ISSN 1068-3755, Surface Engineering and Applied Electrochemistry, 2010, Vol. 46, No. 3, pp. 201–205. © Allerton Press, Inc., 2010.
Original Russian Text © V.D. Shkilev, V.G. Nedioglo, A.N. Adamchuk, 2010, published in Elektronnaya Obrabotka Materialov, 2010, No. 3, pp. 4–8.

## ELECTRICAL PRECISION TREATMENT OF MATERIALS

# The Electric-Discharge Identification of Banknotes

**V. D. Shkilev, V. G. Nedioglo, and A. N. Adamchuk**

*Ministry of Information Development, ul. Pushkina 42, Kishinev, MD- 2012 Republic of Moldova*
*e-mail: schilov@registru.md*

Received October 21, 2009; in final form, January 28, 2010

**Abstract**—New information technologies for manufacturing paper banknotes with a high level of protection are presented. A method for forming a document database based on the association of wave and digital information is offered.

**DOI:** 10.3103/S1068375510030014

The presented work consists of two parts, the first part advances the idea of the high level of banknote protection, and the second one expounds the technological aspects of the realization of the method.

## PART 1

The idea of a processes not completely controllable even theoretically being used for the high-level protection of documents is not new. As far back as the 1960s, S. Wiesner suggested using photons with assigned polarized states [1]. This idea has not been realizable technologically up to now; nevertheless, the suggestion of S. Wiesner was actually brilliant, because new approaches to cryptography that give the hope to sooner or later work out simple and cheap technologies for manufacturing paper banknotes with the highest level of protection have been developed with time on its basis.

Now, let us discuss not the technology for the protection of paper banknotes but a physical experiment carried out in 1989 that helped electron interference be proved [2]. In this experiment, the researchers of the Laboratory for Advanced Research of the Hitachi Company, which was headed by A. Tonomura, and Gakushuin University in Tokyo let an electron flow pass through a penetrable barrier equivalent to a screen between two slots. After passing through the barrier, each electron hit a fluorescent screen, thus producing a short light flash. When observing each flash, the Japanese experimenters could fix the place of hitting of each electron. Modern position-sensitive electron counting systems were used in this expensive experiment. The obtained results proving the wave nature of matter are given in Fig. 1.

At first, (Fig. 1a—10 hits of the target by electrons; Fig. 1 b—100 hits), these flashes seem to be distributed over the target-screen more or less regularly.

However, the hints at a definite picture begin to appear with time (Fig. 3 c—3000 hits). It arises that the flashes prefer to appear in some places and avoid other places on the screen (Fig. 3 c).

In the fourth and fifth expositions (Fig. 1d and Fig. 1e—20000 and 70000 hits of the screen by electrons, respectively) obtained under the conditions of a significant increase in "the exposure time," the sensations turn into an experimental fact—an alternating series of parallel bands proving that the electron interference appears on the target.

Is this experiment the technology that enables the creation of paper banknotes with the highest level of protection? No, this is only a physical experiment hinting at what direction should be taken in the development of the technology. The price of the above-described experiment is extremely high and multiply exceeds the cost of manufacturing a banknote of the most frequently used nominal value. The technology for manufacturing a paper banknote with a high level of protection must be several thousand times cheaper and account for a part of a banknote's nominal value.

## RESULTS AND DISCUSSION

Now, let us pass to the description of another physical experiment [3] that actually opens the path to creating the new technology.

The scheme of its performance is very simple. Small holes are punched in paper by the electric-discharge method. Then, these specimens are scanned in the transmission mode by a usual scanner and stored in a database. The obtained pictures are processed by a computer, and a number of parameters concerning the location of the spots are calculated.

Most of the experimental research in this field [4] describes the properties of the physical processes in an interelectrode gap. The attention of the researchers was almost not devoted to the information potential of these technologies [5].

The important factor permitting the places of the electric punching in the paper to be easily scanned is

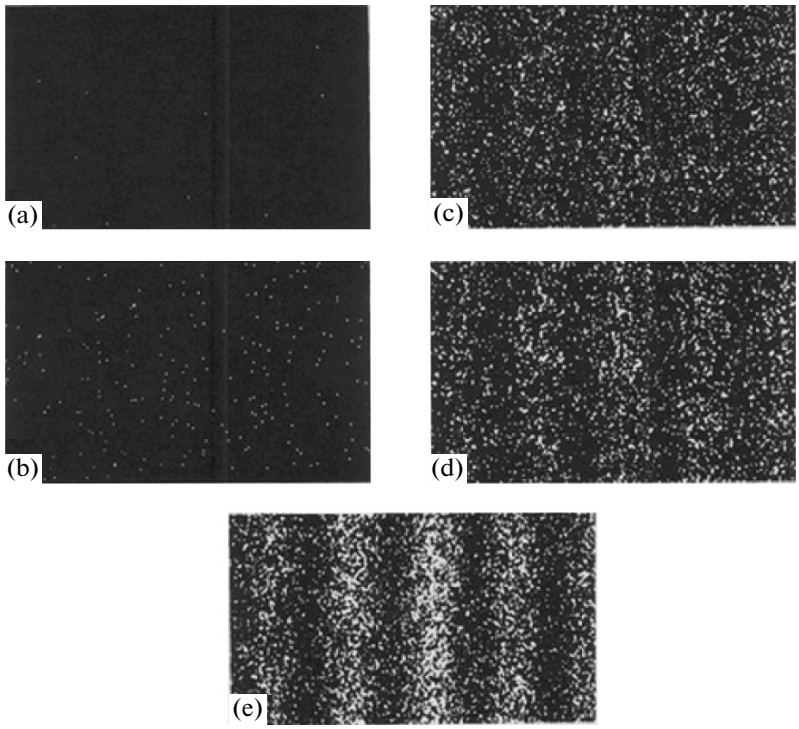


**Fig. 1.** Experimental proof of the existence of matter waves.

that the black colored circle is marked by a laser printer in the area that is to be punched. An individual numeric code is also marked inside this circle presumably when creating a high-security document (Fig. 2). If an individual numeric code is absent, it is impossible to build a database owing to the serious mathematical difficulties arising when using image recognition. The database is built on the combination of digital and wave (individual matrix) information. A document is found in the database using a numeric code, and an individual matrix is used to check whether a document is counterfeit or not. A typical document containing an individual numeric code and an individual picture obtained using electric punching is shown in Fig. 2.


**Fig. 2.** A high-security document protected using an individual numeric code using electric-discharge technology.

Figure 3 shows a typical individual picture (*without a numeric code*), from which it follows not only that the picture as a whole is individual but also that each of the spots is original.

This typical picture (Fig. 3) insignificantly differs from Fig. 1b. The distinction is that the experiment is

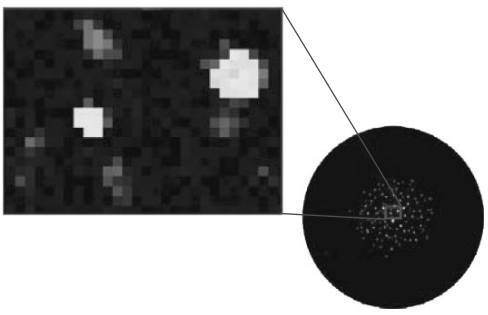

**Fig. 3.** A typical individual image obtained experimentally using the electric-discharge technology.

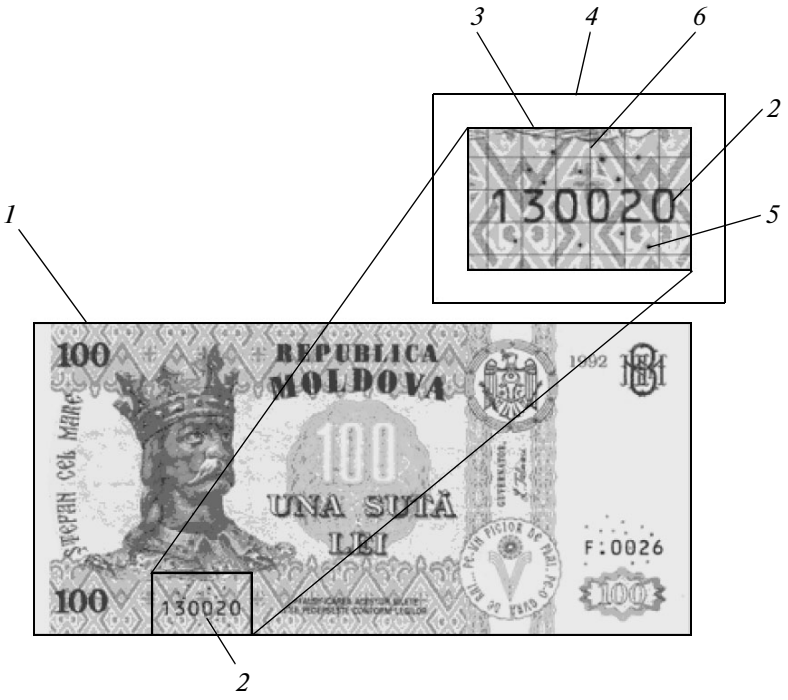


**Fig. 4.** 100 Leus—a banknote of the Republic of Moldova: the paper base with a watermark (*1*); the numeric code of the banknote (*2*); the information-protected area (*3*); the Cartesian system of coordinates (*4*); punches made by the electric-discharge method (*5*); the transparent protection layer (*6*).

ultimately simple and technological, and the results are realized directly on a paper carrier and not on a display screen.

The probability of the repetition of a matrix in the case of individual processing was theoretically estimated at $10^{-400}$. From the standpoint of the protection level, this value is equal to infinity. The technological aspect of the problem shows that infinity and $10^{-400}$ are weakly distinguishable notions.

Does this technology require that new specialized equipment be developed? However strange it may seem, it does not. If a serial high-voltage 20–25 kV transformer and additional electrotechnical details available to all are present, the equipment for manufacturing an identification mark is assembled in 15 min. The expenses for developing and manufacturing such equipment are negligible in comparison with the possible financial losses [6].

When paper banknotes are manufactured, the combination of punches made by the electric-discharge method with already known polygraphic methods of protection may be considered as an important sign. For this purpose, punches are placed near the numeric code of a paper banknote or watermark (Fig. 4).

The signs of authenticity of banknotes are sufficiently large in number. These are latent iridescent bands, diving metalized threads that are seen in the backside of a banknote in the form of brilliant rectangles forming a dotted line, protection fibers, relief images, latent images, watermarks, and microtexts. Recently (the modifications of the 1997 pattern), the Bank of Russia has been introducing a new identification sign—micropunches. However, we know that the micropunches on the 1000 and 5000-ruble banknotes of Russia are made purely mechanically with the help of needles rather than by the electric-discharge method. The banknote's nominal value is marked on a 1000-ruble banknote of the Bank of Russia with the help of micropunches. It is impossible to do this by the electric-discharge method. As usual, this is regarded to be a technological disadvantage. However, such a "disadvantage" turns into a technological advantage in the field of identification. All the banknotes of Russia have the same illustration depicting the banknote's nominal value. This is an accidental original set of punches using the electric-discharge technology. Therefore, this technology may be spoken about in the open press. The technology is easily realizable, but it cannot be repeated twice. When a banknote of Russia is looked at against a light source, the designation of the nominal value formed by the microholes is seen on it (Fig. 5). In the event of using the electric-discharge process, this is an accidental set of punches. The check for authenticity is made by comparing the set of randomly scattered punches with the analogous set stored in the database.

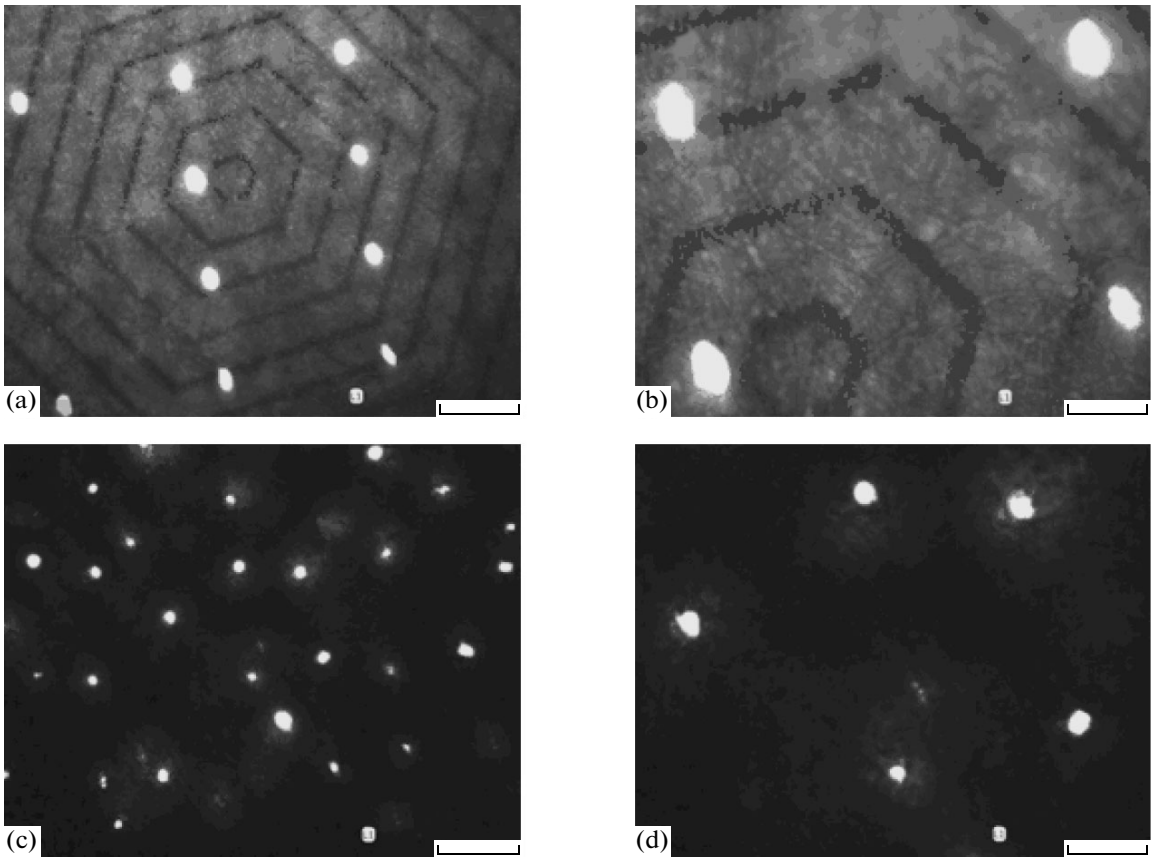


**Fig. 5.** Punches on a banknote of the Russian Federation with a nominal value of 1000 rubles. (a and b) the polygraphic protection in the form of hexahedrons is seen. Electric-discharge punches (c and d). The size of the reference section is 200 microns (a and c) and 500 microns (b and d).

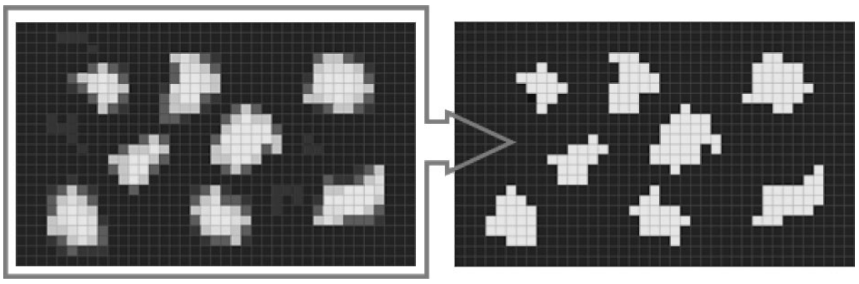

**Fig. 6.** An image before and after binarization.

## PART 2

An approach for direct counting of pixels entering into a ring was used in [3, 6] when analyzing the squares. This approach has a number of disadvantages. It enables one to count only the total square of spots by rings and to reveal the stochastic waves but does not make it possible to calculate the quantity and coordinates of the separate spots, which abruptly narrows the possibility of researching the stochasticity of the process. Therefore, it is appropriate to change to a program that allows the statistical characteristics of each separate sport to be calculated. For this purpose, the following sequence of steps is usually used. The first step is to binarize an image by one of the known methods (W. Niblack, N. Ots, J. Bernsen, et al [7]) with the view to obtaining an image with sharp limits of the spots (Fig. 6). When binarizing an image, the brightness of each pixel is compared with the threshold value of the brightness. If the value of a pixel's brightness is higher than that of the threshold brightness, the corresponding pixel will be "white" in the binary image; otherwise, it will be "black."

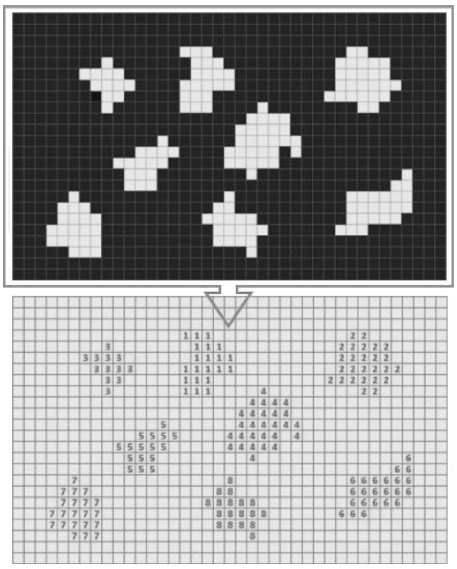

**Fig. 7.** Distinguishing of separate spots.

The second step is to distinguish the separate spots in an image using a recursive or iterative algorithm. The essence of the iterative method is to sequentially scan an image with classifying the white pixels according to the principle of coherence. These operations result in a matrix in which all the pixels of each spot are designated by some number that may also be considered as the sequence number of the spot (Fig. 7).

The third step is to calculate the statistical characteristics of a separate square spot, the coordinates of the center, the dispersion, the bevel, and the excess. The initial image and set of calculated characteristics can be stored in the database to be used in the work of the protection system.

## CONCLUSIONS

A principally new technology for the protection of paper banknotes and documents with a high level of protection has been suggested.

## REFERENCES


1. Wiesner, S., Conjugate Coding, *Sigact News*, 1983, vol. 15, no. 1, pp. 78–88.
2. Tonomura, A., Endo, J., Mamsuda, T., Kawasaki, T., and Exawa, H., Demonstration of Single-Electron Buildup of an Interference Pattern, *Am. J. Phys.*, 1989, vol. 57, pp. 117–120.
3. Shkilev, V.D., Adamchuk, A.N., and Nedioglo, V.G., The Electric-Discharge Technology for Protection of Highly-Important (High-Security) Documents, *Elektron. Obrab. Mater.*, 2008, no. 2, pp. 4–10.
4. Reter, G., Electron Avalanche and Breakdown in Gases, Moscow: Mir, 1968.
5. Shkilev, V.D. et al, Patent of the Republic of Moldova 3389, *MD-BOPI*, 2007, no. 8, p. 51.
6. Shkilev, V.D. and Adamchuk, A.N., New Information Technologies during Manufacturing Paper Banknotes with the Quantum Level of Protection, International Conference "Information and Communication Technologies 2009 ICT Chisinau, Republic of Moldova, pp. 186–188.
7. Fedorov, A., Binarization of Black-and-White Images: the State and Prospects of Development http://iu5.bmstu.ru/~philippovicha/ITS/IST4b/ITS4/Fyodorov.htm.

ISSN 1068-3755, Surface Engineering and Applied Electrochemistry, 2010, Vol. 46, No. 3, pp. 206–214. © Allerton Press, Inc., 2010.
Original Russian Text © S.A. Silkin, S.S. Belevskii, A.S. Gradinar', V.I. Petrenko, I.V. Yakovets, N.I. Tsyntsaru, A.I. Dikusar, 2010, published in Elektronnaya Obrabotka Materialov, 2010, No. 3, pp. 9–18.

ELECTRICAL SURFACE TREATMENT METHODS

# Electrodeposition of Nanocrystalline Co-W Coatings from Citrate Electrolytes Under Controlled Hydrodynamic Conditions Part 3: The Micro- and Macrodistribution of the Deposition Rates, the Structure, and the Mechanical Properties

**S. A. Silkin[a], S. S. Belevskii[b], A. S. Gradinar'[a], V. I. Petrenko[b], I. V. Yakovets[a], N. I. Tsyntsaru[b], and A. I. Dikusar[a, b]**

[a] *Shevchenko Pridnestrov'e State University, ul. 25 Oktyabrya 128, Tiraspol, Republic of Moldova*
[b] *Institute of Applied Physics, Academy of Sciences of Moldova, ul. Academiei 5, Chisinau, MD–2028 Republic of Moldova*
*e-mail: dikusar@phys.asm.md*

Received December 9, 2009

**Abstract**—Using a Hull cell with a rotating cylindrical electrode (RCE), the effect of the hydrodynamic conditions on the deposition rate and its micro- and macrodistribution and the composition and microhardness of the cobalt–tungsten coatings deposited from a citrate electrolyte containing cobalt sulphate (0.2 mol/l) and sodium tungstate (0.2 mol/l) at pH = 6.7 and the solution temperature of 60°C in the Re numbers range of 0 – 3000 is examined. It is shown that the hydrodynamic deposition conditions have no effect whatsoever on the surface roughness, but they slightly influence the electrolyte's throwing power. The correlation between the intensity of the hydrodynamic flows, the deposition rate (due to the current efficiency's increase), and the composition of the coatings (along with their distribution over the surface) is established. It is shown that certain modes of the process at a high deposition rate make it possible to reach a high uniformity of the coating's composition with a high tungsten content, which results in obtaining the maximum surface microhardness.

**DOI:** 10.3103/S1068375510030026

## INTRODUCTION

The study of the composition of the coatings and their functional properties (which are determined, in particular, by the coating's composition), along with such technological parameters as the surface quality (its roughness) and the throwing power (TP) of the electrolyte, i.e., the evaluation of the patterns of the micro- and macrodistribution of the deposition rates, is necessitated by the possibility of the wide practical use of electrolytic cobalt–tungsten coatings as an alternative to those of chromium [1–7]. The micro- and macrodistribution of the deposition rates over the processed surface involves the composition, morphology, and structure modifying and, hence, the changing of the properties of the coatings. The investigation of these parameters under controlled hydrodynamic conditions makes it possible to substantially expand the quantity of information on the technological capacities of such surfaces, which is the purpose of this paper, which is a continuation of the preceding ones [8, 9] aimed at the studying of the effect of the hydrodynamic conditions (the conditions of the ion mass transfer) on the formation of the properties of such coatings.

## EXPERIMENTAL

### *The Electrolyte's Composition and Its Characteristics*

In the present research, the following electrolyte composition was used (mol/l): $Na_2WO_4$—0.2; $CoSO_4$—0.2; $C_6H_8O_7$ (citric acid)—0.04; $Na_3C_6H_5O_7$ (sodium citrate)—0.25; $H_3BO_3$—0.65 (pH = 6.8). The deposition temperature was 60°C. Using such an electrolyte at the indicated temperature is determined by the unique properties (the corrosion and mechanical ones) of the coatings deposited from the above solution [2–7, 10]. It is noteworthy that the electrolyte of the indicated composition was also mentioned in the preceding papers of this series [8, 9] elucidating the role of the hydrodynamic conditions in producing cobalt–tungsten alloy coatings with specified compositions and properties. To control the hydrodynamic deposition conditions, the calculation of the Reynolds criterion is necessary, which (apart from the rotation speeds and the characteristic linear size) requires the values of the kinematical viscosity of the solution at the deposition temperature equal to $0.72 \times 10^{-2}$ cm$^2$/s resulting from the measurements.

*The Electrode and Cell and the Methods of the Surface Preparation prior to the Electrodeposition*

A rotating cylindrical electrode (RCE) served as the testing electrode, but, unlike the electrode described in [8, 9], the "RCE Hull cell" version described in [11–13] was applied.

This scheme made it possible to obtain the distribution of the current densities (the rates of the electrochemical processes) over the RCE surface. The primary current distribution (i.e., the distribution that is not affected by any extra surface processes) in the above geometry of the cell is determined by the following correlation [12, 13]:

$$\frac{i_{(x/h)}}{i_{\text{av}}} = \frac{0.535 - 0.458(x/h)}{\{0.0233 + (x/h)^2\}^{1/2}} + 8.52 \times 10^{-5} \exp\{7.17(x/h)\}, \quad (1)$$

where $h$ is the RCE height, $x$ denotes the actual distance along the RCE surface, and $i_{\text{av}}$ is the average RCE current density.

In the case under consideration (Fig. 1), $h = 30$ mm, $r = 5$ mm, $h/s = 3$, $h/b = 10$, $b/c = 0.3$, and $h/r = 6$. The RCE was located in the cell coaxially with an organic glass cylindrical shield S, so that its lower edge with a fluoroplastic insulating bush was 5 mm higher than the lower edge of the cylindrical shield, and the latter was at a 20 mm distance from the cell bottom. The location of the graphite disk anode did not effect the current distribution over the RCE surface. The initial current distribution in the cell with such a geometry and the indicated geometrical sizes was determined using equation (1). Brass cylindrical electrodes served as the rotating electrodes.

After the mechanical polishing immediately prior to the electrodeposition, the electrode surface was covered with a layer of the electrolytic nickel. The nickel-plating electrolyte comprised 240 g/l of a nickel chloride solution (hexaqueous) and 80 g/l of hydrochloric acid. The electrodeposition lasted for 1 min at a current density of 30 mA/cm$^2$.

The rotation speed in the case of the RCE Hull cell was varied from 0 to 810 rot/min, which was relevant to the variation of the Reynolds numbers in the interval of 0–2950. At $Re \geq 200$,a turbulent character of the flow is known [14] to be developed on such an electrode, and the density of the limiting diffusion current (the rates of the ion mass transfer) on such an electrode is determined by the following correlation:

$$i_{\text{pr}} = 0.079 nFC_0 \omega (\omega r/\nu)^{-0.3} (\nu/D)^{-0.644}, \quad (2)$$

where $\omega$ denotes the RCE rotation frequency (s$^{-1}$), $r$ is its radius (cm), $\nu$ designates the coefficient of the kinematical viscosity (cm$^2$ s$^{-1}$), and $D$ implies the coefficient of diffusion of the reduction ion (cm$^2$ s$^{-1}$). The total volume of the electrolyte in the cell was approximately 300 ml. The thermostating of the cell was performed by means of a heat exchanging unit located beyond the shielding cylinder $S$ (Fig. 1).

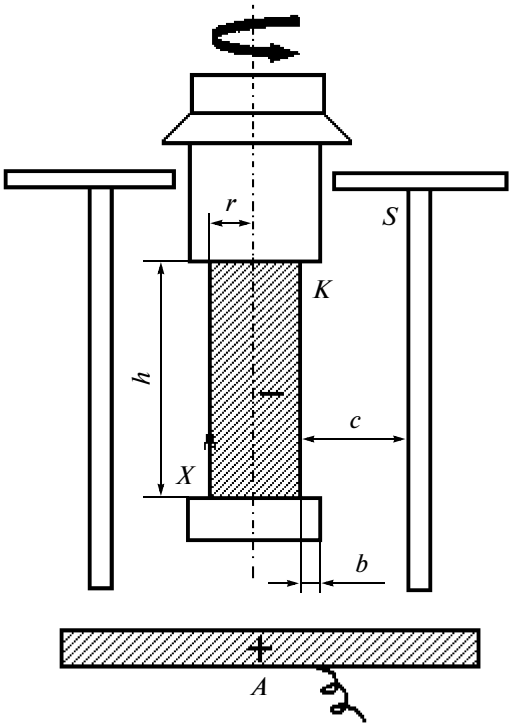


**Fig. 1.** The scheme of the Hull cell with a rotating cylindrical electrode.

In the experiments with the fixed cylindrical electrode at the zero rotation speed, the *Re* number was 0. In this investigation, the minimum RCE rotation speed was 280 rot/min, which corresponded to the *Re* number of about 1000. Thus, the flow mode was a developed turbulent one in all of the cases upon the RCE rotation, which suggested the electrode surface to be equally available for the mass transfer processes. As for the primary current distribution, it obeyed equation (1).

*The electrochemical measurements in the RCE Hull cell* were carried out using 30 mm long brass electrodes. Since the aim was to examine the distribution of the deposition rates along the electrode's length, 7 equally spaced points were marked on the electrode with respect to which all of the characteristics were determined.

The table gives the current density values calculated using equation (1) for the RCE in the above geometry under conditions of the initial current distribution for the various average current densities. The experiments were carried out under the galvanostatic conditions with the average current densities of 0.5, 1, and 2 A/dm$^2$.

In accordance with these data, in the case of the primary distribution, the current density is varied along the electrode length by 12 times for the surface

The values of the current densities of the primary distribution ($A/dm^2$) in the the RCE Hull cell

| Point no. | Position, $x/h$ | Average current density, $A/dm^2$ | | |
|---|---|---|---|---|
| | | 0.5 | 1 | 2 |
| 1 | 0.1 | 1.5 | 3 | 6 |
| 2 | 0.24 | 1 | 2 | 4 |
| 3 | 0.37 | 0.5 | 1 | 2 |
| 4 | 0.51 | 0.375 | 0.75 | 1.5 |
| 5 | 0.64 | 0.25 | 0.5 | 1 |
| 6 | 0.77 | 0.165 | 0.33 | 0.66 |
| 7 | 0.91 | 0.125 | 0.25 | 0.5 |

points indicated on the RCE in the interval of the $x/h$ values of 0.1–0.91, which allowed us within one experiment to evaluate the changes of the characteristics in a fairly wide range of the current densities. Upon the variation of the average current density by 4 times, the maximum difference of the extreme values of the investigated current densities reaches 48 times. At $x/h = 0.37$, the local value of the current density equals the average current density.

The electrodeposition at the selected average current density and the RCE rotation speed was performed at a constant electricity quantity of 60 $C/cm^2$. The average values of the current efficiency at various speeds of rotation (the *Re* numbers) were determined with account for the specimens' mass difference prior to and after the experiment. The current efficiency was calculated based on the theoretical electrochemical equivalent of the alloy equaling 0.311 mg/C. The alloy's compositional variation may give an error of no more than 1%.

In each of the experiments, after the electrodeposition, the coating's average thickness was determined at each of the 7 points whose positions are indicated in the table. Using the method offered in [13, 15] based on the determination of the thicknesses of the deposited layers at points with various $x/h$ values and with the TP electrolyte, at a fixed RCE rotation speed, the average current density was determined.

### *Methods of the Analysis of the Coating and the Determination of its Mechanical Properties*

A specimen with a deposited coating was exposed to a complex investigation for the determination of the parameters at each of the above-indicated 7 test points. The local analysis of the surface was performed using a TESCAN VEGA scanning electron microscope (Great Britain). Simultaneously, the local elemental analysis of the coating using an EDX supplement to the microscope was carried out. The concentration of the components was determined at several points with the $x/h$ fixed values. The paper includes their average values along with the standard deviations. The values of the concentrations of one of the components of the coating (that of tungsten) obtained from the EDX analysis are presented in mass %. At the same time, the indicated values of the concentrations are relevant to their content in the alloy's metal fraction (with no consideration of the light elements of C, O, and H, which are present in the coating (the EDX analysis fails to identify hydrogen)). Using the above microscope, the surface morphology at various RCE points was also determined.

For the qualitative estimation of the surface morphology of the deposited coating, the roughness was determined according to the *Ra* indicator. The measurements were taken using a Surtonic profilograph–profilometer (Taylor Hobson, Great Britain).

The roughness measurements were performed at the axis direction with a reference base of 0.8 mm, which is relevant to the range of the roughness values being measured, with a 10–12 fold number of repetitions. When using a 2.4 mm long tracing, only averaged measurements are possible in the proximity of the points of $x/h = 0.24$, 0.37, and 0.64 of the surface. The measurements were carried out throughout the entire circle length of the cylinder upon the successive rotation of the latter. The average *Ra* values and the standard deviations are presented below. For the estimation of the intrinsic roughness effect on the final roughness of the deposited coating, before beginning the experiment, similar measurements were performed prior to the electrodeposition (i.e., of the surfaces obtained after the nickel plating).

Using a microhardness tester (PMT-3, Russia), the surface microhardness and the surface roughness (*Ra*) measurements were performed at similar points.

Such methods for the analysis of the processes allowed us to fix the effect of the various current densities within a single experiment. All of the values of the electrodeposition parameters or the surface properties presented below are given with respect to the current density of the primary distribution.

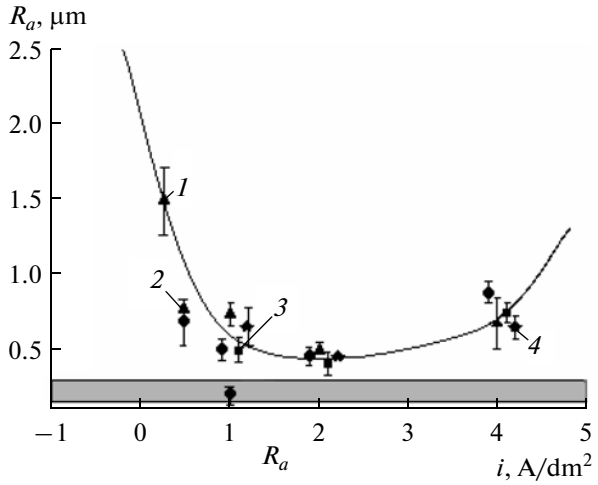


**Fig. 2.** Influence of the current density of the initial distribution on the roughness of the surfaces of the Co-W coatings deposited at the following Re numbers: 0 (*1*), 950 (*2*), 1490 (*3*), 2950 (*4*).

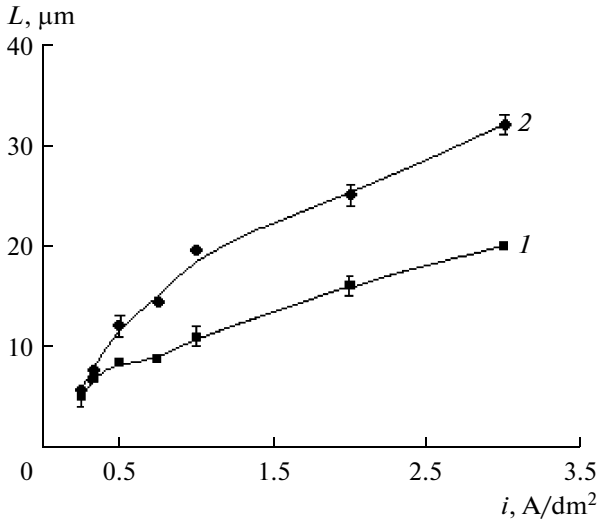


**Fig. 3.** The influence of the local current density of the primary distribution in the RCE Hull cell on the coating thickness at the RCE speed of rotation of 0 rot/min (*1*) and 410 rot/min (*2*) and the average current density of 1 A/dm$^2$.

## RESULTS AND DISCUSSION

### *The Microdistribution of the Deposition Rates and the Hydrodynamic Effect on the Surface Roughness*

The results of the investigation of the hydrodynamic effect are shown in Fig. 2 as the *Ra* dependency on the current density of the primary distribution. There are also given the roughness values of the initial surface, since it is evident that the roughness of the deposited layers may be intrinsic; i.e., it can be determined, in particular, also by the initial roughness. The obtained results show the absence of the hydrodynamic influence on *Ra*. At the same time, the current density effect is evident.

The minimum value of the roughness can be achieved at a current density of 1–2 A/dm$^2$. As is shown in [9], it is in this region of the current densities that the concentration limitations of the process rate are observed upon the electrodeposition from the electrolyte under study. It is also shown there that the electrodeposition of such coatings is a duffusion–kinetic process, and the correlation of the components in the alloy is largely influenced by the electrode potential's varying. The qualitative regularities mentioned in [9] are revealed in the formation of the surface roughness (as resulting from the microdistribution of the deposition rates). It is also seen that the roughness of the electrodeposited surfaces, as a rule, exceeds that of the initial surfaces.

### *The Influence of the Hydrodynamic Conditions on the Deposition Rate*

Not only the current density (as follows from [8, 9]) but also the thickness of the obtained coatings (Fig. 3) (i.e., the deposition rate) is affected by the rate of the stirring. Moreover, such an influence is absent at low current densities, and it enhances at an increase of the current density (Fig. 3). It is evident that the observed influence also comprises an effect on the current efficiency (Fig. 4). Unlike the results shown in Fig. 3, where the local variations of the thicknesses of the coatings are presented, the current efficiency modifi-

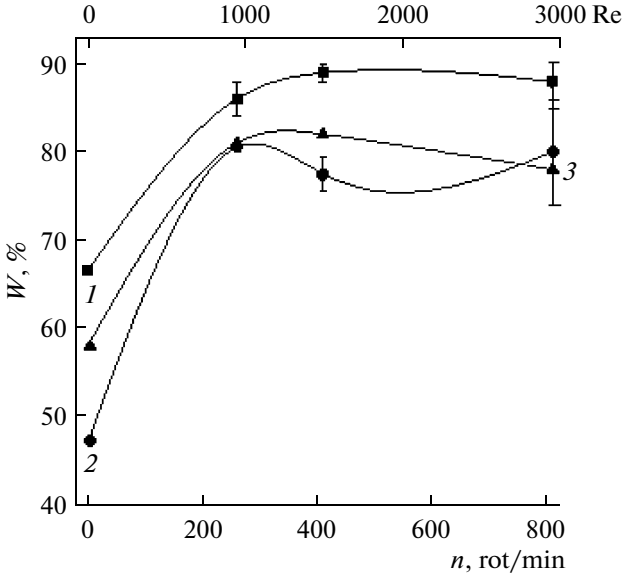


**Fig. 4.** The dependency of the current efficiency on the RCE speed of rotation (the Re number) for the various average current densities, A/dm$^2$: 1 (*1*), 2 (*2*), and 0.5 (*3*) in the RCE Hull cell.

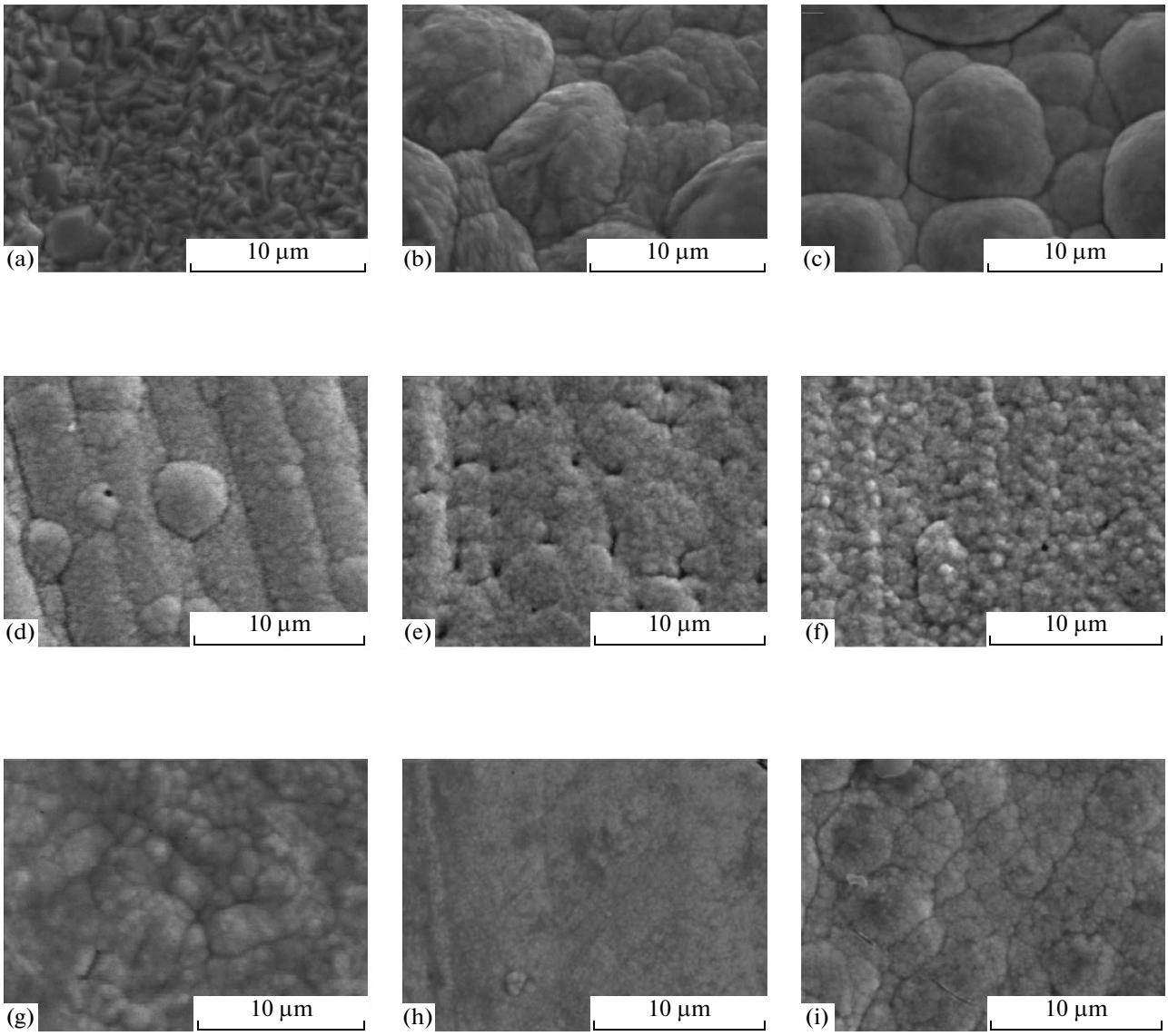


**Fig. 5.** The morphology of the surfaces obtained at the average current densities, A/dm$^2$: 0.5 (a, b, c); 1.0 (d, e, f); 2.0 (g, h, i); Re = 0; and at the $x/h$ values 0.1 (c, f, i), 0.37 (d, e, h), and 0.91 (a, d, g).

cations (Fig. 4) represent the variations of the average values over the entire surface. The character of the hydrodynamic effect in this case is such that the current efficiency's influence is observed only in the range of relatively low agitation rates with the maximum values of the current efficiency being detected at the average values of the current density (1 A/dm$^2$). With the results of [9], one may assume that the effect of the current efficiency's increase is predominant for the increase of the deposition rate and the deposited layer's thickness upon a fixed value of the passed charge and under the conditions of the intensification of the hydrodynamic mode of the deposition.

### *The Hydrodynamic Conditions and the Morphology of the Coatings*

As it follows from [9], the diffusion control (the effect of the stirring rate) determines the deposition kinetics only at sufficiently high potentials and current densities (1–2 A/dm$^2$). This in turn causes the effect of the hydrodynamic conditions of the deposition on the morphology of the coatings (Figs. 5, 6). In the general case, the stirring contributes to the creation of more microcrystalline surfaces. It is also noteworthy that, upon the current density (the potential) increase, surfaces with a less pronounced crystallinity are found to be formed at the average current densities (Figs. 5, 6).

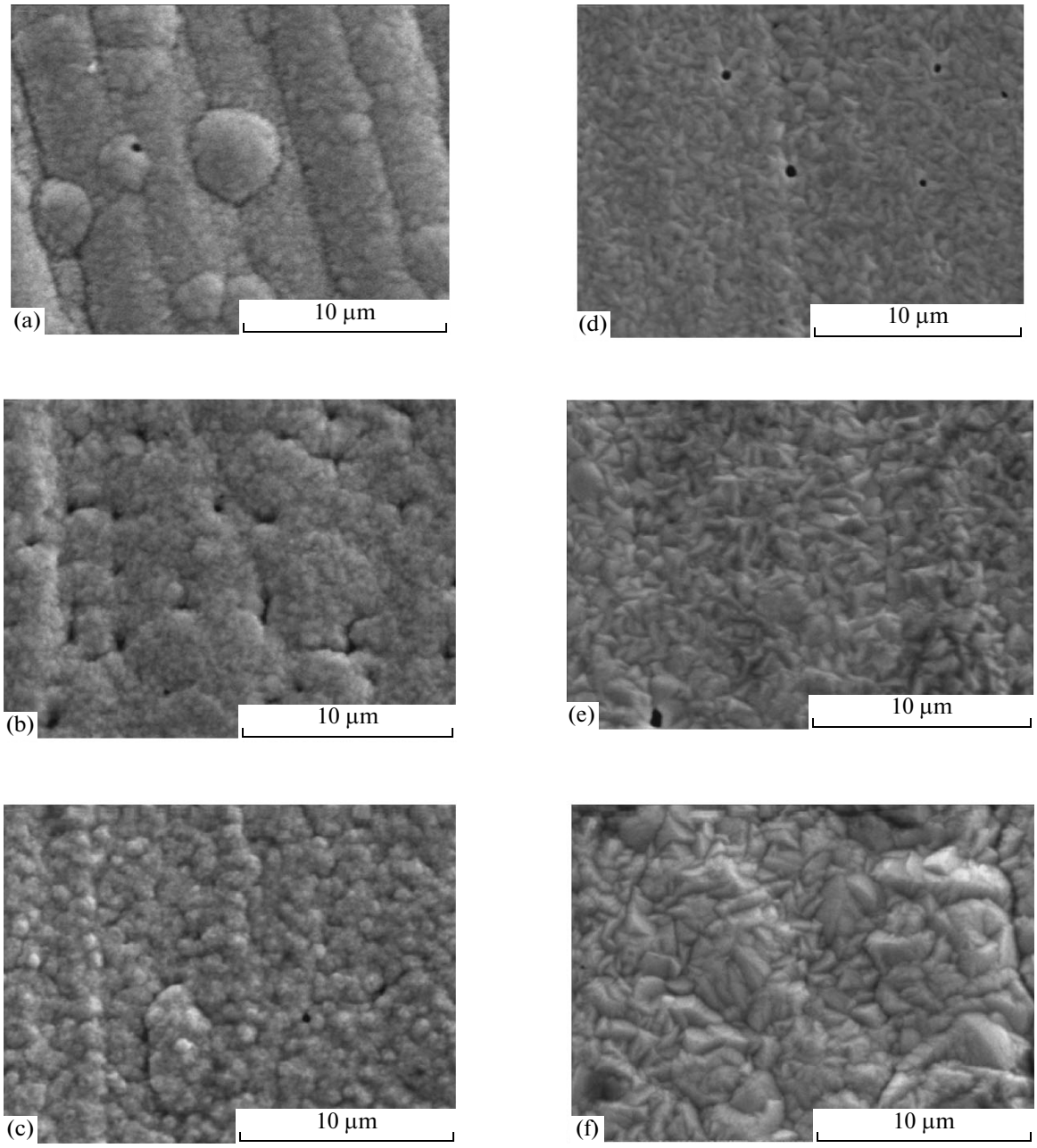


**Fig. 6.** The stirring rate's effect on the surface morphology at $i_{av} = 1$ A/dm$^2$; $Re = 0$ (a, b,c); Re = 1500 (d, e, f); and $x/h = 0.1$ (c, f), 0.37 (b, e), and 0.91 (a, d).

### *The Hydrodynamic Conditions of the Deposition and the Coating's Composition*

As was noted earlier (see [9], Fig. 1), the grain size (the characteristic size of the crystallites) is strongly affected by the *W* content in the coating. The results of the local EDX analysis shown in Fig. 7 illustrate the complex influence of the hydrodynamics on the tungsten–cobalt correlation. At the average and high current densities, the tungsten concentration is maximum in the experiments without stirring, and, at lower current densities, the maximum is registered at the average Reynolds numbers. At Re = 0, the tungsten content grows upon the current density increase, and it decreases at high Reynolds numbers (Fig. 8).

The distribution of the element concentration over the surface and the current density effect are of great importance for the regularities of such a distribution. It differs with the presence and absence of stirring. At a low current density and with a fixed electrode, the distribution is maximally nonuniform (Fig. 7a). The *W* concentration is maximum at high *i*.

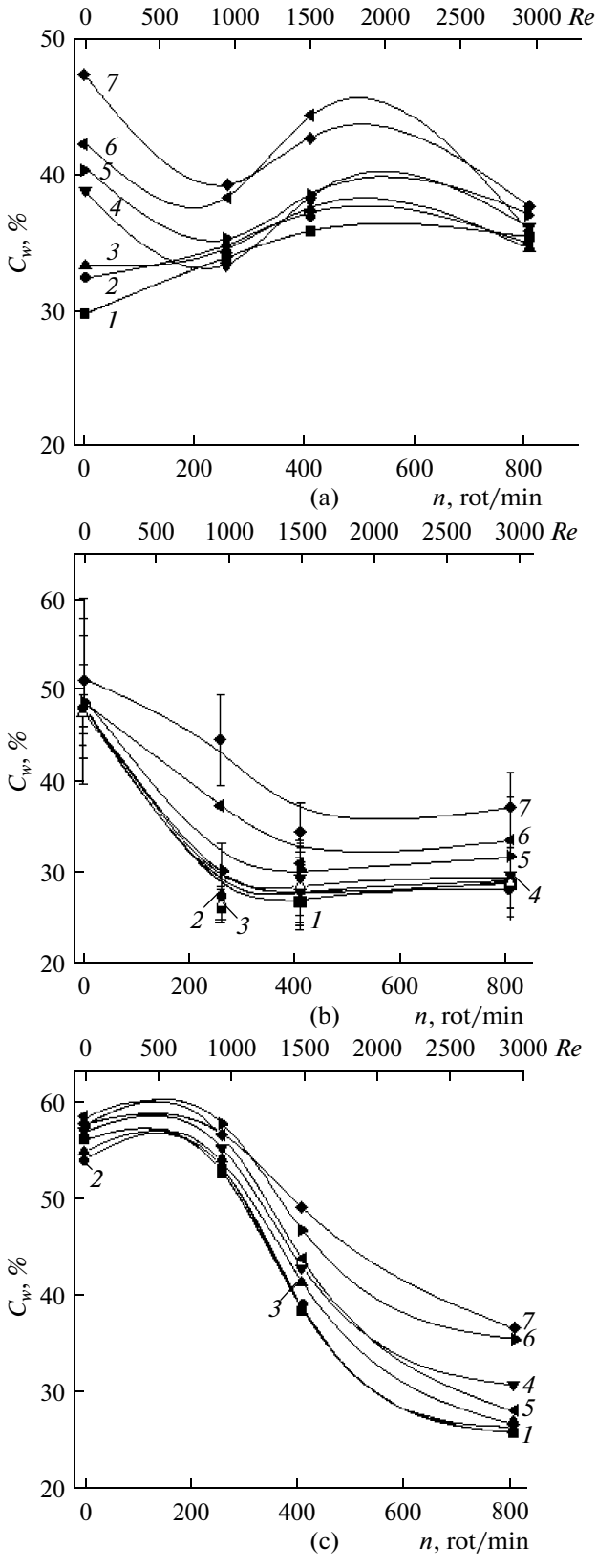


**Fig. 7.** The hydrodynamic effect on the *W* concentration in the alloy (mass %) in the RCE Hull cell at an average current density, A/dm$^2$, of 0.5 (a), 1 (b), and 2 (c).

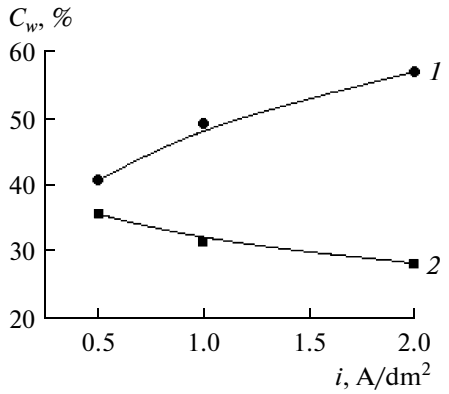


**Fig. 8.** The influence of the average current density on the *W* concentration in the alloy (mass %) at Re = 0 (1) and Re = 2950 (2).

Note quite the opposite picture with high stirring rates. In this case, the maximum *W* concentration is detected at higher current densities but along with a greater nonuniformity of the concentration distribution (Figs. 7b, 7c). It is evident that the best indicators are those obtained at the average current density of 2 A/dm$^2$ (Fig. 7c). Under these conditions, (a) the *W* concentration is maximum, (b) the uniformity of its distribution is maximum, and (c) the stirring rate does not actually influence either the tungsten concentration or its distribution (at relatively low *Re* numbers <1000).

### *The Electrolyte's Throwing Power*

The main indicator of the macrodistribution of the electrochemical deposition rates is the electrolyte's throwing power (TP). The results of its determination using the above methods with the RCE Hull cell are shown in Fig. 9.

This figure shows both the average TP values (obtained at various average current densities) and the highest and lowest values of the current densities used. One can see that the dependency on the current density is virtually absent, while the dependency of the rotation speed (the Reynolds numbers) is present. Moreover, the uniformity of the distribution of the deposition rates (i.e., the TP) decreases with the stirring rate increase. Such a dependency follows, for instance, from the results shown in Fig. 3. It is seen that, at the low current densities, the hydrodynamic effect is actually absent, while, at the high ones, it is present. A consequence of this phenomenon appears to be the enhancement of the nonuniformity of the deposition rate's distribution upon an increase of the mass transfer intensity.

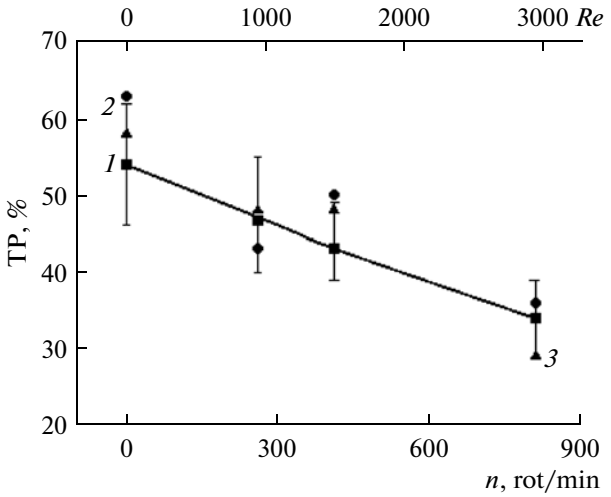


**Fig. 9.** The influence of the hydrodynamic mode on the average values of the electrolyte's throwing power (*1*) and the TP values at the average current densities, A/dm$^2$, of 0.5 (*1*) and 2 (*2*).

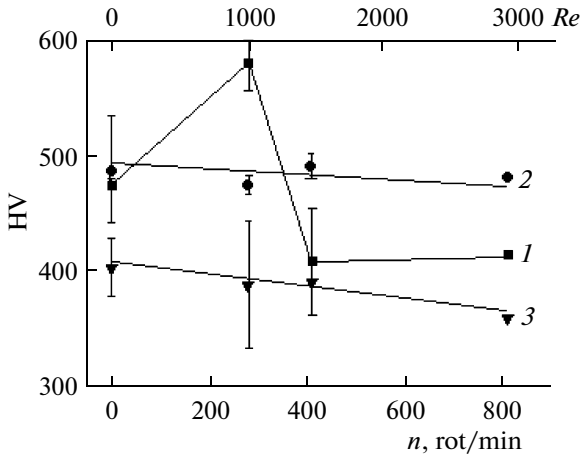


**Fig. 10.** The influence of the hydrodynamic mode on the microhardness (kg/mm$^2$) of the Co-W coatings for the densities of the initial current distribution, A/dm$^2$, of (*1*) 2, (*2*) 1, (*3*) 0.5.

### *Microhardness of the Coatings*

The complex effect of the electric and hydrodynamic modes of the deposition on the composition and structure of the forming coatings eventually determines their functional properties. One of the important features is the surface microhardness, whose dependency on the current density and the hydrodynamic modes is shown in Fig. 10.

The results presented in this graph are obtained upon the average current density of 1 A/dm$^2$. However, the local measurements at certain points of the cylinder's height make it possible to attribute curve *1* to the current density of 2 A/dm$^2$, and curve *3* to the current density of 0.5 A/dm$^2$. The hydrodynamic effect is seen to occur in this case too with the lowest microhardness values being observed at the lowest current densities. The maximum of the microhardness is found to be reached at the average Reynolds numbers and the current density of 2 A/dm$^2$. The comparison with the results of the elemental analysis (Fig. 7) shows that it is under these conditions that the maximum tungsten concentration is observed in the coating.

Since the results presented in Fig.10 were obtained upon only the average current density, they do reveal the common regularity but do not manifest the maximum possible factors. However, they convincingly show that (a) the current density (potential) increase leads to an increase of the microhardness, (b) correlations are found to be between the tungsten concentration in the coating and the increase of its microhardness (compare Fig. 7 and Fig. 10), (c) the intensification of the hydrodynamic flows decreasing the tungsten concentration in the coating (Fig. 7) leads (in the general case) to the microhardness's decrease (Fig. 10), and (d) an insignificant intensification of the hydrodynamic mode upon maintaining a sufficiently high concentration of tungsten in the coating may lead to a microhardness increase (compare the results in Fig. 7c in the interval of the Re numbers of 0–1000 and the microhardness data in the same interval of the *Re* numbers in Fig. 10).

## CONCLUSIONS

The results of the research performed show the effect of the hydrodynamic conditions in the formation of the electrolytic cobalt–tungsten coatings deposited from the citrate electrolytes. They indicate that a lot of the functional properties depend primarily on the alloy composition, which, in turn, is determined by the hydrodynamic conditions. However, the rate increase of the hydrodynamic flows, as a rule, decreases the tungsten concentration in the coating and, hence, has a negative effect on a number of properties. The hydrodynamic influence on the cobalt's reduction rate (see, e.g., [8, 9]) may be considered as one of the possible reasons for the tungsten concentration decrease in the coating.

It is shown that the hydrodynamic conditions actually fail to influence the surface roughness. This fact is very important for the development of the scientific technological bases of obtaining such coatings. The electrolyte throwing power is found to be affected by the hydrodynamics. It is noteworthy that the solution of the problems presented in this paper appears possible due to the elaboration of the preceding method for the TP estimation under the controlled hydrodynamic conditions [13, 15].

The distribution peculiarities of the coating's composition depending on the deposition rate and the hydrodynamic conditions are such that, upon the low

current densities in the absence of stirring, the utmost nonuniformity of the composition is observed. The current density increase leads to an enhancement of the uniformity of the composition's distribution but only with a fixed electrode. Upon stirring, not only the $W$ concentration decreases but also the nonuniformity of its surface distribution increases (hence, the nonuniformity of the properties enhances). At the same time, upon certain (optimal) modes of the deposition (the current density and hydrodynamic conditions), a high uniformity of the distribution of the coating composition (with a high tungsten concentration) and a high deposition rate seem possible.

Note that the results of the present investigation relate to a strictly specified electrolyte composition, whose modification may profoundly change the estimation of the influence of the hydrodynamic factors. However, the general patterns of the micro- and macrodistribution of the deposition rates and the composition and properties of the coatings remained unchanged.

## ACKNOWLEDGMENTS

The authors thank I.Yu. Tolmacheva, a student of Shevchenko Technological State University, for assistance in the experimental works.

The financing of the research was performed within the framework of the state programs of the Moldova Republic (Electrophysical and Chemical Surface Processes of Micro- and Nanometric Scales; Multilayer Nanostructural Materials Obtained by Electrochemical Methods; The Study of the Tribological, Corrosion, and Magnetic Properties) along with the Moldavian National Project for Young Research Workers (project no. 09.819.05).

## REFERENCES

1. Weston, D.P., Shipway, P.H., Harris, S.L., and Cheng, M.K., Friction and Sliding Wear Behavior of Electrodeposited Cobalt and Cobalt-Tungsten Alloy Coatings for Replacement of Electrodeposited Chromium, *Wear*, 2009, no. 267, pp. 934–943.
2. Tsyntsaru, N., Belevsky, S., Dikusar, A., and Celis, J.-P., Tribological Behaviour of Electrodeposited Cobalt–Tungsten Coatings: Dependence on Current Parameters, *Trans. Inst. Metal Finish.*, 2008, vol. 86, pp. 301–307.
3. Tsyntsaru, N., Dikusar, A., Cesiulis, H., Celis, J.-P., Bobanova, J., Sidelinikova, S., Belevsky, S., Yapontseva, Yu., Bersirova, O., and Kublanovsky, V., Tribological and Corrosion Properties of Electrochemical Coatings on the Base of Cobalt and Iron Superalloys, *Powder Metall. Met. Ceram.*, 2009, no. 7/8, pp. 66–78.
4. Tsyntsaru, N., Cesiulis, H., Bobanova, J., Croitoru, D., Dikusar, A., and Celis, J.-P., Electrodeposition and Tribological Characterization of Nanostructured Co-W and Fe-W Alloys, *Proc. Int. Conf. BALTTRIB*, Kaunas, 2009, pp. 205–209.
5. Kublanovsky, V., Bersirova, O., Yapontseva, Yu., Tsyntsaru, N., Belevsky, S., and Dikusar A., Pulse Electrodeposition of Cobalt-Tungsten Alloys from Citrate Electrolyte on Steel, its Corrosion Characteristics, *Phys.-Chem. Mech. Mater.*, 2007, no. 6, pp. 80–90.
6. Tsyntsaru, N.I., Belevskii, S.S., Volodina, G.F., Bersirova, O.L., Yapontseva, Yu.S., Kublanovskii, V.S., and Dikusar, A.I., Composition, Structure and Corrosion Properties of Coatings from Co–W Alloys Electrodeposited under the Direct Current, *Elektron. Obrab. Mater.*, 2007, no. 5. pp. 9–15.
7. Silkin, S.A., Belevskii, S.S., Tsyntsaru, N.I., Shul'man, A.I., Shchuplyakov, A.N., and Dikusar, A.I., Influence of Long-Term Operation of Electrolytes on the Composition, Morphology and Mechanical Properties of Surface Produced at Deposition of Co–W Coatings from Citrate Solutions, *Surf. Eng. Appl. Electrochem.*, 2009. vol. 45. no. 1, pp. 1–12.
8. Belevskii, S.S., Yushchenko, S.P., and Dikusar A.I., Electrodeposition of Nanocrystalline Co-W Coatings from Citrate Electrolytes under Conditions of Controlled Hydrodynamics: Part 1. Co Electrodeposition, *Surf. Eng. Appl. Electrochem.*, 2009, vol. 45, no. 6, pp. 446–454.
9. Belevskii, S.S., Tsyntsaru, N.I., and Dikusar, A.I., Electrodeposition of Nanocrystalline Co-W Coatings from Citrate Electrolytes under Conditions of Controlled Hydrodynamics. 2. Deposition Rate and Coating Composition, *Electron. Obrab. Mater.*, 2010. no. 2, pp. 9–18.
10. Silkin, S.A., Tin'kov, O.V., Petrenko, V.I., Tsyntsaru, N.I., and Dikusar, A.I., Electrodeposition of Alloys: the Role of Temperature, *Elektron. Obrab. Mater.*, 2006, no. 4, pp. 11–18.
11. Podlaha, E.J. and Landolt, D., Induced Codeposition. 1. Experimental Investigation of Ni-Mo Alloys, *J. Electrochem. Soc.* 1996, vol. 143, pp. 885-892.
12. Madore, C., West, A.C., Matlosz, M., and Landolt, D., Design Consideration for a Cylinder Hull Cell with Forced Convection, *Electrochim. Acta*, 1992, vol. 37, no. 1, p. 69.
13. Bobanova, Zh. I., Yushchenko, S.P., Yakovets, I.V., Yakhova, E.A., and Dikusar, A.I., Determination of Throwing Power under the Electrochemical Treatment Using the Hull Cell with a Rotating Cylindrical Electrode, *Elektron. Obrab. Mater.*, 2000, no. 6, pp. 4–15.
14. Eisenberg, M., Tobias, C.W., and Wilke, C.R., Ionic Mass Transfer and Concentration Polarization at Rotating Electrodes, *J. Electrochem. Soc.*, 1954, vol. 101, pp. 306.
15. Bobanova, Zh. I., Yushchenko, S.P., Yakovets, I.V., and Dikusar, A.I., Throwing Power of Sulfuric Electrolyte of Copper Plating under the Intensive Electrodeposition Modes, *Elektrokhimiya*, 2005, vol. 41, no. 1, pp. 91–96.

ISSN 1068-3755, Surface Engineering and Applied Electrochemistry, 2010, Vol. 46, No. 3, pp. 215–217. © Allerton Press, Inc., 2010.
Original Russian Text © N.A. Onatskaya, L.Yu. Demidenko, 2010, published in Elektronnaya Obrabotka Materialov, 2010, No. 3, pp. 19–21.

## ELECTRICAL SURFACE TREATMENT METHODS

# Influence of Schemes of Treatment by Current Pulses on the Formation of the Physical Contact at Pressure Welding

**N. A. Onatskaya and L. Yu. Demidenko**

*Institute of Pulse Processes and Technologies, National Academy of Sciences of Ukraine*
*pr. Oktyabrskii 43a, Nikolaev, 54018 Ukraine*
*e-mail: dpta@iipt.com.ua*

Received September 23, 2009

**Abstract**—It is shown that the treatment of the deformation zone of the precompressed metal plates by current pulses with a density of $10^9$ A/m$^2$ and a duration of about $10^{-4}$ s intensifies the plastic deformation in this region and favors the activation of the contact surfaces. It is found that the highest effect from the viewpoint of the formation of the largest physical contact area occurs in the case of the current passage along the contact zone and, in turn, through both plates with the reduction of the height of the microroughnesses amounting to 75% and the total area of the zones of the plate surface's spreading being in the range from 65 to 70% of the total contact surface area.

**DOI:** 10.3103/S1068375510030038

It is known [1] that, at any methods of pressure welding, the determining part in the formation of the welded joint is assigned to plastic deformation, greatly affecting all the stages of the process. Compression of the welding surfaces is necessary in order to create it. With the diffusion welding circuit being conventional, when the pressure and temperature can be controlled independently, the process is carried out with the pressure at the level of the yield point of the less durable material at the welding temperature [2].

In the method under study of the welding of solid state metals, the compression of the welded surfaces and the plastic deformation of the near-contact layers are performed at the environmental temperature. In the initial stages of the joint formation, the physical contact area's growth occurs at the prevailing action of the thresholding mechanisms of the microplastic deformation. However, this deformation is limited, as the near-contact layers are hardened, and the stresses in the contact reduce. Thus, in order that the physical contact area to be developed and new activation centers on the surface of the weld details are created, it is necessary to use the methods of the plastic deformation process's enhancement.

The application of an electric current seems to be rather promising, as it is known that the introduction of concentrated energy flows in the form of current pulses with a density around $10^9$ A/m$^2$ and a duration of about $10^{-4}$ s directly into the metal deformation zone causes the electroplastic effect (EPE), consisting in the drastic drop of the metal resistance to deformation and an increase of its plasticity [3].

The purpose of this work is to investigate the influence of different schemes of treatment by current pulses on the formation of the physical contact of the interfacing surfaces at the welding of metals in the solid state.

Homogeneous materials (plates of steel 20 of sizes 170 × 15 × 3.0 mm) were chosen as the model specimens. The preparation of the surface for welding consisted in its grinding up to a roughness with the surface finish being not more than 6 μm with the following degreasing of the plate's surface using acetone. The plastic deformation of the microroughnesses on the contact surfaces was carried out through the compression of the specimens using a special tool up to a pressure of 50 MPa. Through the compressed plates, there was passed the current pulses with the above mentioned parameters remaining unchangeable for the different schemes of the treatment. The following treatment schemes were examined:

—scheme 1 – the treatment of the contact zone by the current pulses through one of the compressed plates;

—scheme 2 – the treatment of the contact zone by the current pulses in turn through both compressed plates.

The influence of the schemes of treatment using the current pulses was estimated indirectly according to the change of the surface texture of the welded plates after the treatment.

The investigation of the surface texture of the welded plates was conducted with the help of a scanning electron microscope of the SEM-515 type of the Fillips firm (Holland).[1]

[1] The electron-microscopic investigation was carried out by E.N. Berdnikova and E.O. Paton (IEW, National Academy of Sciences of Ukraine).

Change of the surface texture parameters of the specimens of steel 20 at different schemes of treatment by the current pulses

| Schemes | Plate (steel 20 + steel 20) | Place of investigation | Texture parameters, μm | | | Total surface area, S, % | |
|---|---|---|---|---|---|---|---|
| | | | $H_1/H_0$ | δ | Δ | $S_0$ | $S_1$ |
| 1 | upper | center | 3/6 | 6–7 | 12–13 | 93 | 7 |
| | | edge | 3/6 | 7–8 | 20–22 | 92 | 8 |
| | lower | center | 3/6 | 7 | 13–15 | 94 | 6 |
| | | edge | 3/6 | 7–8 | 15 | 92–93 | 7–8 |
| 2 | upper | center | 1/6 | 20 | 60 | 30 | 70 |
| | | edge | 2/6 | 14 | 50 | 35–40 | 60–65 |
| | lower | center | 1/6 | 15–16 | 50 | 35 | 65 |
| | | edge | 2/6 | 16 | 8–50 | 45–50 | 50–55 |

Rectangular plates of size 30 × 15 × 3 mm cut from the contact zone of the welded specimens were the subjects of the research. The central contact region of the compressed plates and their peripheral zone were studied. The initial plate after the grinding was used as the control sample.

The change of the surface texture in different regions of the contact interaction was estimated according to the following parameters:

—the total area of the surface texture of different types $S = S_0 + S_1$, where $S_0$ is the relative area of the surface texture without any changes caused by the technological action, and $S_1$ is the relative area of the spreading zones (with the texture being maintained or upset) caused by the action of the technological parameters;

—the change of the most typical height of the roughness projection combs ($H_1/H_0$), where $H_1$ is the height of the deformed roughness projection combs, and $H_0$ is the initial height of the roughness projection combs;

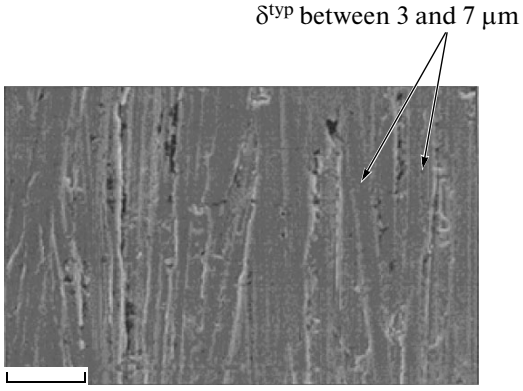


**Fig. 1.** The surface texture of the plate of steel 20 after treatment by the current pulses according to the scheme 1 ×1000.

—the change of the most typical width of the local zones of the bearing or the spreading of the separate (δ, μm) or several merged (Δ, μm) roughness bands.

It is assumed that, in order to form the welded joint, it is necessary to ensure the most favorable changes of the contact surfaces' texture as determined by the following features:

—the maximum spreading area $S_1$ corresponding to the area of the physical contact of the connected surfaces;

—the minimum comb height in the spreading zones $H_1$ indicating the maximum upsetting of the separate roughness projections of the contact surfaces;

—the maximum width of the local zones of the spreading of the separate crumpled bands or roughness projections δ or several merged spreading zones Δ that add up to the total bearing area $S_1$.

By comparing the texture of the specimens' surfaces before and after the treatment by the current pulses using the different schemes, there can be noted the changes in the surface texture caused by the technological action. The investigation's results are presented in the table.

The analysis of the results shows that the action of the current pulses only on one of the compressed plates causes the upsetting or half reduction of the typical comb height on both plates with the spreading zone area being little and varying in the range from 6 to 8%.

The appearance of the surface texture after the treatment by the current pulses according to scheme 1 is presented in Fig. 1.

The treatment by the current pulses according to scheme 2 causes substantial changes in the texture of the contact surfaces. The appearance of the texture is changed: the initially streaky texture becomes mixed with the appearance of swirls (see Fig. 2). The height of the microroughnesses reduces by up to ~75% and is attended by the merging of the spreading zones of the separate roughness projections with the total area of the spreading zones being the highest and attaining

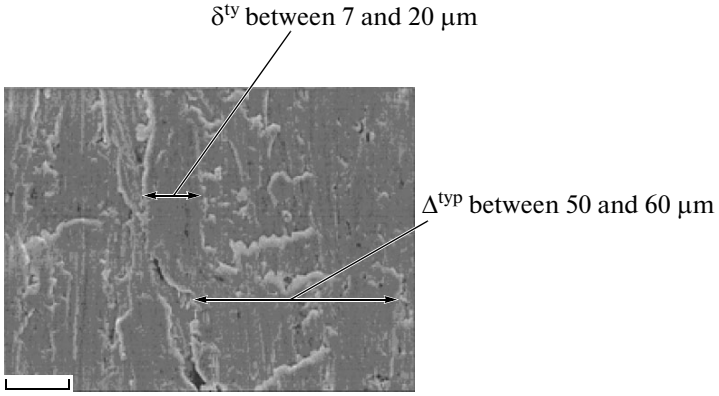


**Fig. 2.** The surface texture of the plate of steel 20 after treatment by the current pulses according to the scheme 2 ×1000.

values from 65 to 70% for the upper plate and from 55 to 65% for the lower one.

Thus, the analysis of the surface texture changes ($S_1$, $H_1$, δ) for the two different treatment schemes shows that the most favorable changes of the surface texture for the formation of the physical contact and welded joint occur at the treatment according to scheme 2 (the treatment by the current pulses at the contact zone and, in turn, through both compressed plates) with the reduction of the height of the microroughnesses amounting to 75% and the total area of the zones of the plate surface spreading being the largest (from 65 to 70% of the total contact surface area).

It should be noted that such intensive plastic deformation of the boundary layers causes not only the formation of the physical contact between the surfaces but also favors the activation of the surfaces, as it is known [2] that, in the process of the welding of uniform metals, the activation of both contact surfaces starts during their approaching each other at the contact of the separate microprojections due to the joint plastic deformation.

## CONCLUSIONS

It is shown that the treatment of the deformation zone of the precompressed metal plates by current pulses with a density of ~$10^9$ A/m$^2$ and a duration of about $10^{-4}$ s intensifies the plastic deformation in this region and favors the activation of the contact surfaces.

It is found that the greatest effect from the viewpoint of the formation of the largest physical contact area occurs in the case of the current passage along the contact zone and, in turn, through both plates with the reduction of the height of the microroughnesses amounting to ~75% and the total area of the zones of the plate surface spreading being in the range from 65 to 70% of the total contact surface area.

## REFERENCES

1. Krasulin, Yu.L., *Vzaimodeistvie metalla s poluprovodnikom v tverdoi faze*, (Interaction of Metal with Semiconductor in Solid State), Moscow: Nauka, 1971.

2. Karakozov, E.S., *Svarka metallov davleniem*, (Pressure Welding of Metals), Moscow: Mashinostroenie, 1986.

3. Troitskii, O.A., Baranov, Yu.V., Avraamov, Yu.S., and Shlyapin, A.D., *Fizicheskie osnovy i tekhnologiya obrabotki sovremennykh materialov*, (Principal Physics and Process Engineering of Modern Materials), vol. 1, Moscow–Izhevsk, 2004.

ISSN 1068-3755, Surface Engineering and Applied Electrochemistry, 2010, Vol. 46, No. 3, pp. 218–222. © Allerton Press, Inc., 2010.
Original Russian Text © A.I. Grigor'ev, S.O. Shiryaeva, N.A. Petrushov, M.V. Volkova, 2010, published in Elektronnaya Obrabotka Materialov, 2010, No. 3, pp. 22–27.

ELECTRICAL PROCESSES
IN ENGINEERING AND CHEMISTRY

# Instability of the Lateral Surface of Strongly Charged Jets in a Collinear Flow of Material Environment

**A. I. Grigor'ev, S. O. Shiryaeva, N. A. Petrushov, and M. V. Volkova**

*Yaroslavl State University, ul. Sovetskaya 14, Yaroslavl, 150000 Russia*

*e-mail: grig@uniyar.ac.ru*

Received January 19, 2010

**Abstract**—On the basis of the analysis of the dispersion equation for nonaxisymmetric capillary waves with an azimuthal number equal to two on a surface of a charged cylindrical jet of an ideal incompressible conductive fluid, it is shown that the influence of the flow has a destabilizing character. The instability of the nonaxisymmetric waves with an azimuthal number equal to two has a threshold character based on both the speed and on size of the electrical charge per unit of length of the jet.

**DOI:** 10.3103/S106837551003004X

## INTRODUCTION

The phenomenon of liquid electrodispersion is widely used in engineering and technology, and it is sufficiently studied experimentally and theoretically (see, for example, Zora [1–7] and the bibliography therein). Nevertheless, some issues related to the phenomenon discussed remained outside of the studies. In particular, this applies to the characteristics of the electrostatic decay into individual drops of very strongly charged jets, especially taking into account the interaction of capillary waves on the surface of a moving jet with a stationary environment. In accordance with [8–9], the presence of the relative motion of the jet and the environment leads to the destabilization of the jet in terms of the implementation of the capillary aerodynamic collapse, which occurs at sufficiently high speeds [7]. However, the influence of the motion of a strongly charged jet relative to the environment at its collapse (at the electrostatic instability of its lateral surface) has not been investigated. The phenomenon of electrostatic instability on the lateral surface was observed experimentally in [10–11], and, in [12–13], a theoretical model is developed . Therefore, it seems actual to investigate the peculiarities of the implementation of the electrostatic nonstability of a charged jet moving with respect to a dielectric material environment. This review addresses this problem.

### *1. The Mathematical Formulation of the Problem*

Consider the problem of the investigation of the stability of capillary waves on a uniformly charged (with a surface charge density $\chi$) cylindrical surface (with radius $R$) jet of a perfectly conducting incompressible ideal fluid with density $\rho_2$ and the coefficient of interfacial tension $\sigma$. Let the jet move at a speed $U_0 \| e_z$ ($e_z$—the longitudinal coordinates) in an ideal incompressible dielectric medium with the density $\rho_1$ and the dielectric constant equal to unity. The problem will be solved in the inertial reference system related to the symmetry axis of the jet and moving with the jet at the speed $U_0$ in cylindrical coordinates, where $e_z$ coincides in direction with $U_0$ and with the axis of symmetry of the unperturbed (by capillary wave motion) cylindrical surface of the jet. All consideration will be given in dimensionless variables, in which $R = \rho_2 = \sigma = 1$ and the surface interfaces perturbed by the capillary wave motion are described by the relation

$$F(r, z, \varphi, t) = r - 1 - \xi(z, \varphi, t) = 0, \quad |\xi| \ll 1,$$

where $\xi(z, \varphi, t)$ is a small perturbation of the cylindrical surface of the jet, and $\varphi$ is the azimuthal angle.

The full mathematical formulation of the problem has the form

$$\operatorname{div} u_1 = 0; \quad \operatorname{div} u_2 = 0; \quad \Delta\Phi = 0;$$

$$\partial_t u_1 + (u_1\nabla)u_1 = -\frac{1}{\rho}\nabla p_1; \quad \partial_t u_2 + (u_2\nabla)u_2 = -\nabla p_2;$$

$$r \longrightarrow 0: \quad u_2 \longrightarrow 0;$$

$$r \longrightarrow \infty: \quad u_1 \longrightarrow -U_0; \quad \nabla\Phi \longrightarrow 0;$$

$$r = 1 + \xi: \quad \frac{dF}{dt} = 0; \quad nu_1 = uu_2 = u_n;$$

$$p_2 - p_1 + p_E - p_\sigma = 0; \quad \Phi(r, t) = \Phi_s(t),$$

where $u_j \equiv u_j(r, t)$ are the velocity fields of the fluid flow in the environment ($j = 1$) and in the jet ($j = 2$); $p_j \equiv p_j(r, t)$ is the hydrodynamic pressure in the environment ($j = 1$) and in the jet ($j = 2$); $p_E$ and $p_\sigma$ are the pressure of the electrical forces and the pressure of the forces of the surface tension on the interfaces, respectively; $\Phi \equiv \Phi(r, t)$ is the potential of the electrostatic field; $\Phi_s(t)$ is the potential of the surface of the jet; $n$ is the unit vec-

tor normal to the surface of the jet; and ρ is the dimensionless density of the environment.

As additional conditions, we assume the following: the condition of constancy of the volume of the jet falling to one wavelength λ (in the single-wave deformation of the interface):

$$\int_V dV = \pi\lambda; \quad V = \{0 \le r \le 1 + \xi(z, \varphi, t);$$

$$0 \le \varphi \le 2\pi; \quad z_0 \le z \le z_0 + \lambda\}$$

and the condition of the conservation of the charge on a segment of the jet's length λ:

$$\int_S \frac{1}{4\pi} n \bullet \nabla\Phi dS = 2\pi\chi\lambda; \quad S = \{r = 1 + \xi(z, \varphi, t);$$

$$0 \le \varphi \le 2\pi; \quad z_0 \le z \le z_0 + \lambda\}.$$

### *2. The Dispersion Equation*

The problem formulated is naturally solved by analogy with how it was done, for example, in [5, 12–13]. Unknown expressions for the surface perturbation of the jet $\xi(\varphi, z, t)$, the hydrodynamic potentials of the currents in the environment $\psi_1(\vec{r}, t)$ and in the drop $\psi_2(\vec{r}, t)$, and for the electrostatic potential $\Phi(\vec{r}, t)$ can be written as follows [5]:

$$\xi(\varphi, z, t) = a\exp(ist)\exp(ikz + im\varphi);$$

$$\psi_1(\vec{r}, t) = b\exp(ist)\exp(ikz + im\varphi)K_m(kr);$$

$$\psi_2(\vec{r}, t) = c\exp(ist)\exp(ikz + im\varphi)I_m(kr);$$

$$\Phi(\vec{r}, t) = d\exp(ist)\exp(ikz + im\varphi)K_m(kr),$$

where $I_m(kr)$ and $K_m(kr)$ are modified Bessel functions of first and second kind of order $m$ [14]; $m$ is the azimuthal parameter; $s$ is the frequency of the capillary waves in the general complex; and $a$, $b$, $c$, and $d$ are unknown coefficients. Substituting the draft solutions in the system of boundary conditions of the problem, we can obtain the dispersion equation for waves with the azimuthal number $m = 2$ in the form

$$s^2 - \frac{2\delta}{\beta}s - \frac{\kappa}{\beta} = 0,$$

$$\beta(k) \equiv \rho h^{-1} - g^{-1} = \frac{\rho g - h}{gh}; \quad \delta(k, U_0) \equiv k\rho U_0 h^{-1};$$

$$\kappa(k, \chi, U_0) \equiv \{[-3 - k^2 - w(1 + h)] - Wek^2 h^{-1}\};$$

$$h(k) \equiv \frac{kK_2'(k)}{K_2(k)} = 2 - \frac{kK_3(k)}{K_2(k)};$$

$$g(k) \equiv \frac{kI_2'(k)}{I_2(k)} = 2 + \frac{kI_3(k)}{I_2(k)};$$

$$w \equiv 4\pi\chi^2; \quad We \equiv \rho U_0^2.$$

The solutions of the dispersion equation have the form

$$s_{1,2} = \frac{\delta}{\beta} \pm \sqrt{\left(\frac{\delta}{\beta}\right)^2 + \frac{\kappa}{\beta}};$$

or

$$s_{1,2} = \frac{g}{(\rho g - h)} k\rho U_0 \pm \sqrt{\left[\frac{gk\rho U_0}{(\rho g - h)}\right]^2 + \frac{[-3 - k^2 - w(1 + h)] - Wek^2 g}{(\rho g - h)}}. \quad (1)$$

### *3. Discussion of the Obtained Results*

When the change of the physical parameters of the system occurs, the waves on the surface interfaces will maintain their stability, while the frequencies $S_{1,2}$ remain real, that is, until the radical expression in (1) is positive. When the radical expression becomes negative, the frequencies $S_{1,2}$ will have an imaginary part, and they will form a pair of complex conjugate roots. Herewith, the amplitude of the wave with the negative imaginary part of the frequency $\sim\exp[i(\mathrm{Re}s - i\,|\mathrm{Im}\,s|)\,t] \sim \exp[|\mathrm{Im}s|\,t]\exp[i\mathrm{Re}s\,t]$ will begin to increase exponentially and the amplitude will increase in time with the increment $\gamma \equiv |\mathrm{Im}s|$, which leads to the disintegration of the jet in to separate drops. The amplitude of the wave with the positive imaginary part of the frequency will be exponentially damped with the increase in time.

Note that the coefficient $g$ is always positive (at that, $g > 2$), the coefficient $h$ is always negative, and $h < -2$. Note also that, for a liquid jet in a gaseous environment ($p \sim 0.001$) with any reasonable speeds ($U_0 \le 1000$ sm/s [15]), for waves with the wave numbers of interest in terms of the electrostatic fragmentation of the jet ($k \sim 1$), the second term under the radical in (1) is usually negative and actually determines the growth of the instability increment.

By equating in (1) the radical expression to zero, we obtain the critical condition of the transition from stable to unstable waves:

$$\rho k^2 We + \left[(-3 - k^2 - w(1 + h))\frac{h}{g} - k^2 We\frac{1}{g}\right](\rho g - h) = 0. \quad (2)$$

From (2), it's easy to find the critical value of the parameter *We* for the initiation of the instability:

$$We = \frac{[-3 - k^2 - w(1 + h)](\rho g - h)}{k^2}. \quad (3)$$

For an uncharged jet at

$$We \ge \frac{(3 + k^2)(\rho g - h)}{k^2},$$

there will be realized the aerodynamic instability of the lateral surface of the jet [7]. From (3), it's easy to see

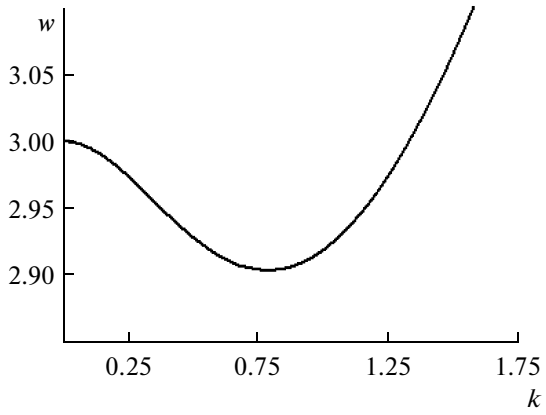


**Fig. 1.** The dependence of the critical (for the start of the implementation of the electrostatic instability of the lateral surface of the jet in a vacuum) value of the dimensionless charge parameter $w$ on the dimensionless wave number $k$.

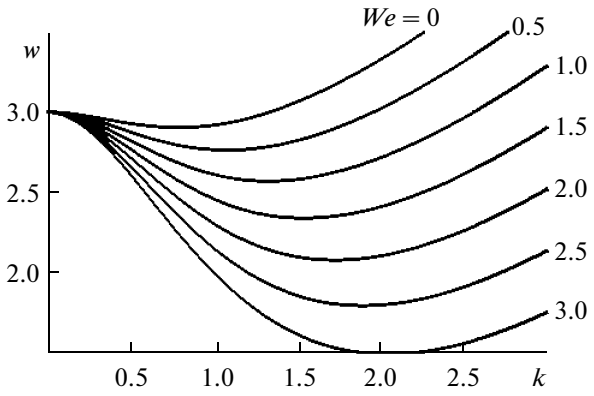


**Fig. 2.** The dependences of the critical (for the start of the implementation of the mixed electrostatically aerodynamic instability of the lateral surface of the jet in a vacuum) parameter value $w$ on the dimensionless wave number $k$ plotted for different values of the parameter $We$.

that, with increasing of $\chi$, the surface density of the electric charge on the boundary interfaces (the parameter $w$) and the critical value of the velocity of the stationary moving $U_0$ for the beginning of the collapse of the jet (the parameter $We$) decrease and at

$$w = -\frac{(3+k^2)}{(h+1)} \equiv \frac{(3+k^2)}{(|h|-1)} \qquad (4)$$

vanish. The value of the parameter $w$, which is defined by (4), is critical for the implementation of the electrostatic instability of the lateral surface of the jet in the absence of the flow of the material environment (in vacuum). The corresponding dependence $w(k)$ is shown in Fig. 1 and located in full agreement with the results of earlier studies [5, 12–13]. If the environment's stream is collinear to the jet, the critical value $w$ is determined by the relation

$$w = \frac{\dfrac{k^2 We}{pg-h} - (3+k^2)}{(h+1)} = \frac{(3+k^2) - \dfrac{k^2 We}{pg+|h|}}{(|h|-1)}. \qquad (5)$$

Figure 2 shows the dependences $w = w(k)$ calculated by (5) at fixed values of the parameter $We$. From the figure, it is easy to see that, with an increase in the parameter $We$, the minimum value of the charge parameter $w$ at which the mixed electrostatically aerodynamical instability of the lateral surface of the jet is realized is reduced, and the value of the wave number of the corresponding wave increases. This fact is important because, in the absence of a flow collinear to the jet of the external material environment, the minimum value of the charge parameter for the jet conduction (as shown in Fig. 1) $w \approx 2.905$ and by the estimation in [5,13] is very close to the limit in terms of the electrical breakdown of air. It should be noted that, according to the foregoing, a value of the parameter $We$ noticeably larger than unity in the phenomenon of electrodispersion is also not realistic. However, the combination of two parameters ($w \approx 2$ and $We \approx 2$) allows us to reconcile the results of the experimental observations with the results of the theoretical analysis and with common sense.

From Fig. 3a, which shows the plots of the dependence of the value of the unstable increment of the nonaxisymmetric waves with $m = 2$ on the interfaces on the wave number $k$ at $w = 0$ and several fixed values of the parameter $We$, we can see that, with increasing of the parameter $We$, the width of the area of the wave numbers corresponding to the unstable waves (the area of implementation of the aerodynamic instability of the lateral surface of the jet) is expanding, and the value of the wave number corresponding to the wave with the maximum increment is shifted to the area of larger values of the wave numbers. We also see that, in the absence of an electric charge on the jet, the instability of the lateral surface of the jet is realized only when the velocity values correspond to the very large parameter values $We \geq 5.215$; this is in agreement with the experimental data in [7,16]. When the charge parameter $w$ is not null (see Fig. 3, b–d), the crucial velocity value for the realization of the instability of the lateral surface of the jet (the parameter $We$) decreases, and, at $w \approx 2$, the value of the parameter $We$ reaches values observed in experiments on electrodispersion [15]: $We \leq 2$ (see Fig. 3, c–d).

Figure 4a shows graphs of the dependence of the value of the instability increment of the nonaxisymmetric waves with $m = 2$ on the interfaces on the wave number $k$ at $We = 0$ and several fixed values of the parameter $w$. At $We = 0$, we are dealing with purely electrostatic instability of the lateral surface of the jet, which is implemented in full agreement with [12–13] at $w \geq 2.905$ (see Fig. 1). At increasing of the velocity of the relative motion of the jet and the material environment (with increasing of the parameter $We$), the critical value of the parameter $w$ for the starting of the electrostatic instability of the lateral surface of the jet

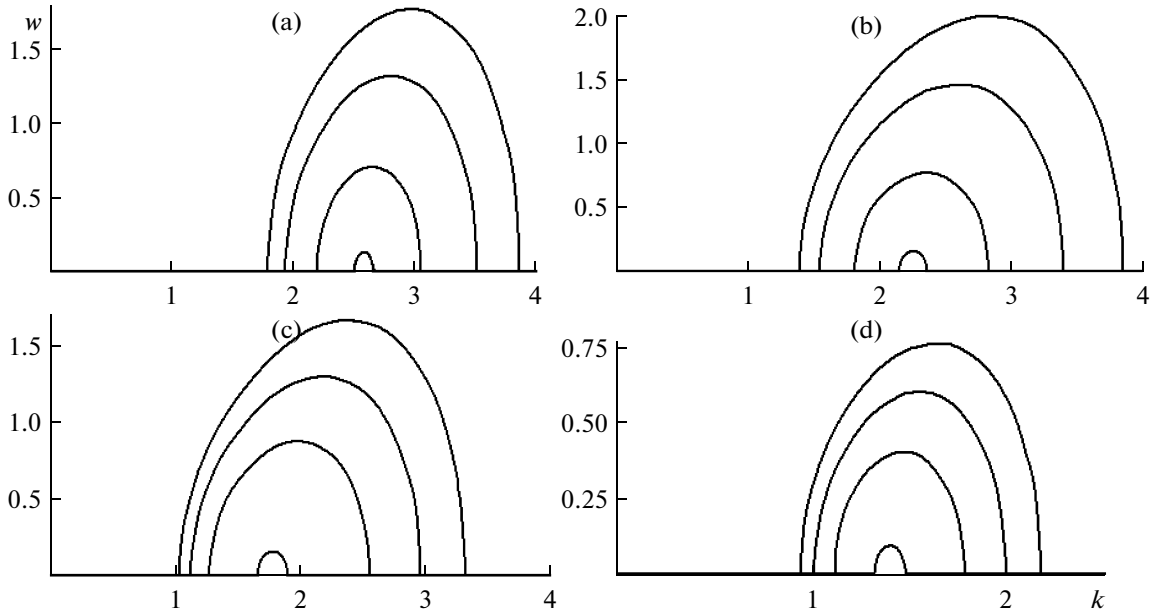


**Fig. 3.** The dependences of the value of the dimensionless instability's increment γ of the nonaxisymmetric waves with $m = 2$ on the dimensionless wave number $k$ plotted at $\rho = 0.001$ for different values of the dimensionless parameters *We* and *w*. From the bottom to top: (a) $We = 5.215$, 5.3, 5.5, and 5.7 ($w = 0$); (b) $We = 3.77$, 3.9, 4.2, and 4.5 ($w = 1$); (c) $We = 2.15$, 2.4, 2.65, and 2.9 ($w = 2$); (d) $We = 1.165$, 1.25, 1.35, and 1.45 ($w = 2.5$)

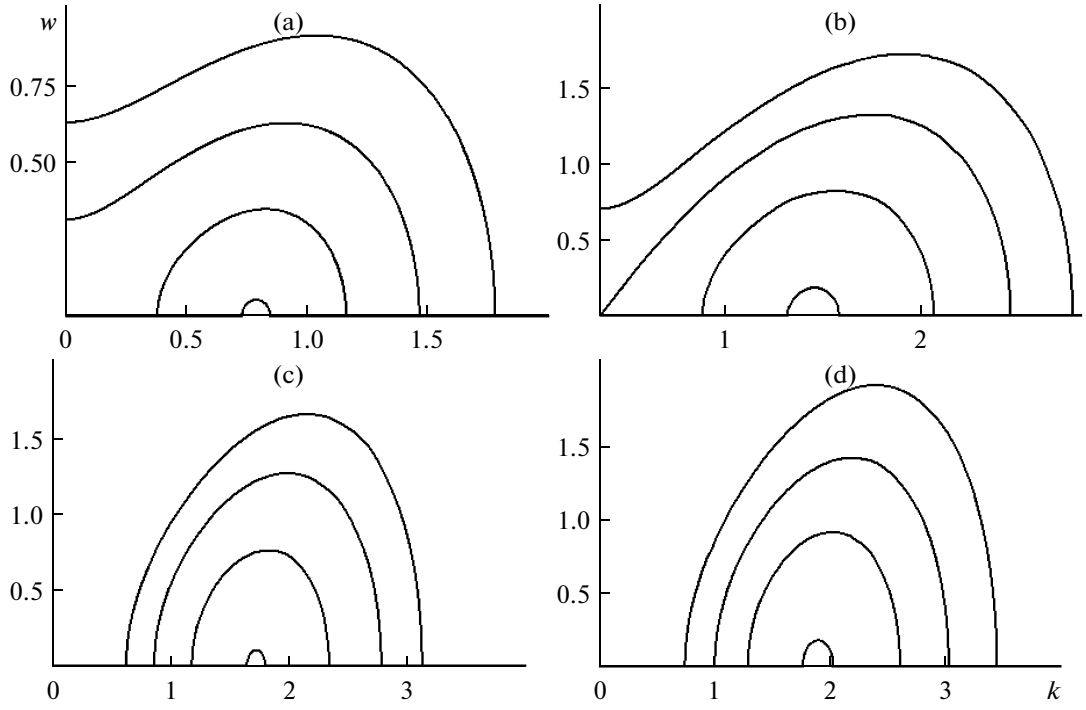


**Fig. 4.** The dependence of the value of the dimensionless instability's increment γ of the nonaxisymmetric waves with $m = 2$ on the dimensionless wave number $k$ plotted at $\rho = 0.001$ for different values of the dimensionless parameters *w* and *We*. From the bottom to the top: (a) $w = 2.905$, 2.95, 3.05, and 3.2 ($We = 0$); (b) $w = 2.58$, 2.75, 3, and 3.25 ($We = 1$); (c) $w = 2.08$, 2.2, 2.4, and 2.6 ($We = 2$); (d) $w = 1.8$, 1.95, 2.15, and 2.4 ($We = 2.5$).

decreases (see Fig. 4, b–d). Figure 4, a–d shows that, at the fixed parameter *We*, with increasing of the parameter *w*, the wave number of the wave with the maximum value of the increment is shifted to the area of higher wave numbers, and the value of the increment increases.

In Fig. 3 a–d and Fig. 4 a–d, it is striking that the instability of the lateral surface of the jet has a threshold character as the largest charge value per unit of length of the jet (the parameter $w$) and the velocity of the environment's flow (the parameter $We$). Thus, when $We = 0$, the electrostatic instability is realized only for large values of the charge (at $w \geq 2.905$), and, for the noncharged jet, the aerodynamic instability of its lateral surface is realized only at very high speeds (at $We \geq 5.215$).

## CONCLUSIONS

The dispersion equation for axisymmetric capillary waves with the azimuthal number $m = 2$ on the charged surface of the jet of an ideal incompressible electrically conducting fluid moving along its axis in an ideal incompressible dielectric environment is derived. It is shown that the influence of the relative motion of the jet and the environment has a destabilizing character. The dispersion equation in two extreme situations—an uncharged jet with blowing of its flow and a charged jet when neglecting the influence of the motion relative to the environment—describes, respectively, the aerodynamic and electrostatic instability of the lateral surface of the jet. The instability of nonaxisymmetric waves with an azimuthal number equal to two has a threshold character as the velocity and the value of the electric charge per unit of length of the jet.

## ACKNOWLEDGMENTS

This work was performed under the thematic plan of the university (Rosobrazovanie grant no. 2.1.1/3776) and the Russian Foundation for Basic Research (project nos. 09-01-00084 and 09-08-00148).

## REFERENCES

1. Buraev, T.K, Vereshchagin, I.P, and Pashin, N.M., Strong Electric Fields in the Technological Processes, *Energiya*, Moscow, 1979, no. 3. pp. 87–105.
2. Entov, V.M., and Yarin, A.L., Results of Science and Technology, *VINITI Ser. "Mehanica gidkosti i gaza"*, 1984, vol. 17, pp. 112–197.
3. Dudnikov, V.G., and Shabalin, A.L., *Elektrogidrodinamicheskie istochniki ionnyh puchkov* (Electrohydrodynamic Sources of Ion Beams (Review), Novosibirsk: Preprint INP 87-63 SB AS USSR, 1987.
4. Fenn, J.B., Mann M., Meng, C.K., et al., Electrospray Ionization for Mass Spectrometry of Large Biomolecules, *Science*, 1989, vol. 246, no. 4926, pp. 64–71.
5. Grigor'ev, A.I., Instabilities of Charged Drops in Electric Fields (Review), *Electron. Obrab. Mater.*, 1990, no. 6, pp. 23–32.
6. Shiryaeva, S.O., Grigoriev, A.I., and Volkova, M.V., *Spontannyi kapillyarnyi raspad zaryagennyh struy* (Spontaneous Capillary Disintegration of Charged Jets), Yaroslavl: Yaroslavsiy Gos. Univ., 2007.
7. Eggers, J., and Willermaux, E. Physics of Liquid Jets, *Rep. Prog. Phys.*, 2008, vol. 71,no. 036601, pp. 1–79.
8. Strutt, J.W. (Lord Rayleigh). On the Instability of Cylindrical Fluid Surfaces, *Phil. Mag.*,1892, vol. 34, no. 5, pp. 177–180.
9. Basset, A.B., Waves and Jets in a Viscous Liquid, *Amer. J. Math.*, 1894, vol.16, pp. 93–110.
10. Cloupeau, M., and Prunet Foch, B., Electrostatic Spraying of Liquids: Main Functioning Modes, *J. Electrostatics*, 1990, vol. 25, pp. 165–184.
11. Jaworek, A., and Krupa, A., Classification of the Modes of EHD Spraying, *J. Aerosol Sci.*, 1999,vol. 30, no. 7, pp. 873–893.
12. Grigor'ev, A.I., Electrostatic Instability of Highly Charged Jets of the Conducting Fluid, *Zh. Tekh. Fiz.*, 2009, vol. 79, no. 4, pp. 36–45.
13. Grigor'ev, A.I., and Shiryayeva, S.O., On the Electrostatic Instability of a Body Charged Jet of Dielectric Fluid, *Electron. Obrab. Mater.*, 2009, no. 6, pp. 35–41.
14. Abramovitz, M., Stigan, I., *Spravochnik po special'nym funkciyam* (Handbook of Special Functions), Moscow: Nauka, 1979.
15. Shiryaeva, S.O., Grigor'ev, A.I., and Sviatchenko, A.A., *Klassifikaciya regimov raboty elektrogidrodinamicheskih istochnikov ionov* (Classification of Modes of Electrohydrodynamic Ion Sources), Yaroslavl: Preprint IM RAS, vol. 25, 1993.
16. Hoyt, J.W., and Taylor, G.I., Waves on Water Jets, *J. Fluid Mech.*, 1977, vol. 83, pp. 119–127.

ISSN 1068-3755, Surface Engineering and Applied Electrochemistry, 2010, Vol. 46, No. 3, pp. 223–229. © Allerton Press, Inc., 2010.
Original Russian Text © V.L. Lanin, N.V. Dezhkunov, A.V. Kotukhov, 2010, published in Elektronnaya Obrabotka Materialov, 2010, No. 3, pp. 28–35.

ELECTRICAL PROCESSES
IN ENGINEERING AND CHEMISTRY

# Application of Ultrasonic Effects in Liquid Media for Fabrication of Nanomaterials

**V. L. Lanin, N. V. Dezhkunov, and A. V. Kotukhov**

*State University of Informatics and Radioelectronics of Belarus, ul. P. Brovki 6, Minsk, 220013 Republic of Belarus*
*e-mail: vlanin@bsuir.by, dnv@bsuir.by*

Received February 9, 2010

**Abstract**—The amplification of sonoluminescence is shown experimentally under the influence of low-frequency ultrasound in the cavitation area generated by a high-frequency field. The generation of microstreams in the boundary layers at the high uniformity of the distribution of the ultrasonic pressure is effective for dispergation of nanoparticles in liquid media.

**DOI:** 10.3103/S1068375510030051

## INTRODUCTION

Composite nanostructured materials on the basis of metals and carbon nanoparticles exhibit many unique properties involving a low friction coefficient, high hardness and durability, electric conductivity, and high corrosion and wear resistance. The structure and properties of nanostructured materials substantially depend on the type and concentration of the nanoparticles in finely dispersed systems [1]. These materials can be used for manufacturing superconductors, protective screens, electric contacts, etc.

The nanostructured materials are prepared by vacuum sputtering, electric arc deposition, plasma-jet hard-facing in an inert gas stream, laser-induced evaporation, and magnetron sputtering [2]. These processes are characterized by high energy consumption. The dimensions of such nanoparticles strongly depend on the process parameters and fall in a wide range of dimensions from 5 to 200 nm.

Nowadays, nanostructured materials are more widely prepared by virtue of methods based on ultrasonic (US) effects arising in liquid media [3]. The first direction is the application of ultrasound for the synthesis and deposition of nanoparticles; the second direction is dispergation of nanoparticles in liquids for disintegration of agglomerates in them.

The action of US radiation is primarily associated with the development of such an effect as acoustic cavitation arising in media at propagation of ultrasound. Cavitation is an affective tool for transformation of the low-density energy of the acoustic wave into the high-density energy linked with pulsations and collapse of cavitation bubbles [4]. For the intensity of the US wave exceeding 2 W/cm$^2$, sonoluminescence arises in liquid media at the large accumulation of cavitation bubbles. This is caused by the fact that, at the moment of the collapse of the cavitation bubbles, the pressure and temperature of the gas reach significant values (up to 100 MPa and 5000–25000 K, according to certain data) [5]. After the cavity's collapse, a spherical quickly decaying shock wave propagates in the adjacent liquid. Since the collapse duration is less than one nanosecond [6], very high rates of the adiabatic heating are created in this process exceeding $10^{11}$ K/s. The collapses of the bubbles also induce microjets in the liquid, whose speed reaches 150 m/s.

The energy of the ultrasonic field is used for the chemical synthesis of nanostructured materials. This research field known as sonochemistry is based on the generation and development of the cavitation process in liquid media and the sonochemical reactions that accompany the cavitation. In intensive cavitation fields, the decomposition of water molecules and the formation of active radicals and oxidants ($H_2O_2$, $O_3$, etc.) occur owing to the high gradients of temperature and pressure (Fig. 1) [7]. Sonochemical methods are used for fabrication of nanostructured amorphous materials, the inclusion of nanoparticles in mesaporous materials, the deposition of semiconductor nanoparticles on the surfaces of polymer and ceramic materials, and the formation of protein micro- and nanospheres.

One of the effective methods used to control the sonochemical reactions is the registration of the sonoluminescence arising in intensive cavitation fields at hypersonic frequencies [8]. Various methods of increasing of the activity of cavitation fields are being intensively developed and studied.

An effective method to increase the cavitation activity is the action by low-frequency (LF) ultrasoud on the cavitation area generated by a high-fequency (HF) field in a pulse-modulated HF field that is generated by HF and LF generators operating simultaneously. The sonoluminescence intensity many times exceeds the sum of the intensities generated by each generator separately [9]. An obvious mechanism of the

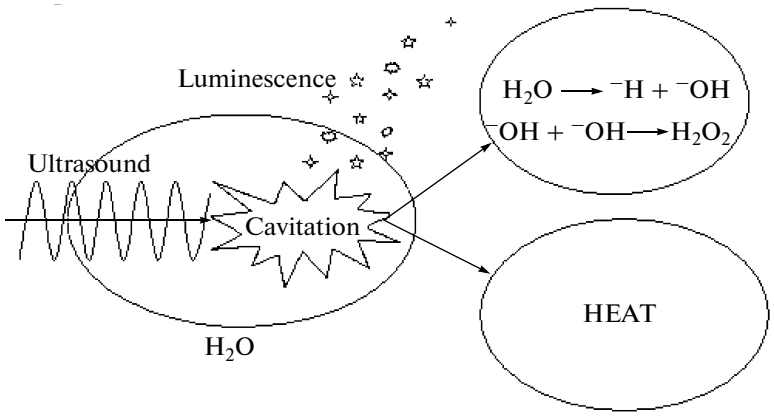


**Fig. 1.** Scheme of the development of sonochemical reactions in liquid media.

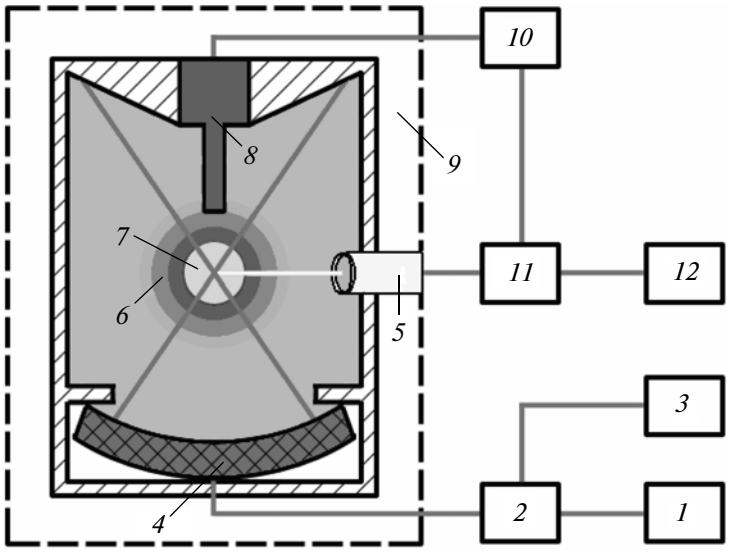


**Fig. 2.** Scheme of the experimental setup. (*1*) US generator, (*2*) modulator, (*3*) pulse generator, (*4*) transducer, (*5*) photomultiplier, (*6*) zone of intensive cavitation, (*7*) focal spot of the projector, (*8*) hydrophone, (*9*) lightproof box, (*10*) preamplifier, (*11*) oscilloscope, (*12*) spectrum analyzer.

increasing of the sonoluminescence in interacting fields is the increase of the sum energy introduced in the liquid when two generators operate and the interference of the fields.

The application of the energy of ultrasonic vibrations proved to be effective for dispergation and dissolution of such unsoluble elements as Al, Ti, Fe, etc., in alloys. The melt and soluble particles are intensively stirred at a constant temperature by virtue of vortex microstreams at frequencies of 20–200 kHz. Metallographic research has shown the considerable solubility of Al, Ti, and Fe in melts [10].

With the aim to dispergate nanoparticles with dimensions less than 100 nm in liquid media, intensive microstreams are induced in boundary layers at frequencies of 1–2 MHz by US generators with power up to 100 W. High-frequency ultrasound is effective in liquid media owing to the following reasons: the wavelength is comparable with the dimensions of the particles, the viscous surface layer is thin, and the forces of the radiation pressure exceed the typical values of the adhesive forces of the particles to the surface [11].

## EXPERIMENTAL METHOD

In this work, the regimes were studied of the action of the energy of low and high frequency ultrasonic radiation that ensures the maximal activity of cavitation in a pulse-modulated field. The scheme of the experimental setup is shown in Fig. 2.

A cylinder of stainless steel with its diameter being 10 cm and height 6 cm was used as the working reservoir. A copper tube was wound at the side wall of the cell through which a thermostatic liquid was pumped.

A piezoelectric focusing transducer with a diameter of 65 mm and a resonance frequency of 880 kHz was mounted through the hole in the bottom of the reservoir using a teflon cap, which was screwed on it.

A window is made at the level of the focal spot of the transducer in the side wall of the reservoir where a light guide of the photomultiplier is inserted. The reservoir end opposite to the transducer is supplied with a conical cap covered inside by sound-absorbing pleated rubber; this ensures a regime close to the regime of a traveling wave. A hydrophone is mounted through the reservoir cap in such a way that its receiving piezoceramic element with a diameter of 2 mm and thickness of 0.25 mm is located behind the focal spot of the transducer at a distance of 25 mm from it.

The output signals of the photomultiplier and hydrophone were preamplified and transmitted to a memory oscilloscope and analyzed using a computer.

The reservoir was filled with the liquid from an auxiliary reservoir through a drain tube in a laminar regime to prevent the capture of gas bubbles during this process. The cell was filled with the processed fluid, which was left to settle for two days. Then, the liquid was degassed under the action of ultrasound for 20 min at the voltage at the transducer of 170 V ($\approx$10 W/cm$^2$). The gas content decreased by 20–25% in comparison with the equilibrium under the action of the ultrasound. This substantially increased the reproducibility of the results, since, after this treatment, the air concentration in the liquid virtually does not change under the ultrasonic action during the experiment. After the degassing, the cell was coved by a cap, and the liquid did not contact with the air.

In the process of the US dispergation of nanoparticles, it is important to form micro- and macrostreams in such a way that they ensure a homogeneous distribution of the nanoparticles in the liquid medium. Acoustical flows of the Schlichting type arise in a liquid medium with a solid surface in the boundary layer with the thickness $\delta$, and they are vortices with the scale $\lambda/4 \times 1.9\delta$. The equations for the normal and tangential velocities of the stream have the form

$$\bar{v}_x = -\frac{v_0^2}{4c_0}(\mu - \mu^2)\sin 2kx, \quad (1)$$

$$\bar{v}_y = -\frac{v_0^2}{4c_0}k\delta\mu^2\cos 2kx, \quad (2)$$

where $v_0$ is the initial flow velocity; $c_0$ is the wave velocity; $k$ is the wave number; $\mu$ is the relative distance ($\mu = y/\delta$); and $x$, $y$ are the current coordinates of the wave front.

The thickness of the acoustic boundary layer $\delta$ is defined by the equation

$$\delta = \sqrt{\frac{\eta}{\pi f}}, \quad (3)$$

where $\eta$ is the viscosity of the melt and $f$ is the frequency of the ultrasonic vibrations.

The condition of the appearance of a standing wave in the bath is that the height of the liquid column is a multiple of $\lambda/2$. The thickness of the acoustic boundary layer for frequencies of 21.0–22.0 kHz amounts to 6–10 mm. Thus, to fabricate nanostructured materials by US activation at dispergation of the particles, it is necessary to use both the microstreams in the near-surface layers of the Schlichting type and the macrostreams in the volume of the bath.

In the process of US dispergation, the main demand on the US technological systems is the high uniformity of the distribution of the US pressure over the volume of the bath. Therefore, a various quantity of packet-type piezoelectric transducers (PPT) with power of 50–100 W are used mounted on the side walls and bottom of the bath in a specified order with their parallel connection with a generator. In this case, the efficiency and operation stability of the transducers depend on the width of the transformation band, since the larger overlap of the amplitude–frequency characteristics of the individual transducers allow them to compensate for the unavoidable dissipation of their natural resonance frequencies.

In comparison with a linear arrangement of packet-type piezoelectric transducers, a modular system of PPT is more promising when the PPT are mounted as a grid with a triangle structure whose side length is a multiple of $n\lambda/\sqrt{3}$, where $n$ are integer numbers $n = 1, 2, 3,...$ and $\lambda$ is the wavelength of the US wave in the liquid medium [12]. The distance between the centers in the group is a multiple of the wavelength $\lambda$ of the US waves propagating in the liquid. The PPT in each group are electrically connected in parallel and plugged to the appropriate channels—A, B, and C—of a modular US generator. This arrangement of the PPT generates a uniform over the area US field at three-phase generation owing to the superposition of the waves generated by the transducers attached to the various channels of the US generator.

The area of the largest acoustic pressure corresponding to the maximum voltage on the transducer consequently shifts from transducer A to B and from the B to C in each group (Fig. 3).

As a result, there arise directed liquid streams from the zone with a larger acoustic pressure to the zone with lesser pressure. Since the motion of the regions occur with a relatively low frequency (100 Hz) in the liquid with a definite viscosity vortex, macrostreams arise, which, along with the microstreams arising in the viscous boundary layer, intensify the processes of the mass transfer and dispergation of the nanoparticles.

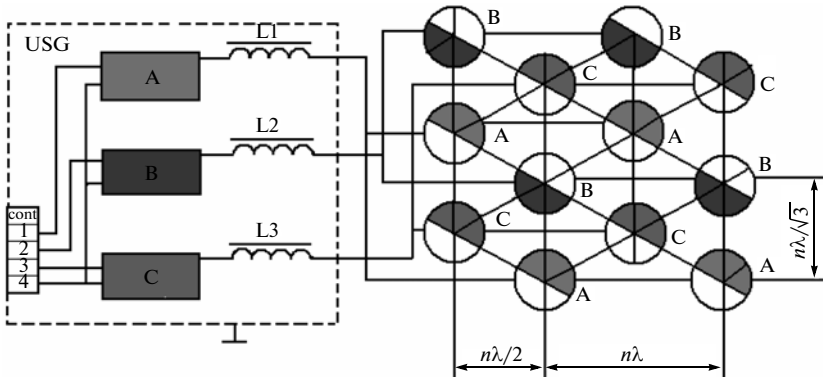


**Fig. 3.** Modular scheme of the generation of US vibrations in liquid media.

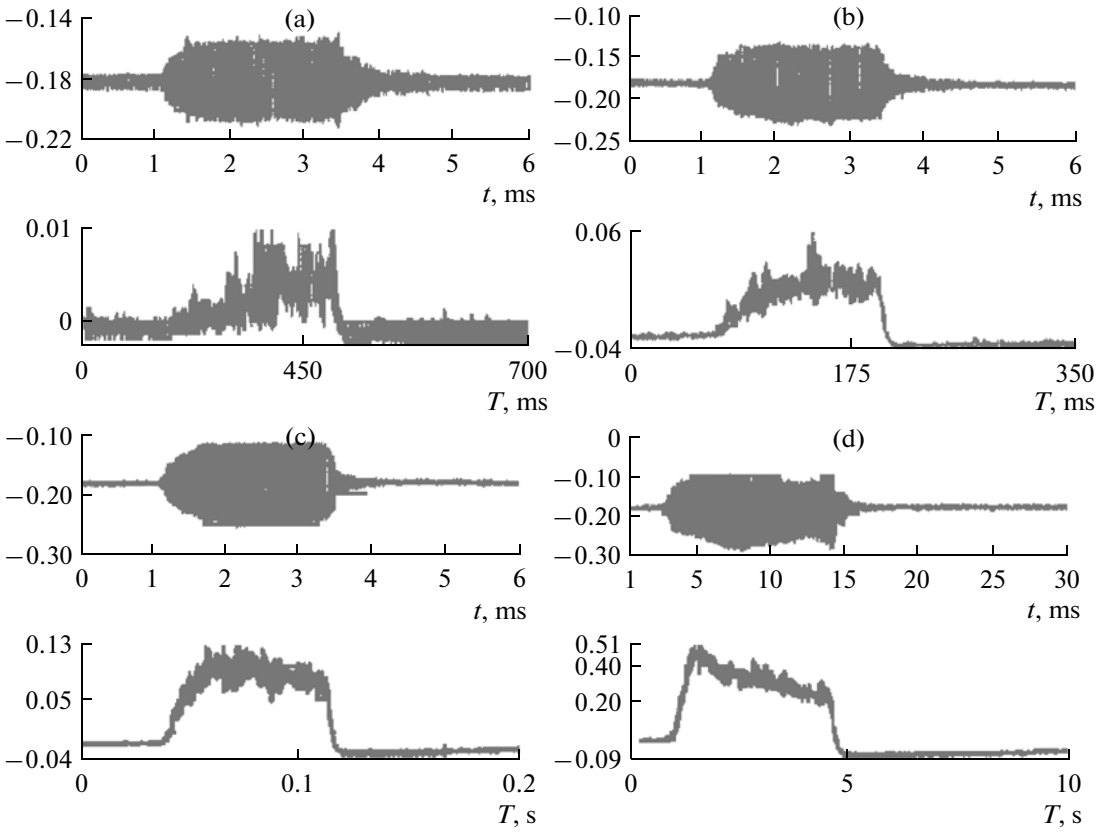


**Fig. 4.** Form of the output signals of the hydrophone and photomultiplier for various $T$, ms. (a) 700, (b) 350, (c) 200, (d) 10; $\tau$ = 3 ms.

## EXPERIMENTAL RESULS AND DISCUSSION

The dependence of the intensity of the sonoluminescence (SL) was studied versus the pulse repetition interval $T$ (starting from 2000 ms in the direction of its decreasing) and versus the pulse duration $\tau$, which increased from 0.1 ms. This interval of variation of $T$ and $\tau$ was chosen with the aim to decrease as far as possible the influence of the previous experiment on the result of the subsequent one. In the time interval between the two consecutive pulses, the liquid relaxes toward its initial state. For shorter pulses and larger time intervals $T - \tau$ between the pulses, the liquid has sufficient time to relax closer to its initial state in the interval between the two consecutive pulses of the US vibrations (Fig. 4). The measurements were performed after a 10 s acquisition time for the chosen meanings of $T$, $\tau$, and $U$. The time interval between the two measurements was 30 s, and the time of settling of the liquid after a set of measurements was 30 min.

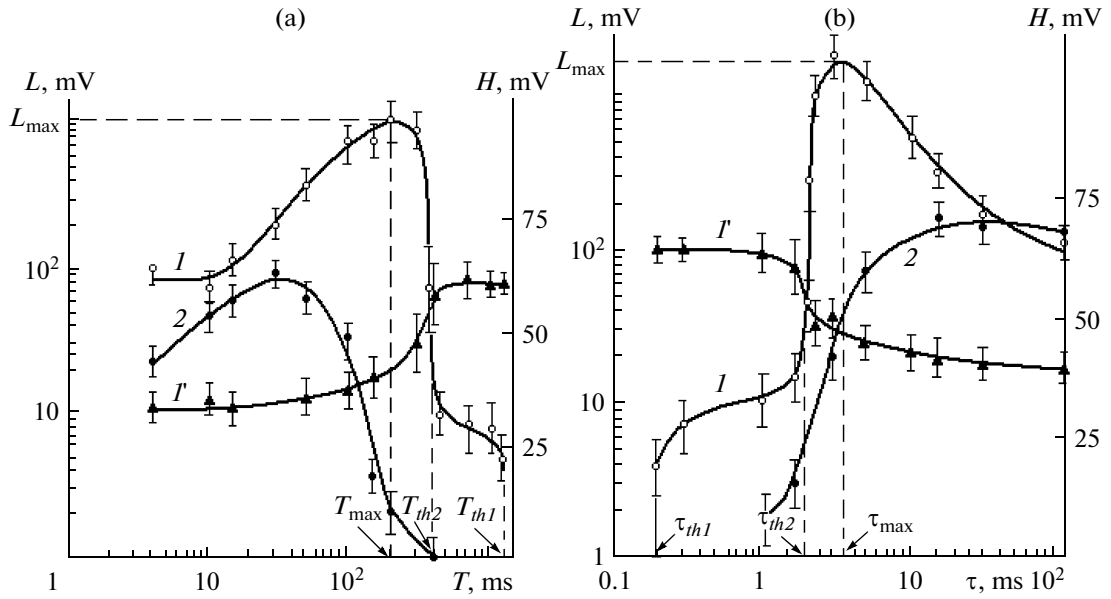


**Fig. 5.** Dependences of the SL intensity (curves *1*, *2*) and the output hydrophone signal H (curve *1'*) versus the pulse repetition interval $T$ (a) and pulse duration τ (b) of the US field: τ = 3 ms, $U$ = 120 V (1) and 55 V (2). The values of $T_{th1}$, $T_{th2}$, $T_{max}$ and $\tau_{th1}$, $\tau_{th2}$, and $\tau_{max}$ are shown for curve *1*.

Figure 5 shows the characteristic dependences of the SL intensity (curves *1* and *2*) in distilled water at 23°C and the dependences of the hydrophone output signal (curve *1*) versus the pulse repetition interval $T$ (Fig. 5a) and the pulse duration τ (Fig. 5b) of the ultrasound. When the $T$ is sufficiently high (>2000 ms), the SL is absent. When the pulse repetition interval $T$ decreases at constant $U$ and τ, the SL arises at some threshold $T = T_{th1}$. At the outset, it increases slowly; then, starting from certain critical meanings $T = T_{th2}$, considerable increasing of the slope of the dependence $L(T)$ is observed. The SL intensity reaches its maximum and starts to decrease, approaching some limiting value. At the high intensities of the ultrasound (curve *1*), the intensity of the SL at $T = T_{th2}$ exhibits explicitly stepwise (threshold) increasing; the decreasing of $T$ by 15–20% leads to the increasing of $L$ approximately by two orders of magnitude.

Thus, the two thresholds of the cavitation can be observed. The first $T_{th1}$ corresponds to the initiation of the SL and the second $T_{th2}$ to the sharp increase of its intensity. When the period decreases, the intensity of the signal registered by the hydrophone first only slightly changes; or more accurately, it changes in the limits of the experimental error. When $T = T_{th2}$, a fast decrease of the output hydrophone signal is observed; this suggests a corresponding increasing of the absorption of the ultrasound.

The value of $L$ changes in the same way when the pulse duration τ increases at constant $T$ and $U$ (Fig. 5b). As in the first case, two thresholds $\tau_{th1}$ and $\tau_{th2}$ can be observed. The SL arises for $\tau = \tau_{th1}$; a sharp change of the slope of the dependence $L(\tau)$ for $\tau = \tau_{th2}$ (curve *1*) and increasing of the absorption of the ultrasound in the cavitation zone (curve 2) are observed. The values of $T$ and τ corresponding to the maximum values of the SL intensity $L_{max}$ will be further denoted as $T_{max}$ and $\tau_{max}$, respectively.

Figure 6 shows the dependences of the SL intensity versus the amplitude of the voltage on the projector in distilled water at 23 °C for various periods $T$. It is seen that the threshold of the inertial cavitation increases with the increasing of $T$, i.e., with the increasing of the relative pulse duration of the ultrasound. High intensities of the ultrasound are necessary for the cavitation

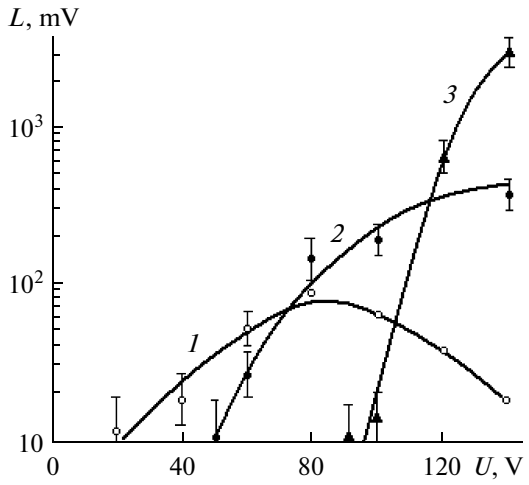


**Fig. 6.** Dependences of the SL intensity versus the voltage on the projector for various periods $T$, ms. (*1*) 10, (*2*) 50, (*3*) 250; τ = 3 ms.

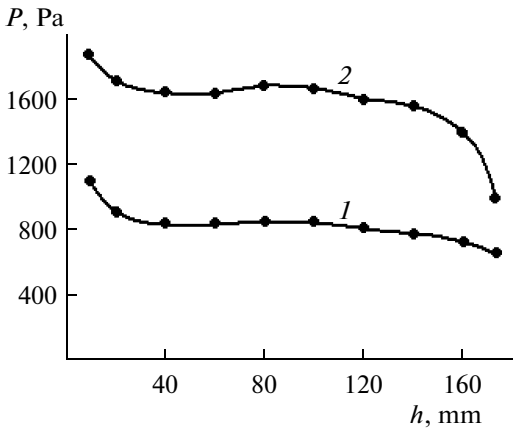


**Fig. 7.** Distribution of the pressure of the US field in the center of the bath. (*1*) The holder with the workpieces is inserted, (*2*) without the holder.

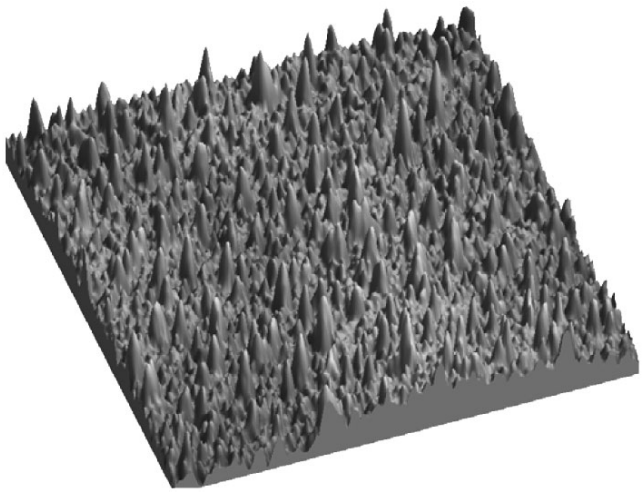

**Fig. 8.** ASM image of the surface of the coating of copper–carbon nanoparticles.

nuclei to reach the dimensions on the order of the resonance ones and start to collapse at large $T$. The maximum of the cavitation activity shifts to the range of higher intensities of the ultrasound. The maximal value of the SL intensity also increases when the period $T$ increases.

The probable mechanisms of the amplification of the sonoluminescence in the interacting LF and HF US fields can be as follows:

(1) The generation of combination frequencies and the expansion of the spectral composition of the resulting field leads to the expansion of the range of the dimensions of the bubbles involved in the cavitation process.

(2) The decreasing of the threshold of the HF cavitation during the discharge half-period of the LF field, which is quasi-static with respect to the HF field, induces the increasing of the quantity of the bubbles cavitating in the HF field.

(3) The large bubbles generated by the LF field exert a force action on the clusters of HF bubbles, prevent their formation, and increase the uniformity of the distribution of the bubbles over the volume of the cavitation zone. Owing to this, more optimal conditions for the collapse of the cavities are ensured, and the cavitation activity increases.

(4) When collapsing, the cavitating bubbles disintegrate into small fragments; their number can reach 10 or larger. The fragments of the bubbles collapsing under the action of the LF field can serve as the cavitation nuclei in the HF field. Since these nuclei contain considerably less air than the stable bubbles, which exist in the liquid, they collapse in the HF field with a larger velocity.

The nonuniformity was estimated of the cavitation pressure in the working volume of the US bath with a modular arrangement of projector systems. The measurements were performed using a cavitation indicator in the center of the bath at various distances from the projector in the presence of a holder with workpieces or without it (Fig. 7).

The holder with workpieces present in the bath decreases the value of the cavitation pressure and reduces the nonuniformity of the cavitation field. The nonuniformity of the distribution of the cavitation field amounts on average to 3–4% over the area of the bath and 6–10% along its depth.

The composite material, which contains carbon nanoparticles as a dispersed phase, fabricated by electrodeposition possesses a fine-crystalline structure; this ensures its high mechanical properties and stable electric resistance. The image of the surface of the film of copper–carbon nanoparticles obtained by virtue of a Microscan atomic-force microscope (ASM) with the field dimensions of 600 × 600 nm is shown in Fig. 8. The average value of the microrelief height in the film amounted to 97.81 nm.

The introduction of 0.5–15 g/l of nanoparticles into the electrolyte by the method of US dispergation lead to the fabrication of a finer coating and decreasing of the dimensions of the mosaic blocks from 33.4 to 29.5 nm at the density of the current of 3 A/dm$^2$. Depositions with finer grains were probably prepared, since the absorbed particles prevent the increasing of the grain dimensions. The nanoparticles are included in the metal matrix during the deposition and facilitate the improvement of the wear resistance of the coatings. The nanoparticles in the form of spheres of the carbon atoms, while present on the surface of thin friction materials, serve as a lubricant and in this way decrease the coefficient of friction. The wear resistance of the composite film coatings depends on the content of nanoparticles in the electrolyte and by 2 to 4 times exceeds the wear resistance of conventional

coatings. The reasons for the increasing of the wear resistance of the composite coatings are as follows: the closer packing of the crystals and increasing of the bearing surface of the layers, since their profile becomes smoother.

## CONCLUSIONS

Thus, the application of the US effects arising in liquid media is promising for the fabrication of nanostructured materials both at sonochemical synthesis and for dispergation of nanoparticles in liquids with the aim to disintegrate their agglomerates. The action of the low-frequency ultrasound on the cavitation zone generated by the high-frequency field is effective with the aim to increase the cavitation efficiency. The range of dimensions of the bubbles involved in the cavitation process increases owing to the interference and also to the generation of combination frequencies and the expansion of the spectrum of the resulting field. At the ultrasonic dispergation of nanoparticles in liquid media, it is effective to generate microstreams in the boundary layers of the Schlichting type at high uniformity of the distribution of the US pressure over the volume of the medium.

## ACKNOWLEDGMENTS

This research was supported by the Belarus Republican Fund for Basic Research (project no. B08R–115).

## REFERENCES

1. Agarwal, A., Rea, K., Wannaparhun, S., et al., Aluminum-Based Nanostructured Composite Coatings: Processing, Microstructure and Wear Behavior, in *Surface Engineering in Materials Science*, Warrendale: TMS, 2003, pp. 81–89.
2. Fahrner, W.R, *Nanotechnology and Nanoelectronics: Materials, Devices, Measurement Techniques*, New York: Springer, 2005.
3. Mason, T.J., and Lorimer, J.P., *Applied Sonochemistry: Uses of Power Ultrasound in Chemistry and Processing*, Wiley, 2002.
4. Leighton, T.G., *The Acoustic Bubble*, London: Academic Press, 1994.
5. Margulis, M.A., *Sonochemistry and Cavitation*, London: Gordon and Breach, 1996.
6. Hiller, R., Putterman, S.J., and Barber B.P., Spectrum of Synchronous Picosecond Sonoluminescence, *Phys. Rev. Lett.,* 1992, vol. 69, pp. 1182–1184.
7. Gedanken, A., Using Sonochemistry for the Fabrication of Nanomaterials, *Ultrasonic Sonochem.*, 2003, no. 10, pp. 47–51.
8. Harada, H., Yoshida, H., and Kato, H., The Intensity of MBSL and Chemical Power in Pure Water with Various Dissolved Gases at 2.4 MHz, *Proc. 11th Meeting of the Eur. Soc. of Sonochemistry,* 2008, La Grande-Motte, France, 2008, pp. 163–164.
9. Dezhkunov, N.V., Francescutto, A., Ciuti, P., Mason, T. J. et al., Enhancement of Sonoluminescence Emission from a Multibubble Cavitation Zone, *Ultrason. Sonochem.*, 2000, no. 7, pp. 19–24.
10. Abdel-Reihim, M., and Reif, W., Effects of Ultrasonic Vibrations on the Dispersions of Elements in Melts, *Metals*, 1988, vol. 37, no. 9, pp. 873–877.
11. Qi, Q., and Brenton, G.J., Mechanism of Removal of Micron-Sized Particles by High-Frequency Ultrasonic Waves, *IEEE Trans. Ultrason., Ferroelectr. Frequency Control*, 1995, vol. 42, no. 4, pp. 619–629.
12. Lanin, V.L., and Tomal', V.S., Ultrasonic Technologies of Fabrication of Nanomaterials, *Perspektivn. Mater.*, no. 6, part 1, 2008, pp. 269–271.

ISSN 1068-3755, Surface Engineering and Applied Electrochemistry, 2010, Vol. 46, No. 3, pp. 230–234. © Allerton Press, Inc., 2010.
Original Russian Text © S.A. Khainatskii, 2010, published in Elektronnaya Obrabotka Materialov, 2010, No. 3, pp. 36–42.

ELECTRICAL PROCESSES IN ENGINEERING AND CHEMISTRY

# On the Equations of State for Metals in the Electric Explosion Models of Conductors

**S. A. Khainatskii**

*Institute of Pulse Processes and Technologies, Ukrainian National Academy of Sciences*
*pr. Oktyabr'skii 43-A, Nikolaev, 54018 Ukraine*
*e-mail: iipt@iipt.com.ua*

Received January 11, 2010

**Abstract**—An analytical wide-range equation of state for metals giving good agreement with the experimental results in the vast range of parameters of the state of matter is developed.

**DOI:** 10.3103/S1068375510030063

## INTRODUCTION

The efficient application of the electric explosion of conductors in the accomplishment of various technological processes and for experimental procedures, the possibility of using this phenomenon as a promising method of examining a metal's critical states [1], and determining the temperature dependency of the kinetic coefficients [2] in a wide range of temperatures and pressures necessitates the development of a fairly reliable model to display the process of the electric explosion. Experimental and theoretical investigations of the conductor's destruction during the current passage showed that, with respect to the current density, there are two models to describe the phenomenon: the MHD model and a model with the thermal processes being predominant [3]. In both models, the determination of the substance's properties is essential, i.e., the thermodynamic functions of it when the metal of a conductor undergoes various phase transformations from solid to plasma states. In this respect, the determination of the role of the physical factors that (depending on the load rate) provide for the valid description of the electric explosion using one or another model largely depends on the results of the construction and application of real equations of state [4–8]. The most perfect among the modern wide-range equations of states of metals (those of V.E. Fortov with coauthors [7] and I.L. Iosilevskii [8] et al.) are found to have an interpolation structure and, hence, in certain transitional regions, they are insufficiently accurate. Therefore, it is of crucial importance to develop more precise formulas for the calculation of the thermodynamic parameters in the transitional regions. The thermal equation of state of metals was earlier presented by us in [9] for the dynamic problems in simulating the conductor destruction upon the electric explosion. Its form and coefficients were obtained from the experimental results of a number of authors; i.e., this equation is semi-empirical in its essence. The present paper is aimed at obtaining an analytical wide range

equation of state for metals based on the most general physical concepts giving good agreement with the experimental results in certain parametrical ranges of the substance's state.

## A FEW OF THE KNOWN EQUATIONS

In the development of the theoretical models of the electric explosion, the following can obviously be considered as the major failures: the limited number of metals for which we managed to set up the equation of state; the huge number of adjustable parameters peculiar to each of the models; the considerable number of simplifying assumptions of a specific nature; the absence of ultimate transitions from solid matter to plasma states. In such a situation, despite a number of recent reviews and reports on the achievements and problems of the theory of the equations of state [4], it seems necessary to carry out a certain analysis of the physical models of the substance (classical at present) to proceed to a more justified application of the description form of the substance state in the model of the electric explosion.

In our case, the van der Waals general conditions for the determination of the critical isotherm behavior and the supplemented requirements for the wide-range (global) equations of state [10] can serve as the basis for the analysis and derivation of a semi-empirical equation of state. Since, in the process of the electric destruction of the conductors, a few sequential phase transformations may occur, the ES applied for the description of such processes must adequately describe the solid; liquid; gaseous (plasma); and, in some cases, double-phase states.

In the early [11] and recent [12] papers too, Van der Waals's equation was used for the description of the electric explosion, which, according to [13], in coor-

dinates of $P$, $\rho$, and $T$, can be presented in the following form:

$$p = \left(1 - \frac{1}{3}x + \frac{1}{9}x^2 + \ldots + \frac{1}{3^n}x^n\right)\frac{x\tau}{Z_c} - \rho x^2. \quad (1)$$

Here $p = P/P_c$; $x = \rho/\rho_c$; $\tau = T/T_c$; and $Z_c = \mu\dfrac{P_c}{R\rho_c T_c}$ is the factor of compressibility at a critical point (the critical factor of compressibility).

It is easy to show that one of the simplest conditions [10] $\partial p/\partial x|_{\tau=\tau_0} = c^2$, where the reduced sound velocity $c_r = \sqrt{\partial p_x/\partial x}$, under normal conditions, in the given case appears not to be fulfilled ($c^2 = -6x_0$). Under the normal conditions, the reduced sound velocity for the metals is on the order of 10.

It thus becomes obvious that the Van der Waals equation of state or the modification of it should be extrapolated to the condensed phases of the metals with great care.

It should also be noted here that the critical factor of compressibility for the metals is 0.284 according to [14]. In the van der Waals ES and its other modifications, except for the Diterichi equation, $z = 0.375$.

The intention to use the simplest analytical model for the calculation of virtually all of the thermodynamic values leads in a number of cases to the application of small integer degrees in describing the elastic component of the pressure. This component of the pressure, in terms of the relative densities, can be written for the interacting particles as follows:

$$p_\tau = -\frac{\tau x}{z}; \quad p_x = a\left(x^2 + \frac{b}{a}x^3\right). \quad (2)$$

where $a = -3$ and $b = 1$. With such a ratio of the constants, the reduced sound velocity is 4, which is significantly closer to the real but less than the experimental values of the sound velocity for metals.

In review [10], an equation of the following type is presented as the most often used one:

$$p_x = a\left(x^{\frac{m}{3}+1} - bx^{\frac{n}{3}+1}\right). \quad (3)$$

According to the above review, Mie and Bohr used the equation with $n = 3$, and a whole series of works were aimed at the clarification of $m$ and $n$.

Using the form of the thermal component as an ideally gaseous one, it is easy to show (when defining the constants according to Van der Waals) that, at $n - m \le 1$, the sound velocity will always remain less than the real one. In addition, with such a form of the applied equation, it appears to be independent of the temperature.

Recently, for the electrical explosion's description, Kolgatin and Khachatur'yants' interpolation equation for the state of metals is used most often [6, 16, 17], which, after certain transformations and evaluations, can be reduced to the form

$$p_\tau = \frac{4}{9}\left(\frac{1 + 3\gamma x^k/l\tau}{1 + x^k/l\tau}\right); \quad p_x = ax^{\frac{m}{3}+1} - bx^{\frac{n}{3}+1}. \quad (4)$$

Here, $\gamma$, $a$, $b$, $l$, and $k$ are the constants determined by the metal's properties.

Considering all the above mentioned, the application of this equation for metals in a condensed state is assumed to be possible only with certain provisions, i.e., mainly for the gaseous-plasma phase. Since, for the majority of metals the degree $m = (5–6)$, we have to make do with a cubic equation at best, and the difference between the degrees $m/3 + 1$ and $n/3 + 1$ insignificantly differs from 1. In this case, as has already been said, the sound velocity will be considerably lower than the experimental value. It is evident that the sound velocity will increase monotonically upon the temperature growth up to a critical point.

An identical equation in the form of a third power polynomial was already used in [18, 19]. In [19], the equation obtains a form where all of the coefficients depend on the temperature:

$$p(x, \tau) = a(\tau)x + b(\tau)x^2 + c(\tau)x^3. \quad (5)$$

Finally, in a series of papers discussing the method for finding the efficient potential of a cell model of a condensed substance, Kesselman with colleagues [20–22] offered an equation for liquid metals where the elastic component of the pressure is represented by a function of the temperature in an explicit form:

$$p_x = -A(T)\rho^q + B(T)\rho^f. \quad (6)$$

Here, $q = 2$ and $f = 4$ are determined from the condition of the optimal description of the experimental thermal data, and $f$, with a higher degree of density, becomes closer to the Teit equation with the density degree for metals lying in the range from 3.2 to 6.3 [23] with $q$ and $f$ being necessarily integer-valued according to [20–22].

Let us now show that a somewhat different but sufficiently close equation can be derived where the density degree should not necessarily be integer valued. Moreover, the performed analysis [10] showed that, in a more general form, the elastic component of the pressure as a rule may by represented as

$$p_x \approx \sum_{i=1}^{N} a_i x^{i-1/3}.$$

Therefore, below, a gradual consideration of the main pressure items that determine the form of the equation of the state for metals will be carried out with account for the main items of interaction.

## THE MODEL OF THE EQUATION OF STATE

For the crystalline metal lattice, the energy of the Coulomb interaction and of any positive ion with all the rest of the charges that it is surrounded by can be expressed depending on the distance $d$ between the neighboring positive ions using the formulae of the same form as in the case of the ion lattice, where the ions of the opposite sign are at a distance $d/2$ from each other:

$$u = -@e^2/d, \tag{7}$$

where @ is the Madelung constant, and $e$ is the electron charge.

If an actual close to uniform distribution of the electrons between the positive ions of the metal is substituted for the concentrated distribution corresponding to the concentration of the electrons in the interstitial spaces of the positive ions, the @ coefficient may obtain a value of 3, 4.

The electric energy in a metal lattice characterizes the forces of the interparticle coupling due to the electron collectivization. The electric forces of coupling at a certain value of $d_0 = d$ must be balanced by the repulsion forces of quite a different nature. It is easy to ascertain that those are the inertia forces occurring during the motion of the collectivized electrons and, to be exact, upon modifying this motion's direction in the case of the electron reflection from the metal's surface. In other words, the pressure created by the collectivized electrons acts as the repulsion forces, as occurs in conventional gases.

The gas pressure is determined through its $V$ volume, the $N$ number of particles, and the average kinetic energy of one of them ($mv^2/2 = \varepsilon$) using the known formula of the kinetic theory of a gas:

$$PV = \frac{1}{2}Nmv^2 = \frac{2}{3}N\varepsilon.$$

Assuming here that $\varepsilon = \frac{2}{3}kT$, we derive the Clapeyron formula $PV = NkT$, which represents the equation of state of conventional gases.

In the region of the ordinary temperatures of metals, as was shown above, the pressure depends only on the volume; i.e., it is not a function of the temperature:

$$PV = (2/3)E, \tag{8}$$

where $E$ is the energy of the collectivized electrons. On the other hand, the average energy of the electron gas of the metal is determined precisely by the kinetic energy of the collectivized electrons, it is not thermal in character, and therefore is temperature independent (at least up to the values equaling units of electron-volts, i.e., up to a few dozens of thousands of degrees). Hence, it is possible to assume with fairly high authenticity that the external effect of the electrons upon an increase of the metal volume by $dV$ occurs due to their kinetic energy $PdV = -dE = \frac{2}{3}E\frac{dV}{V}$, from where, using (8), we have $\ln(V^2E^3) =$ const, i.e.,ħ

$$E = \text{const}/V^{2/3}. \tag{9}$$

This ratio represents nothing else but the adiabatic gas compression (or expansion) law. While, in the case of conventional gases, the adiabatic compression is accompanied by heating and the expansion by cooling, the gas temperature of the collectivized electrons remains constant upon the metal volume modifying. As the electron number also remains unchanged, the average kinetic energy of the separate electrons must vary upon the volume varying following the same law (9) that $E$ obeys. Since $V^{1/3}$ is proportional to the $d$ distance between the neighboring ions, we rewrite (9) as

$$\varepsilon = \chi/d^2. \tag{10}$$

On the other hand, the de Broglie wavelength $\lambda$ is correlated with the electron motion rate $mv\lambda = 2\pi\hbar$ and must approximately coincide with the $2d$ length of the electron orbit in an isolated atom. Assuming that $\lambda = 2d$, we get $mv = \pi\hbar/d$. Therefore, $mv^2/2 \approx \pi^2\hbar^2/4md^2$; hence, from the comparison with (10), we obtain $b = \beta\hbar^2\pi^2/4m$, where $\beta$ is the correction index of the order of unit, and $m$ is the electron mass.

In the general case of a polyvalent metal, the electron rate is determined not by the average distance between the neighboring atoms but by the average distance between the neighboring valence electrons, i.e., by the value of $d/Z_0^{1/3}$, where $Z_0$ is the metal valence, and then $\chi = \beta\pi^2\hbar^2Z^{2/3}/4\text{m}$.

The $W$ total metal energy is thus derived from the sum of the potential energy (7) of the $U$ Coulomb interaction and of the $E$ kinetic energy (8) of the collective electrons, whose pressure is relevant to the repulsion forces. So, one may write for the $Z_0$ valence metal

$$-U = -\frac{@Z^2e^2N}{d}$$

and

$$E = \frac{\beta\hbar^2Z^{5/3}N\pi^2}{4m}\frac{1}{d^2}. \tag{11}$$

The total metal energy is thus represented as

$$W = -\frac{C}{d} + \frac{a}{d^2} = -U + E.$$

At the same time, in the state of the dynamic equilibrium for the electron interaction forces, we have $mv^2/d = e^2/d^2$, i.e., $mv^2 = e^2/d$; hence, $2E = U$ and

$$W = -U + E = -E. \tag{12}$$

Using (9), (12) will take the form of

$$W = -\frac{\text{const}}{V^{2/3}}. \quad (13)$$

Due to (13), for the pressure resulting from the forces of the electron coupling through the positive ions, we have

$$p_x = -\frac{\partial W}{\partial V} = \frac{\text{const}}{V^{5/3}}. \quad (14)$$

In terms of the relative density, we have $p_x = -\text{const}x^{5/3}$.

Selecting the power index for the positive component of the pressure, we shall use the compressibility factor value for metals adopted by [14]. The latter condition is well fulfilled for the case when $v = 7/3$; i.e., the term of a multipole expansion with the potential interaction proportional to $1/d^7$ agrees best with the energy of the Coulomb interaction of the ion with the surrounding in a real metal crystalline lattice. Considering the above mentioned, the equation of the state will be written as

$$P = \frac{kT}{V} - \frac{g}{V^{5/3}} + \frac{q}{V^{10/2}}. \quad (15)$$

Proceeding to the dimensionless variables, in the designations adopted earlier for the equation of state, we finally have

$$p = \frac{\tau x}{z} - Gx^{5/3} + Qx^{10/3}. \quad (16)$$

The new constants $z$, $G$, and $Q$ are to be determined using the conditions at the critical point: $(\partial p/\partial x)_\tau = 0$ and $(\partial^2 p/\partial x^2)_\tau = 0$. The compressibility factor $z^{-1} = 25/7$ in this case takes the value closest to the experimental data among the values obtained on the basis of the available precise solutions of the equations of the state presented earlier. Using the above constants, the equation of the state (16) will be rewritten as follows:

$$p = z^{-1}\tau x - \frac{21}{25}z^{-1}x^{5/3} + \frac{3}{25}z^{-1}x^{10/3}$$

or

$$p = \frac{25}{7}\tau x - 3x^{5/3} + \frac{3}{7}x^{10/3}. \quad (17)$$

The same as in the equation of the state of a condensed phase of a pure substance [22], the parameters $G$ and $Q$ depend on the temperature. From the conditions $\partial p/\partial x|_{To} = c_r^2$ ($c_r$ is the reduced sound velocity under the normal conditions) and $\partial p/\partial x|_{Tc} = 0$, it is evident that this dependency decreases with an increase of the temperature.

In addition, note that these correlations are used due to the fact that the sound velocity, because of its informativeness, predominates in the agreement of the thermodynamic properties and the derivation of the equation of the state [25].

The specific dependency of the elastic component of the pressure on the temperature fit for both the liquid and the solid phases can be expressed in the form of a nonadditive contribution as an exponent [22].

For the attractive interaction,

$$f_1(T) = \exp[c_1(1-\tau)]. \quad (18)$$

For the repulsive forces,

$$f_2(T) = \exp[c_2(1-\tau)]. \quad (19)$$

Then, the elastic component in the equation will take the following form:

$$p_x = -Ax^{5/3}e^{c_1(1-\tau)} + Bx^{10/3}e^{c_2(1-\tau)}, \quad (20)$$

where $A = Gf_1(\tau)^{-1}$ and $B = Qf_2(\tau)^{-1}$.

Solving the equation system $p_x = 0$ at $\tau = \tau_0$, $x = x_0$; $\partial p_x/\partial x = c_r^2$ at $\tau = \tau_0$, $x = x_0$, we obtain the values of the $c_1$ and $c_2$ constants:

$$c_1 = \frac{1}{1-\tau_0} - \ln\frac{3}{5}\frac{c_r^2}{Ax_0^{2/3}},$$
$$c_2 = \frac{1}{1-\tau_0} - \ln\frac{3}{5}\frac{c_r^2}{Bx_0^{7/9}}. \quad (21)$$

Considering that $c_r$ has a small spread for the majority of metals, one can instantly evaluate the values of the $c_1$ and $c_2$ constants. The numerical values of these constants differ insignificantly from each other and from the values obtained using the other method in [22] only for one common constant.

Since the sound velocity is the most accurately measurable acoustic property, then, using its values from the vast range of temperatures and pressures, makes it possible to create a fairly authentic thermodynamic $P$–$V$–$T$ surface. In addition, on the contrary, comparing the calculated sound velocity using the equation of the state for various temperatures with the experimental values for the same temperatures, one can infer the adequacy of the selected model compared to the real equation of state.

The values of the sound velocity thus calculated from the equation of the state (20) for the liquid metals of Ag, Cd, and Pb in the melting temperature proximity differ not more than by 5–7% from the experimental values. The comparison was performed with the data from Kikoin's handbook [26].

## CONCLUSIONS

The equation of state thus obtained contains not a single adjustable constant. All the constants are expressed through the critical parameters of the metals along with the sound velocity under normal condi-

tions. Naturally, the accuracy of the calculations performed using the reduced equation depends on the accuracy of the determination of the pressure, the temperature, and the density at the critical point. The parametric evaluations at the critical point based on the law of the corresponding states [14] were carried out provided that the critical factor of the compressibility for the big group of metals was a universal constant equaling 0.284. Relying upon this state, the equation obtained fits for more than fifty metals whose critical parameters were calculated in [14]. Note that such an equation seems improper to use for the biphasic liquid–gas region, because using a certain common value of the density in this part of the phase diagram appears pointless, and a similar characterization has nothing to do with the real systems and cannot serve as a parameter to characterize the phase transition region [27].

## REFERENCES


1. Martynyuk, M.M., Paremeters of the Critical Point of Metals, *Zh. Tekh. Fiz.*, 1983, vol. 57, no. 4, pp. 810–821.
2. Ivanov, V.V., Lebedev, S.V., and Savvatimskii, A.I., Peculiarities of Electroresistance of Liquid Tungsten under Conditions of a Limited Volume and upon Free Expansion, *Teplofiz. Vys. Temp.*, 1982, vol. 20, no. 6, pp. 1093–1097.
3. Kolgatin, S.N., Lev, M.L., Peregud, B.P., et al., Destruction of Copper Conductors due to the Current Flow in Them of the Density of above $10^7$ A/cm$^2$, *Zh. Tekh. Fiz.*, 1989, vol. 59, pp. 123–133.
4. Siminenko, V.A. and Sin'ko, G.V., Achievements and Problems of a Theory of Equations of State, *Teplofiz. Vys. Temp.*, 1988, vol. 26, no. 5, pp. 864–873.
5. Kalitkin, N.N., Quasizonal Equation of State, *Mat. Model.*, 1989, vol. 1, no. 2, pp. 64–106.
6. Kolgatin, S.N. and Khachatur'yants, A.V., Interpolation Equations of State of Metals, *Teplofiz. Vys. Temp.*, 1982, vol. 20, pp. 447–451.
7. Bushman, A.V., Kanel', G.I., Ni, A.L., and Fortov, V.E., *Teplofizika i dinamika intensivnykh impul'snykh vozdeistvii* (Thermal Physics and Dynamics of the Intense Pulse Effects), Chernogolovka: Inst. Khim. Fiz. AN SSSR 1988, p. 325.
8. Gryaznov, V.K., Iosilevskii, I.L., Krasnikov, Yu.G., et al., *Teplofizicheskie svoistva rabochikh sred gazofaznogo yadernogo reaktora* (Thermophysical Properties of Operating Media of the Gas-Phase Nuclear Reactor), Moscow: Atomizdat, 1980, p. 303.
9. Krivitskii, E.V., Shamko, V.V., and Khainatskii, S.A., Thermal Equation of State of Metals for the Dynamic Problems of the Conductor Destruction Modeling upon the Electroexplosion, *Elektron. Obrab. Mater.*, 2002, no. 5, pp. 28–31.
10. Kuropatenko, V.F., The Equation of State in the Mathematical Models of Mechanics and Physics, *Mat. Model.*, 1993, no. 12, pp. 48–61.
11. Bennet, F., *Volna ispareniya* (Evaporation Wave), Kal'dirola, P. and Knopfel', G., Eds., Moscow: Mir, 1974, pp. 241–257.
12. Vorob'ev, V.S. and Malyshenko, S.P., Phase Equilibrium in a Liquid Conductor with Current in Z-Pinch Geometry, *Zh. Tekh. Fiz.*, 1997, vol. 111, no. 6, pp. 2016–2029.
13. Anisimov, M.A., Rabinovich, V.A., and Sychev, V.V., *Termodinamika kineticheskogo sostoyaniya ideal'nykh veshchestv* (Theromodynamics of a Kinetic State of Ideal Substances), Moscow: Energoatomizdat, 1990.
14. Fortov, V.E., Dremin, A.N., and Leont'ev, A.A., Estimation of Parameters of the Critical Point, *Teplofiz. Vys. Temp.*, 1975, vol. 13, no. 5, pp. 1072–1080.
15. Senkevich, A.A., Parameters of the Critical State and Their Correlation with the Effective Potential of the Interaction Forces, *Otchet Ped. Inst. Krupskoi,* Moscow: 1987.
16. Kolgatin, S.N. and Shneerson, G.A., Peculiarities of Plasma Heating upon the Electric Explosion of the Conductors in a Super Strong Magnetic Field, *Pis'ma Zh. Tekh. Fiz.*, 1994, vol. 20, no. 5, pp. 67–71.
17. Kolgatin, S.N. and Shneerson, G.A., On Plasma Heating by the Induced Azimuthal Current upon the Electric Explosion of the Conductors in a Super Strong Magnetic Field, *Zh. Tekh. Fiz.* 1997, vol. 67, no. 1, pp. 46–50.
18. Romanov, G.S. and Smetannikov, A.S., Numerical Modelling of the Layered Pulse Discharge, *Zh. Tech. Fiz.*, 1981, vol. 51, no. 4, pp. 678–686.
19. Dresvyannikov, V.I. and Trenin, V.V., *Prikladnye problemy prochnosti: Analis i optimizatsiya konstruktsii* (Application Problems of Strength: the Analysis and Optimization of a Construction), Gor'kii:1989, pp. 61–68.
20. Kessel'man, P.M. and Onufriev, I.V., A Method of the Effective Potential in a Cell Model of Liquid. Application to the Binary Liquid Systems, *Inzh. Fiz. Zh.*, 1979, vol. 37, no. 2, pp. 316–323.
21. Kessel'man, P.M., Modification of a Cell Model and Equation of State of Liquid, *Inzh. Fyz. Zh.*, 1988, vol. 50, no. 1, pp. 65–72.
22. Kessel'man, P.M., Inshakov, S.A., and Bykov, A.Yu., The Equation of State of a Solid Body, *Teplofiz. Vys. Temp.*, 1996, vol. 34, no. 3, pp. 392–396.
23. Fizika vzryva (Physics of Explosion), Stanyukovich, K.P., Ed., Moscow: Nauka, 1975.
24. Frenkel', Ya. I., *Vvedenie v teoriyu metallov* (Introduction to Theory of Metalls), Moscow–Leningrad: GITTL, 1950.
25. Bystrov, P.I., Kagan, D.M., Krechetova, G.A., and Shil'rain, E.E., *Zhidkiometallicheskie teplonositeli teplovykh trub i energeticheskikh ustanovok* (Liquid Metal Heat Carriers of Heat Pipes and Power Stations), Moscow: Nauka, 1988.
26. *Tablitsy fizicheskikh velichin* (Tables of Physical Values), Kikoin, I.K., Ed., Moscow: Atomizdat, 1976.
27. Bazarov, I.P. and Nikolaev, P.N., Derivation of the Equation of State of the Homogenous Systems, *Zh. Fiz. Khim.*, 1987, vol. 61, no. 3, pp. 807–809.

ISSN 1068-3755, Surface Engineering and Applied Electrochemistry, 2010, Vol. 46, No. 3, pp. 235–236. © Allerton Press, Inc., 2010.
Original Russian Text © I.I. Beril, M.K. Bologa, 2010, published in Elektronnaya Obrabotka Materialov, 2010, No. 3, pp. 43–44.

## ELECTRICAL PROCESSES IN ENGINEERING AND CHEMISTRY

# Temperature Dependence of the Electric Conductivity of Low Conducting Organic Liquids

**I. I. Beril and M. K. Bologa**

*Institute of Applied Physics, Academy of Sciences of Moldova, ul. Akademiei 5, Chisinau, MD 2028 Republic of Moldova*
*e-mail: mbologa@phys.asm.md*

Received August 25, 2009

**Abstract**—The relationships for refined sunflower oil and transformer oil are presented. It is substantiated that the electric conductivity of the low conducting organic liquids is of a semiconductor type.

**DOI:** 10.3103/S1068375510030075

Previously, there were derived the relations for the concentration of phosphatides in the refined sunflower oil [1] and for the resistivity of the transformer oil [2]. On the basis of this, the specific electric conductivity of the sunflower oil is

$$\sigma_1 = 1.44 \times 10^{-9}(\varphi - 0.123)(T - 281.291), \quad (1)$$

while that of the transformer oil is

$$\sigma_2 = \frac{1.61 \times 10^2}{\rho_0} e^{+\alpha(T - T_0)}, \quad (2)$$

where $\varphi = 0.1452$ is the lowest concentration of phosphatides, $T$ is the absolute temperature, $\rho$ is the resistivity at $T = 293$ K, and $\alpha = 0.04–0.05$ l/grad is the temperature coefficient. Formulas (10) and (2) are valid at temperatures of 20°C ≤ $t$ ≤ 70°C. The low reproducibility of the data of the previous experimental research should be noted, as the microscopic parameters of the liquids were not controlled, which is very important in every particular experiment. Thus, the development of theoretical works in this sphere is preferred.

Under the condition that the energy of activation of the impurity centers $\Delta E$ is much greater than the heat energy $3/2kT$, where

$$\Delta E \gg 3/2kT, \quad (3)$$

from relations (1) and (2), for $\ln\sigma$, there are derived the linear dependences on the reciprocal temperature:

$$\ln\sigma = a\frac{1}{T} + b, \quad (4)$$

where $a$ and $b$ are the coefficients determined from (1) and (2) in every case after transformation to form (4).

Condition (3) is nearly always fulfilled. For instance, the impurity centers of the 1st and 7th groups of the periodic system with the activation energies 1.36, 0.87, 0.56, and 0.66 eV are introduced into the refined sunflower oil[1]: $3/2kT \approx 0.04$ eV; that is, condition (3) is well fulfilled.

From (1) and (2), it is simple to derive relation (4) and, after construction of the diagrams, to calculate

$$\ln\sigma_1 = -3.5 \times 10^3 \frac{1}{T} - 19.8, \quad (5)$$

$$\ln\sigma_2 = -4.58 \times 10^3 \frac{1}{T} - 17.7. \quad (6)$$

The dependences of the electric conductivity logarithm on the reciprocal temperature for the refined sunflower oil (Fig. 1) and the transformer oil (of [TeKai] type) (Fig. 2) are presented in Figs. 1 and 2. For the transformer oil, there are plotted the experimental points obtained in [2] in the experiments at 20°C. At $\alpha = 0.04$ and 0.05 (considering that, at $t$ = 20°C, four experimental points were obtained for the other temperatures), the electric conductivity is taken on the basis of the approximation for the resistivity [2] with $\sigma = \varepsilon_0/\rho V C_0$, where $\rho$ is the resistivity, and $V$ and $C_0$ are the volume of the interelectrode gap and its capacity.

It can be similarly shown that the electric conductivity of all the known refined low conducting organic liquids is of the semiconductor type.

In works [3–5], there is given the relation for the electrolytic liquids, which is well fulfilled for the aqueous and other electrolytes:

$$1/E = -\frac{x - x_0}{\varphi_0} \approx \frac{\Delta x}{\Delta\varphi}; \quad \varphi_0 = \frac{kT}{ez}, \quad (7)$$

where $x$, $x_0$, $\varphi_0$, $k$, $T$, $e$, and $z$ are the current, the initial coordinates, the characteristic potential, Boltzmann's constant, the absolute temperature, the electron

[1] The impurity centers are introduced into the oil artificially to produce extrinsic donor and acceptor semiconductors.

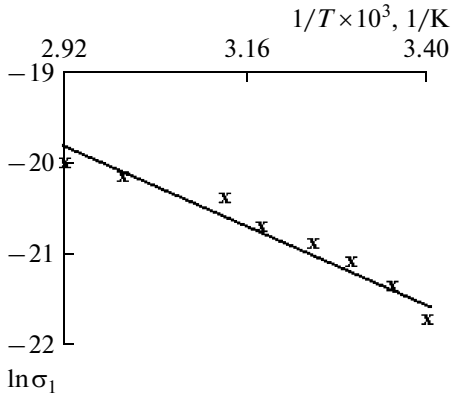


**Fig. 1.** The sunflower oil's electric conductivity logarithm versus the reciprocal temperature characteristics.

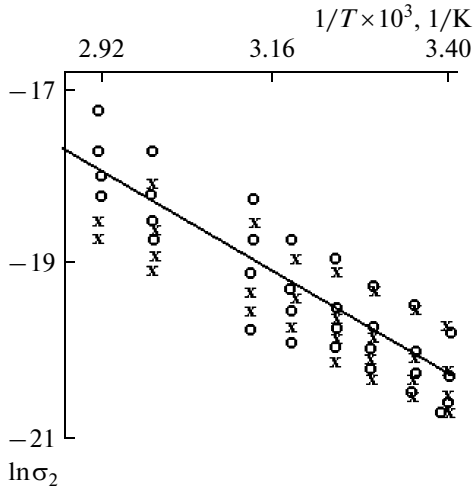


**Fig. 2.** The transformer oil's electric conductivity logarithm versus the reciprocal temperature characteristics. $\alpha = 0.04$ (x); $\alpha = 0.05$ (o).

charge, and the valency of the examined ion, respectively. For the refined transformer oil, $z = -10^{-5}$, and $\varphi_0$ ranges up to 2.58 kV. The conclusion is reached that the transformer oil is grouped with electrolytes, but this is untrue, as the valency loses its meaning by definition. The change of the definitions of the characteristics not only leads to confusion but also causes the deviation from the adequacy achieved before on the basis of the fundamental laws.

As the refined low conducting organic liquids are classed with semiconductor materials, the problems concerning producing *p* and *n* high-voltage semiconductors on their basis becomes rather important, as such substances can be used in practical electronics.

## REFERENCES

1. Bologa, M.K and Beril, I.I., *Rafinatsiya podsolnechnogo masla v electricheskom pole*, (Sunflower Oil Refinement in Electric Field), Kishinev: Shtiintsa, 2004.
2. Beletskii, Z.M., Ryzhenko, V.I., and Topolyanskii, E.L., The Dependence of the Transformer Oil Conductivity on the Electric Field Intensity and Temperature, *Elektrotekhnika*, 1974, no. 4, pp. 46–48.
3. Ostroumov, G.A. and Petrichenko, N.A., Insulating Fluids as the Ion Conductors of Electricity, *Elektron. Obrab. Mater.*, 1974, no. 1, pp. 40–44.
4. Ostroumov, G.A. and Stishkov, Yu.K., *Electron. Obrab. Mater.*, 1970, no. 1, pp. 36–39.
5. Samodin, V.M. and Stishkov, Yu.K., *Electron. Obrab. Mater.*,1971, no. 3, pp. 44–46.

ISSN 1068-3755, Surface Engineering and Applied Electrochemistry, 2010, Vol. 46, No. 3, pp. 237–242. © Allerton Press, Inc., 2010.
Original Russian Text © A.P. Smirnov, V.M. Kosenkov, V.G. Zhekul, S.G. Poklonov, 2010, published in Elektronnaya Obrabotka Materialov, 2010, No. 3, pp. 45–52.

## ELECTRICAL PROCESSES IN ENGINEERING AND CHEMISTRY

# The Study of the Effect of the Electrodischarge Action Modes on Viscous Deposits in Cylindrical Channels

**A. P. Smirnov, V. M. Kosenkov, V. G. Zhekul, and S. G. Poklonov**

*Institute of Pulse Processes and Technologies, National Academy of Sciences of Ukraine*
*pr. Oktyabrskii 43a, Nikolaev, 54018 Ukraine*

*e-mail: iipt@iipt.com.ua*

Received January 11, 2010

**Abstract**—The study of the effect of the electrodischarge device parameters on the behavior of viscous deposits in the perforation channel of the well bottom hole zone has been carried out applying mathematical simulation. There are suggested some recommendations on improving the decolmatage electrodischarge method.

**DOI:** 10.3103/S1068375510030087

## INTRODUCTION

With an oil well being in service, there happens the colmatage of the bottom hole zone (BHZ) with various deposits (viscous or brittle ones) reducing its yield. Different decolmatage methods based on the chemical, physical, or combined physical–chemical action on the colmatant are used to rejuvenate the well's yield [1]. The electrodischarge (electrohydroimpulsive) decolmatage procedure elaborated in the IPPT of the National Academy of Sciences of Ukraine is one of the most promising physical action modes [2].

The aim of the previous research of the decolmatage electrodischarge method [3, 4] was to study the hydrodynamic processes in the well, to examine the behavior of the matrix of a porous medium saturated with a liquid at the impulsive loading by an electric discharge and to investigate the electrodischarge action on brittle deposits with the behavior of the viscous deposits not being considered.

The analysis of the behavior of a viscous colmatant contaminating a well BHZ bay is possible at electrodischarge action with the help of a mathematical or physical simulation. The physical simulation of the processes in the well calls for great time and material expenditures, so it would be appropriate to apply a mathematical simulation.

Thus, the purpose of this work is the mathematical simulation of the viscous deposit's behavior at an electrodischarge (electrohydroimpulsive) action and the study of the influence of the different electrodischarge device parameters on the proficiency of its effect on the viscous deposits.

## THE MATHEMATICAL MODEL OF THE PROCESS

The mathematical model of the electrodischarge action on viscous deposits in BHZ slits (or perforations) has a block structure and consists of three blocks. The first block of the model describes the processes in the discharge channel, the second one describes the processes in the borehole fluid, and the third one deals with the processes in the viscous fluid in the well's BHZ bay with the output data of one block being the initial data for the next block.

In constructing the mathematical model of the above mentioned processes, the following assumptions were made:

—at the initial moment of time, the discharge channel has the shape of a straight ring cylinder with its height being equal to the interelectrode gap length and the symmetry axis coinciding with the symmetry axis of the well and the submersible section of the complex;

—the well is filled with a perfect liquid;

—the well wall is absolutely rigid and fixed;

—a plane compression wave falls on the well wall;

—the perforation walls are impenetrable and fixed;

—the perforation is filled with the borehole fluid and viscous deposits.

The first block equations (1)–(4) corresponding to the model presented in [5] describe the processes in the charging circuit and in the discharge channel:

$$L\frac{dI}{dt} + I(R_{\text{chan}} + R_{\text{bus}}) + q_z/C = U_n, \qquad (1)$$

where $I = dq_z/dt$,

$$\frac{d(p_{chan}S_{chan})}{dt}\frac{1}{\gamma-1} + p_{chan}\frac{dS_{chan}}{dt} = I^2 R_{chan}\frac{1}{l}, \quad (2)$$

$$p_{chan} = \frac{\rho_0}{2\pi}\frac{d^2 S_{chan}}{dt^2}\ln\left(\frac{\pi^{0.5} l}{S_{chan}^{0.5}}\right) - \frac{\rho_0}{8\pi S_{chan}}\left(\frac{dS_{chan}}{dt}\right)^2, \quad (3)$$

$$R_{chan} = \frac{Al(\gamma-1)}{p_{chan}S_{chan}}. \quad (4)$$

In relations (1)–(4), $I$ is the discharge current, A; $L$ is the electric circuit inductance, H; $C$ is the capacity of the bank of capacitors, F; $U_n$ is the initial voltage at the moment of the discharge chammel's generation, V; $R_{chan}$ is the discharge channel resistance, Ohm; $R_{bus}$ is the resistance of the discharge circuit buses, Ohm; $q_z$ is the electric charge, C; $l$ is the discharge channel length, m; $p_{chan}$ is the pressure in the channel, Pa; $S_{chan}$ is the area of the discharge channel cross section, $m^2$; $\gamma$ is the Poisson effective adiabatic exponent; $\rho_0$ is the density of the rest fluid, $kg/m^3$; $A$ is the spark constant, $V^2\,s\,m^{-2}$; and $t$ is the time, s.

To describe the hydrodynamic processes in the well (the second block of the mathematical model) in view of all assumptions and the well sizes, there is used a one-dimensional wave equation (5) [6]:

$$\frac{\partial^2\varphi}{\partial r^2} + \frac{1}{r}\frac{\partial\varphi}{\partial r} = \frac{1}{c_w^2}\frac{\partial^2\varphi}{\partial t^2}, \quad (5)$$

where $\varphi$ is the potential of the liquid motion velocities, $m^2/s$; $r$ is the space coordinate, m; and $c_w$ is the sonic speed in the borehole fluid, m/s.

The set of equations (6)–(9) consisting of the continuity equation (6) and the viscous liquid motion equations (7), (8) [7] is used to describe the behavior of the viscous deposits (the third block of the mathematical model). This set of equations is closed by the liquid state equation in the form of Tetta (9) [8]:

$$\frac{\partial\rho}{\partial t} + \mathrm{div}(\rho V) = 0, \quad (6)$$

where $\mathrm{div}(\rho V) = \frac{1}{r}\frac{\partial r\rho V_r}{\partial r} + \frac{\partial\rho V_z}{\partial z}$; $\rho$ is the fluid density, $kg/m^3$; and $r$, $z$ are the space coordinates, m.

$$\frac{\partial V_r}{\partial t} + V_r\frac{\partial V_r}{\partial r} + V_z\frac{\partial V_r}{\partial z} = -\frac{1}{\rho}\frac{\partial P}{\partial r} + \nu\left(\frac{\partial^2 V_r}{\partial r^2} + \frac{1}{r}\frac{\partial V_r}{\partial r} + \frac{\partial^2 V_r}{\partial z^2} - \frac{V_r}{r^2}\right), \quad (7)$$

where $\nu$ is the kinematic viscosity coefficient, $m^2/s$; and $P$ is the pressure in the liquid, Pa.

$$\frac{\partial V_z}{\partial t} + V_r\frac{\partial V_z}{\partial r} + V_z\frac{\partial V_z}{\partial z} = -\frac{1}{\rho}\frac{\partial P}{\partial r} + \nu\left(\frac{\partial^2 V_z}{\partial r^2} + \frac{1}{r}\frac{\partial V_z}{\partial r} + \frac{\partial^2 V_z}{\partial z^2}\right), \quad (8)$$

$$P = B_s\left(\left(\frac{\rho}{\rho_0}\right)^{k_s} - 1\right) + P_0, \quad (9)$$

where $\rho_0$ is the density of the nondisturbed liquid, $kg/m^3$; $P_0$ is the pressure of the nondisturbed liquid, Pa; and $B_s$, $k_s$ are the parameters characterizing the liquid medium.

At the borehole fluid–viscous deposit contact interface, there is laid down the condition of the equality of the tangential stresses on the side of the viscous deposit interface and the borehole fluid–interface (10). This condition allows one to study to high accuracy the processes at the boundary surface of the two media:

$$\tau_{media} = \tau_{b.f.}, \quad (10)$$

where $\tau_{media}$ is the tangential stress in the viscous deposit at the boundary surface of the viscous media, Pa; and $\tau_{b.f.}$ is the tangential stress in the borehole fluid at the boundary surface of the viscous media, Pa.

The tangential stresses are determined with the expression [9]

$$\tau_{xy} = \mu\frac{\partial V_r}{\partial y}, \quad (11)$$

where $\mu$ is the dynamic coefficient of the viscosity, Pa s; and $\tau_{xy}$ are the tangential stresses, Pa.

The upper and the lower boundaries and the boundary opposite to the inlet one are assumed to be absolutely rigid, and there are laid down the conditions of nonleakage and adhesion:

$$V_n = 0, \quad V_\tau = 0, \quad (12)$$

where $V_n$ is the normal component of the liquid velocity, m/s; and $V_\tau$ is the tangential component of the liquid velocity, m/s.

The set of equations (1)–(4) describing the processes in the discharge channel and in the charging circuit has been solved by the Euler–Cauchy finite difference method [10]. Wave equation (5) has been solved with the help of the cross pattern [11]. The three-step finite difference method [12] has been used to solve the set of equations (6)–(9) describing the hydrodynamic processes in the viscous fluid. Two steps are performed with the Euler–Cauchy method. The regularization procedure for the solution of equations (6)–(9) has

been carried out using the method of Abarbanel and Zwas to remove the nonphysical oscillations.

The computation was performed with the help of a program written in the algorithmic language Borland Delphi 7.0.

## INVESTIGATION OF THE MODES OF ELECTRODISCHARGE ACTION ON VISCOUS DEPOSITS

Previously, there was carried out the testing of this mathematical model and the numerical method of Euler–Cauchy–Abarbanel and Zwas [12], and the conclusion was reached that it can be used to study the effect of different process parameters of the electrodischarge working of the well on the behavior of the viscous deposits in cylindrical channels.

When examining the influence of the modes of the electrodischarge action on the behavior of the viscous deposits in the BHZ perforation holes, there are taken as the initial data of the charging circuit the parameters corresponding to the parameters of the electrodischarge downhole device of the "EsKaIEf" type [13]:

—the charging voltage $U_0 = 30$ kV;

—the discharge circuit inductance $L = 0.7$ μH;

—the capacity of the capacitor bank $C = 2.1$ μF;

—the resistance of the discharge circuit elements without regard for the discharge channel is $R_{kn} = 0.6$ Ohm;

—the interelectrode gap length is $l = 0.02$ m.

The diagram of the BHZ perforation channel is presented in Fig. 1. The channel is filled with two liquid media with different viscosities. A uniform layer of viscous deposits ($D_2$ and $D_3$) with the viscosity $\mu_1$ is on the hole walls, and there is a borehole fluid layer with the viscosity $\mu_2$ between them; at that, $D_1 = D_2 + D_3$ and $D_2 = D_3$. It is also taken that $\mu_1\ \mu_1 \ll \mu_2$. Water ($\mu_1 = 0.00105$ Pa s) was chosen as the first model liquid, and a viscous medium with $\mu_2 = 80$ Pa s was chosen as the second one.

The time profiles of the discharge current and voltage (Fig. 2), as well as of the pressure in the discharge channel (Fig. 3, curve *1*), were obtained as a result of the performed calculations of the first block of the mathematical model. The results of the computation of the second block of the mathematical model are presented in the form of a diagram of the pressure on the well's walls (Fig. 3, curve *2*).

To determine the way of the electrodischarge action on the viscous deposits, there were fulfilled calculations for a cylindrical perforation channel 0.3 m in length and with a diameter of 0.012 m at the hydrostatic pressure $P_{hydrostatic} = 0.1$ MPa typical for water-supply wells.

The analysis of the obtained data shows that, under the action of the compression wave, the layer of viscous deposits and the borehole fluid start to move with

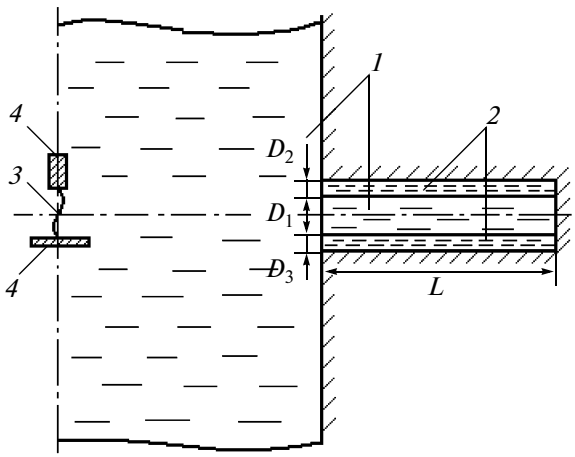


**Fig. 1.** The diagram of the cylindrical perforation channel: (*1*) the borehole fluid; (*2*) the viscous deposits; (*3*) the discharge channel; (*4*) the electrodes; $L_p$—the pore length, m; $D_1$—the cylindrical layer of the borehole fluid, m; $D_2$, $D_3$—the cylindrical layer of the viscous deposits, m.

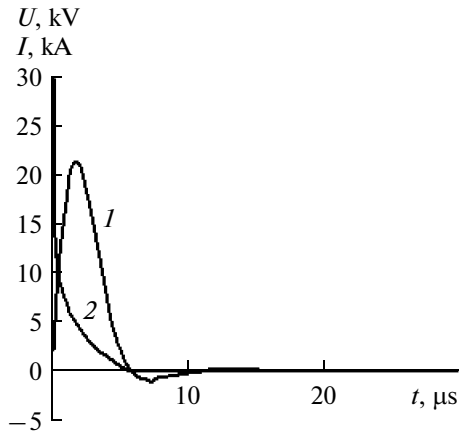


**Fig. 2.** Theoretical values of the current and voltage: (*1*) the theoretical current profile; (*2*) the theoretical voltage profile.

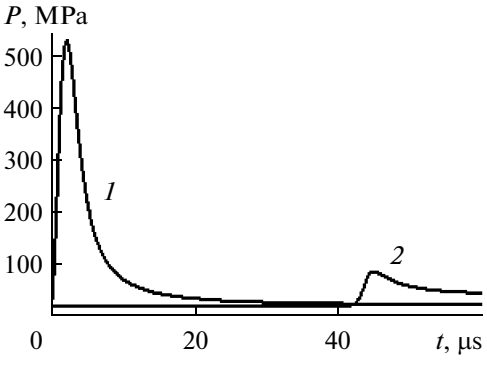


**Fig. 3.** The theoretical pressure profiles ($U_0 = 30$ kV; $L = 0.7$ μH; $C = 2.1$ μF); (*1*) the pressure in the discharge channel; (*2*) the initial compression wave on the well wall within 0.0635 m of the channel discharge.

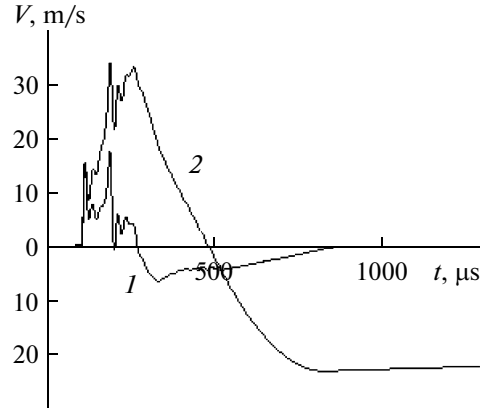


**Fig. 4.** The liquid motion velocity at $P_{hydrostatic} = 0.1$ MPa within 0.05 m of the input boundary of the perforation channel: (*1*) the viscous layer motion velocity; (*2*) the water motion velocity.

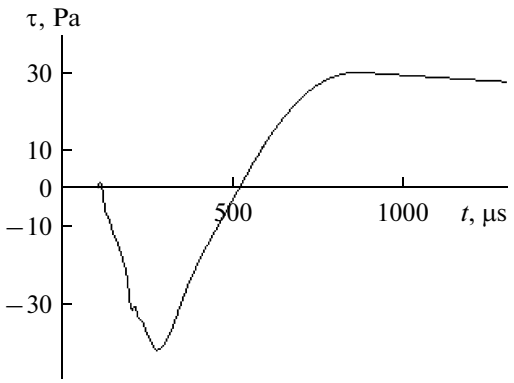


**Fig. 5.** The tangential stresses arising at the liquid–viscous deposits boundary surface within 0.05 m of the input boundary of the perforation channel at $P_{hydrostatic}$ = 0.1 MPa.

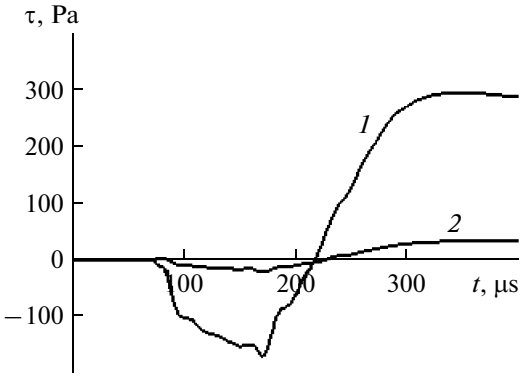


**Fig. 6.** The tangential stresses at the borehole fluid–viscous deposits boundary surface within 0.05 m of the input boundary of the perforation channel at $P_{hydrostatic}$ = 20 MPa: (*1*) the borehole fluid with $\mu_1 = 0.00872$; (*2*) the borehole fluid with $\mu_1 = 0.00105$.

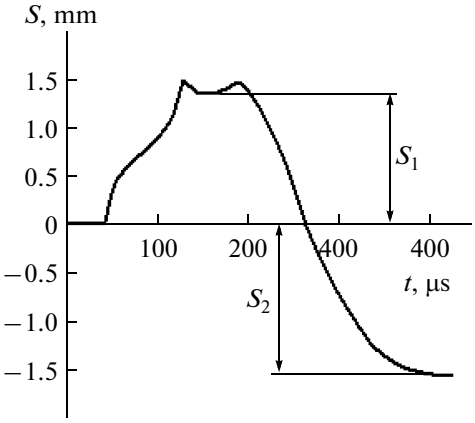


**Fig. 7.** The displacement of the point of the layer of the viscous deposits at the input boundary of the perforation channel at $P_{hydrostatic} = 20$ MPa.

a certain velocity (Fig. 4). The motion of the viscous layer continues during the action of the direct and reflected compression waves; then, there happens the rapid attenuation of the hydrodynamic processes in the viscous layer and then it comes to a stop. The water continues moving longer. The tangential stresses arising at the water–viscous deposits boundary surface due to the water motion are considerably less than the limiting shearing stresses for the viscous material (Fig. 5), lying, for instance, for solid oil, in the range of 300 to 800 Pa [14]; thus, this process doesn't participate in the breakage of the layer of the viscous contaminants.

The subsequent calculations performed at $P_{hydrostatic}$ = 20 MPa (typical for oil wells) for a cylindrical perforation channel 0.1 m in length and with a diameter of 0.012 m show that the hydrostatic pressure doesn't exert a substantial effect on the qualitative picture of the process (see Figs. 6 and 7).

In Fig. 6, there are presented the calculation results for two variants of the oil well filling up: 1—it is filled up with low-viscous oil with $\mu_1 = 0.00872$ Pa s; 2—it is filled up with water with $\mu_1 = 0.00105$ Pa s. The analysis of this figure shows that, when the well is filled with the low-viscous oil, there appear tangential stresses at the boundary surface of the media, the quantity of which is at the point of the critical shift stress for the viscous substance. Consequently, in this case, there are possible the deformation and the breakage of the upper layer of the deposits caused by the motion of the borehole fluid.

In studying the influence of the electrodischarge device's operating parameters on the behavior of the viscous deposits in the perforation channel, there was chosen the finite displacement of the point at the outer boundary of the viscous deposits (the quantities $S_1$ and $S_2$, see in Fig. 7) to estimate the efficiency of the action. This choice is due to the fact that the displace-

The effect of the electrodischarge device's operating modes on the viscous deposits

| Mode number | $U_0$, kV | $U_n$, kV | $R_{kh}$, Ohm | $L$, μH | $C$, μF | $l$, m | $W$, J | $S_1$, mm | $S_2$, mm |
|---|---|---|---|---|---|---|---|---|---|
| 1 | 30 | 28.5 | 0.6 | 0.7 | 2.1 | 0.02 | 850.5 | 1.138 | 1.273 |
| 2 | 30 | 28.5 | 0.6 | 0.7 | 4 | 0.0217 | 1620.0 | 1.378 | 1.53 |
| 3 | 25 | 23.7 | 0.6 | 0.7 | 2.1 | 0.0183 | 590.6 | 1.006 | 1.127 |
| 4 | 35 | 33.2 | 0.6 | 0.7 | 2.1 | 0.0216 | 1157.3 | 1.257 | 1.404 |
| 5 | 10 | 9.5 | 0.6 | 0.7 | 18.9 | 0.0152 | 850.5 | 1.005 | 1.121 |
| 6 | 35 | 33.2 | 0.6 | 0.7 | 1.543 | 0.0208 | 850.5 | 1.142 | 1.28 |
| 7 | 30 | 28.5 | 0.6 | 3.5 | 2.1 | 0.0245 | 850.5 | 1.089 | 1.212 |
| 8 | 30 | 28.5 | 0.15 | 0.7 | 2.1 | 0.02 | 850.5 | 1.446 | 1.612 |
| 9 | 41.425 | 39.3 | 0.6 | 0.7 | 2.1 | 0.0235 | 1620.0 | 1.402 | 1.562 |

ment incorporates both the forces caused by the compression wave and the processes hindering the motion (the friction force and the originated tangential stresses).

In the calculations, it is taken into account that the losses of the energy stored in the capacitor bank for the breakdown are 10%. The optimum interelectrode gap length has been selected for all the operating modes [15]. Water with $\mu_1 = 0.00105$ Pa s (and the parameters characterizing the medium $B_s = 304.6 \times 10^6$ and $k_s = 7.15$) is taken as the first model liquid. A liquid with the viscosity equal to the solid oil viscosity under standard conditions $\mu_2 = 80$ Pa s is the model of the viscous deposits. The parameter $k_s = 11.015$ is taken according to [16] for the high-viscosity oil, and the parameter $B_s = 131 \times 10^6$ is determined by the expressions presented in [16].

The initial data and the results of the investigation of the effect of the electrodischarge device's operating parameters on the viscous deposits are presented in the table.

The following notations are taken in the table: $U_n$ is the initial voltage at the moment of the discharge channel's generation, kV; and $W$ is the discharge energy, J.

The parameters of the operating practices presented in the table are chosen to retrace their effect on the efficiency of the action on the viscous deposits, as determined by the value of the displacement relative the solid walls of the perforation hole. It is seen from the table data and Fig. 8 that the efficiency of the action is mainly determined by the discharge energy. Thus, the twofold growth of the energy thanks to both the capacity of the installation's storage capacitor and the charging voltage results in the nearly equal (up to 25%) increase of the displacement of the viscous medium of the deposits (mode nos. 1, 2, 3, 4, and 9).

A fourfold decrease of the discharge circuit's resistance (mode no. 8) causing the increase of the displacement of the viscous deposits by 27% indirectly proves the action of the energy introduced into the spark discharge channel as it is attended by the reduction of heat losses in the discharge circuit and by the rise of the energy released in the discharge spark channel.

The latter is attended by the growth of the coefficient of the efficiency of the conversion of the stored electrical energy into the energy of the discharge acoustic wave.

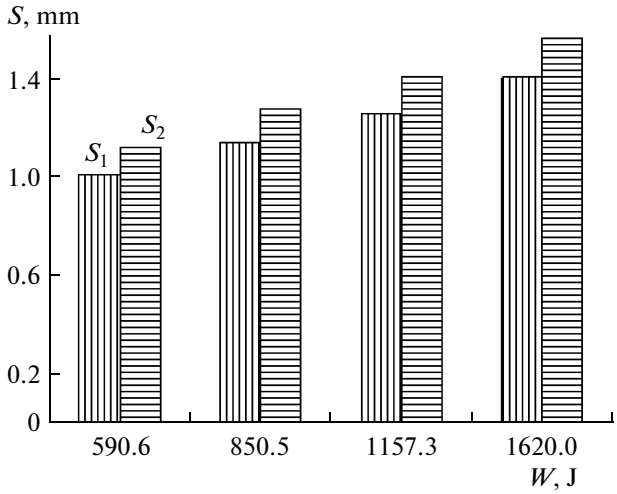


**Fig. 8.** Dependence of the viscous layer displacement on the discharge energy.

## CONCLUSIONS

The analysis of the results presented in this work allows determining the character of the behavior of viscous deposits in well perforation holes at the pulse electrodischarge action, as well as the effect of the working process's parameters on the cleanout efficiency. The following conclusions were reached:

—the pulse electrodischarge action causes the displacement of the layer of viscous deposits relative to the well perforation hole causing its cleanout in the course of the recurrent loading (repetition of the discharges);

—in the course of the pulse electrodischarge loading, there occur tangential stresses in the layer of the viscous deposits bordering the borehole fluid, and, in the case of the excess of the limiting shearing stresses for such viscous deposits, they can become the cause of their breakage;

—the efficiency of the electrodischarge action on the viscous deposits depends mainly on the discharge energy and the coefficient of the efficiency of the energy conversion into the compression wave energy.

## REFERENCES


1. Bashkatov, D.N., Drakhlis, S.L., Safonov, V.V., and Kvashnin, G.P. *Spetsial'nye raboty pri burenii i oborudovanii skvazhin na vodu*, (Special Works at Sinking and Fitting of Water–Supply Wells), Moscow: Nedra, 1988.
2. Gulyi, G.A., *Osnovy razryadnoimpul'snykh tekhnologii*, (Elements of Discharge Impulse Technologies), Kiev: Naukova Dumka, 1990.
3. Kosenkov, V.M., Kurashko, Yu.I., and Shvets, I.S., Influence of Parameters of Electrical Discharge Action on Dynamic and Seepage Processes of Near–Filter Zone of Water–Supply Wells, *Geotech. Mekh.*, 2002, no. 35, pp. 23–31.
4. Barbashova, G.A., Vovchenko, A.I., Kamenskaya, L.A., and Shamko, V.V., Control of Hydrodynamic processes at Electroexplosive Programmed Multiple–Impulse Introduction of Energy, *Akust. Visnik*, 2004, vol. 7, no. 4, pp. 3–9.
5. Krivitskii, E.V., *Dinamika elektrovzryva v zhidkosti*, (Dynamics of Electric Explosion in Liquid), Kiev: Naukova Dumka, 1986.
6. Lependin, L.F., *Akustika*, (Acoustics), Moscow: Vysshaya Shkola, 1978.
7. Loitsyanskii, L,G., *Mekhanika zhidkosti i gaza*, (Fluid Dynamics), Moscow: Nauka, 1987.
8. Mukha, Yu.P. and Surkaev, A.L., Study of the Effect of Nonlinearity of the Interacting Shock–Acoustic Compression Waves, *Pis'ma Zh. Tech. Fiz.*, 2002, vol. 28, no. 15, pp. 43–47.
9. Fletcher, K. *Vychislitel'nye metody v dinamike zhidkostei*, (Computational Methods in Fluid Dynamics), vol. 2, Moscow: Mir, 1991.
10. Pirunov, U.G., *Chislennye metody*, (Numerical Methods), Moscow: Drofa, 2004.
11. Kalitkin, N.N., *Chislennye metody*, (Numerical Methods), Moscow: Nauka, 1978.
12. Smirnov, A.P., Application of the Semimplicit Numerical Method of Euler–Cauchy–Abarbanel and Zwas to the Solution of Time-Dependent Equation of Gas Dynamics, *Fiziko-tekhnichni problemi girnichogo virobnitstva*, 2005, pp. 121–128.
13. Khvoshchan, O.V., Kurashko, Yu.I, and Litvinov, V.V., On the Problem of Reduction of Mass and Overall Dimensions of the Submersible Electrical Discharge Complexes, *Electron. Obrab. Mater.*, 2009, no. 4, pp. 87–92.
14. Sinitsyn, V.V., *Plastichnye smazki v SSSR. Assortiment*, (Grease Lubricants in the USSR. Assortment), Moscow: Khimiya, 1979.
15. Shamko, V.V. and Kucherenko, V.V., Theoretical Elements of Engineering Analysis of the Power and Hydrodynamic Parameters of the Underwater Spark Discharge, *Preprint of Inst. of Pulse Processes and Technologies, Ukr. Nat. Acad. Sci*, Nikolaev, 1991, p. 52.
16. Shamko, V.V. Determination of Macroscopic Properties of Water–Oil Emulsions, *Materialy III nauchnoi shkoly "Impul'snye protsessy v mekhanike sploshnykh sred"*, (Proc. III Scientific School "Impulse Processes in Mechanics of Continua"), Nikolaev, 1999, pp. 97–98.

ISSN 1068-3755, Surface Engineering and Applied Electrochemistry, 2010, Vol. 46, No. 3, pp. 243–247. © Allerton Press, Inc., 2010.
Original Russian Text © V.M. Nagirnyi, S.V. Petrichenko, 2010, published in Elektronnaya Obrabotka Materialov, 2010, No. 3, pp. 53–58.

## ELECTRICAL PROCESSES IN ENGINEERING AND CHEMISTRY

# The Nature of Electrocrystallization of Metal Oxide Compounds

**V. M. Nagirnyi* and S. V. Petrichenko**

*Ukrainian State University of Chemical Engineering, Dnepropetrovsk, Ukraine*

**e-mail: petal@res.dp.ua*

Received January 19, 2010

**Abstract**—The article discusses the possible mechanisms of anodic formation of oxide compounds (by the example of $Co_2O_3$) and the relevant phase transformations during electrolysis in an aqueous solution of cobalt sulfate on the basis of an analysis of scientific papers and experimental data. The mechanism of anodic formation of $Co_2O_3$ molecules with the involvement of adsorbed oxygen and phase formation processes taking into account the volumetric structure of the oxide molecules is proposed. The surface morphology of the investigated sediments proves that they are built up by means of step growth of crystals and the formation of large-sized crystal grains displaying a certain tendency for spheroidization. Based on the Gibbs–Thompson equation for the electrochemical system, which correlates the value of the electrode potential with the radius and specific free surface energy of the nucleus, the possible energy relations of anodic nucleation of metal-oxide compound are considered.

**DOI:** 10.3103/S1068375510030099

Electrolytic oxide compounds are of significant interest as active cathode materials for chemical power supply units and, mainly, for lithium batteries because of their superior electrochemical characteristics and the ease and controllability of the processes of their production. Their obvious advantage is the capability to produce nonballast thin-layer cathodes on the basis thereof by direct sedimentation of oxide material on a metal substrate (stainless steel, aluminum) and, in particular, on the shell of an elementary cell of a power supply. The oxide materials that can be quantitatively evolved by anodic sedimentation from aqueous solutions among others include oxides of magnesium, vanadium, and cobalt ($MnO_2$, $V_2O_5$, and $Co_2O_3$), as well as various combinations thereof or with oxides of nickel and chromium (NiO, $Cr_2O_3$) in the form of multiphase oxide systems. The scientific and technological foundations of the electrolytic production of the aforementioned oxide materials are discussed in detail elsewhere [1 – 3]. However, these works do not sufficiently highlight the mechanism of the formation of oxide compounds on the anode surface and the involved processes of phase transformations. Some aspects of this problem are discussed elsewhere [4]. A more complete and detailed review of theses aspects is given below. Taking into consideration that, in the literature, there is a lack of data on the nature of electrocrystallization and, in particular, on mechanisms of the phase formation of metal oxide compounds, the present work could be valuable for the further development of the discussed method.

The electrocrystallization of metal oxide compounds is characterized by certain principal distinctions in comparison with the electrocrystallization of metals. Some of them are as follows:

- the final product of the respective electrochemical process is an oxide molecule of 3D-structure;
- the formation of the molecule takes place stepwise via intermediate molecular fragments;
- the anode sediment of the oxide compound cannot exist in the state of exchange equilibrium with the solution;
- the process of the phase formation of the metal oxide occurs at the simultaneous formation of a crystalline molecular lattice with account for the structural (geometric) and chemical affinity of the bonded molecules.

For the sake of simplicity, the case study involves the electrolytic synthesis of cobalt oxide ($Co_2O_3$); however, this pertains equally to the aforementioned oxide systems synthesized by electrolysis. This substance was obtained by anodic sedimentation from sulfate solutions ($CoSO_4 \cdot 7H_2O$) with concentrations of 0.03–0.035 mol $l^{-1}$ at 80 ± 3°C and pH 4–5 on a steel substrate (grade 12H18N9T).

The feasibility of electrosynthesis of $Co_2O_3$ is based on the electrode reaction [5]:

$$2Co^{2+} + 3H_2O - 2e \longrightarrow Co_2O_3 + 6H^+. \qquad (1)$$

At anodic polarization, this reaction, probably, includes a set of consecutive stages:

1—discharge of the cobalt ion ($Co^{2+} \longrightarrow Co^{3+}$);

2—formation and adsorption of the intermediate oxide ion $CoO^+$;

3—the surface interaction of the $CoO^+$ ions and the formation of the $Co_2O_3$ molecule itself; the

The current efficiency of cobalt oxide at electrolytic synthesis

| Temperature, °C | CE, wt % at $I_a$, mA/cm$^2$ | | | | |
|---|---|---|---|---|---|
| | 5 | 10 | 20 | 25 | 30 |
| 50 | 2.7 | 1.2 | 0.5 | – | – |
| 85 | 20 | 13.5 | 7.5 | 4.5 | 0.5 |

adsorption thereof on the anode surface creates backgrounds for the subsequent origination of a new phase.

The considered processes are closely related with the accompanying reaction of oxygen evolution. Therefore, it should be assumed that this reaction acts as a regulating factor determining the character and mechanisms of the studied process [6]. In particular, this is confirmed with the value of the current efficiency (CE) of the $Co_2O_3$, which only at the optimal conditions of the electrolysis ($t = 80$–$85$°C, pH = 4–5, $I_a = 5$–$10$ mA/cm$^2$) achieves 20 wt % (see Table).

On the basis of the recent theoretical concepts, it can be assumed that oxygen is evolved stepwise on the anode at the discharge of water molecules via the chemosorbed layer of its atoms [7]:

$$2[Me + H_2O - 2e \longrightarrow (Me\text{-}O) + 2H+]; \quad (2)$$

$$(Me\text{-}O) \longrightarrow 2Me + O_2; \quad (3)$$

$$H_2O - 4e \longrightarrow O_2 + 4H+. \quad (4)$$

If the aforementioned mechanism of the oxygen evolution is taken as the background, then the discharge of $Co^{+2}$ with the subsequent formation of

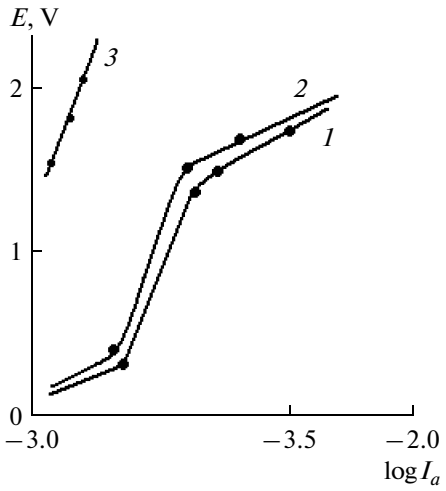


**Fig. 1.** $E$–log$I_a$ dependencies at anodic sedimentation of $Co_2O_3$ from a 0.035 mol/l $CoSO_4$ solution (pH 4–5, temperature 80 ± 3°C) on the steel substrate, grade 12H18N9T: (*1*) total dependency; (*2*, *3*) partial dependencies of the evolution of $O_2$ and $Co_2O_3$, respectively

$Co_2O_3$ can be presented in the form of successive reactions as follows:

$$Me + H_2O - 2e \longrightarrow (Me\text{-}O) + 2H+; \quad (5)$$

$$Co^{2+} - e \longrightarrow Co^{3+}; \quad (6)$$

$$Co^{3+} + (Me\text{-}O) \longrightarrow CoO^{1+} + Me; \quad (7)$$

$$Co^{2+} + (Me\text{-}O) - e \longrightarrow CoO^{1+} + Me; \quad (8)$$

$$2CoO^{1+} + (Me\text{-}O) \longrightarrow Co_2O_3 + Me; \quad (9)$$

$$2Co^{2+} + 3H_2O - 2e \longrightarrow Co_2O_3 + 6H^+.$$

These reactions cannot be eliminated by the reason of their mutual superposition and the overlapping of the rates of the evolution of the oxide and oxygen, which, according to [8], results in the quantitative modification of the nature of the electrode process. Therefore, the accompanying process of the oxygen evolution should be considered as a factor determining the general character of the kinetics of the anodic process. This is additionally confirmed by the comparison of the total and partial polarization curves of the evolution of the oxygen and $Co_2O_3$ in the $E$–log$I_a$ coordinates (Fig. 1) acquired under the aforementioned conditions. The slope coefficients of the curves amount to 0.55, 0.47, and 0.80 V, respectively (Fig. 1). The total and partial curves of the $O_2$ evolution actually coincide with each other and are characterized by close values of the slope coefficients; moreover, this secondary reaction at $I_a > 25$ mA/cm$^2$ completely suppresses the process of $Co_2O_3$ formation. The latter starts close to its standard electrode potential (1.49 V at the mentioned temperature and concentration of the solution) with the overvoltage that, according to the approximate estimation, is in the range of 0.1–0.15 V. In fact, it cannot be determined accurately due to occurrence of the aforementioned factors. Nevertheless, it should be assumed that the evolution of $Co_2O_3$ takes place at comparatively low power consumption (reactions 6, 9), and the most power consuming is, probably, reaction (6).

The $E$–log$I_a$ dependencies of the total anode process and the individual evolution of $O_2$ (Fig. 1) are broken curves consisting of three straight sections (zones I–III). Section I of the total dependency probably reflects a certain increase of the diffusion of $Co^{2+}$ ions stipulated by the anode polarization and the increase of the concentration thereof in the near-surface anode layer. However, already at a moderate value of the polarizing current, the diffusion current reaches the boundary region, which is spread up to the start of the evolution of $Co_2O_3$ (Section II). In this section, the further compaction of the ion layer occurs with the simultaneous formation of an external coating with a double layer related with the intrusion of $Co^{2+}$ ions in the adsorbed layer of the oxygen and the formation of its diffusion portion. At the same time, the potential of the oxygen evolution is reached and the discharge of $H_2O$ mole-

cules starts. Section III is responsible for the process of the evolution of the major anode product ($Co_2O_3$) together with oxygen. The high slope coefficient of this section and the close value of the slope of the partial $O_2$ curve indicate that the oxide is evolved under limit conditions determined by the diffusion rate of the $Co^{2+}$ ions. This is additionally confirmed by the abnormally high Tafel slope of the partial curve (3) of the $Co_2O_3$ formation (0.8 V), which is stipulated mainly by the significant concentration polarization. This agrees with the known generalized interrelation of the electrochemical and diffusional kinetics [9].

It is particularly remarkable that the high slope coefficient of the partial curve (curve 2) of the $O_2$ evolution (0.47 V) significantly differs from its theoretical value (0.12 V) available elsewhere. This can be attributed to the variations of the mechanism of the oxygen discharge under the action of the decelerating effect of the associated process of the $Co_2O_3$ formation. However, if it is assumed that the slope coefficients are added in a common process, then the assumed slope value of the curve (curve 2) can be expressed in terms of their difference, that is, $0.55 - 0.47 = 0.08$ V, and this is within reasonable limits.

The reaction (9) in the aforementioned stepwise mechanism of the formation of the $Co_2O_3$ molecule is in fact the initial stage of the electrolytic phase formation, since, at this phase, there occurs the quantitative transition to a new phase state. The energetic stability of a single molecule localized on the surface or a group thereof (crystallization center) of the developed crystalline nucleus is achieved due to the slight oversaturation of the system expressed in the given case by the imposing of an additional potential (superpotential), which equalizes the work of the surface forces aimed at the destruction of the center. The super-potential provides the nearly spontaneous development of the molecular crystalline nucleus up to a certain critical dimension corresponding to the minimum of free energy of the system. In [4], the correlation between the superpotential with the work of the formation of the stable crystalline nucleus ($r_{min}$) was determined by the Gibbs–Thomson ratio for the electrochemical system [10]:

$$\Delta\varphi = 2\sigma V/nFr,$$

where $\sigma$ is the specific free surface energy; $V$ is the molar volume of the oxide; and $n$, $F$, and $r$ are the valence, Faraday number, and nucleus radius, respectively.

On the basis thereof, the expression was developed interrelating the difference between the overvoltages at the start of the nucleation ($r_{min}$) and at the end of the formation of a stable molecular nucleus ($r_{cr}$) with the variation of the free energy of the system:

$$\Delta\varphi = \varphi_1 - \varphi_2 = 2V/nF(\sigma_1/r_{min} - \sigma_2/r_{cr}),$$

where, $\Delta\varphi$ is the anodic overvoltage, and $\varphi_1$ and $\varphi_2$ are the anode potential at the beginning (superpotential) and at the end of the formation of the molecular crystal nucleus, respectively.

Assuming that $\sigma/r = \sigma^*$, which stands for the specific free surface energy reduced to the given dimension of the formed nucleus, it can be written as follows (for $n = 2$):

$$\Delta\varphi = -\text{const}\Delta\sigma^*;$$

that is, the work of the formation of a stable molecular crystal nucleus amounts to the difference of its vales at the variation of the nucleus's dimension from $r_{min}$ to $r_{cr}$. It is quite obvious that here $\varphi_1 \longrightarrow \varphi_2$, thus determining in fact the potential of the evolution of the $Co_2O_3$ molecule. Under stationary conditions of the electrolysis after the formation of a continuous monomolecular layer of the oxide sediment, the anode potential is averaged and the superpotential forfeits its role of the factor that determines the energy of generation of a new phase on the foreign surface. This is stipulated by the fact that the formation of new nuclei on the homogeneous substrate is significantly facilitated in terms of energy at the growth of the sediment due to the appearance of structural defects, free vacancies, dislocations, and so on. Such an effect contributes to the direct embedding of the evolved molecules of the oxide, to developing crystalline lattices, to filling of free vacancies, to further growth of the planes of the molecular packages, and so on. Nevertheless, the difference between the initial ($\varphi_1$) and final ($\varphi_2$) polarizations at the nucleation plays the role of the key factor determining the structure of the sediments and the configuration and dimensions of the formed molecular-crystalline aggregates. The possible consequences of the correlation between these parameters are discussed elsewhere [11] for the case of electrocrystallization and metals; however, these results are also quite valid for the discussed processes of molecular phase formation. Thus, at $\varphi_1 \gg \varphi_2$, the accelerated discharge of $Co^{2+}$ ions provides the sufficient oversaturation of the $Co_2O_3$ molecules in the nucleation zone and the respective formation of crystalline nuclei. However, at this, the diffusion layer of the solution is rapidly depleted and the developed crystalline aggregates are already degraded at the initial stages of their development, which promotes the formation of fine crystalline sediments. At $\varphi_1 \geq \varphi_2$, the ion transport to the anode surface decreases, and the molecular oversaturation depends mainly on the diffusion mode; therefore, the evolved $Co_2O_3$ molecules continue the growth of the ready crystalline complexes. This promotes the layer-by-layer formation of bidimensional molecular-crystalline aggregates with the subsequent formation of growth steps of crystals, which is characteristic for the respective structures of the electrolytic sediments of $Co_2O_3$. The mechanism of the electrocrystallization in this case too is substantiated predominantly by overlaying of bidimensional crystalline aggregates, which form thickened packages–steps. Separate groups of crystals are "merged" into enlarged

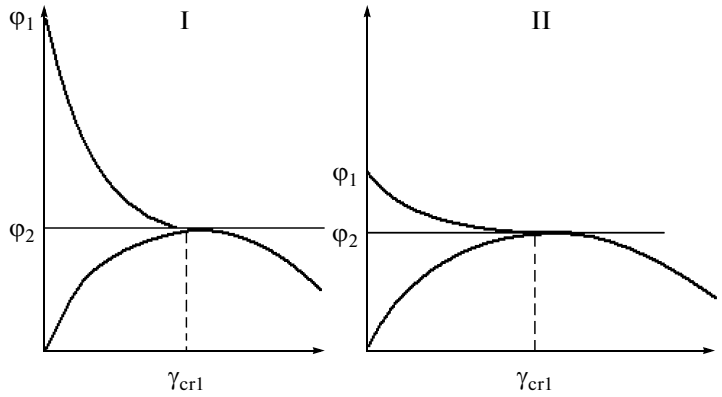


**Fig. 2.** Schematic view of the variations of the electrode potential φ at the formation of the molecular crystalline nucleus of the oxide phase on a foreign surface at changes of its size from a minimal ($r_{min}$) to stable ($r_{cr}$) value. I—at $\varphi_{init} \gg \varphi_{final}$; II—at $\varphi_{init} = \varphi_{final}$.

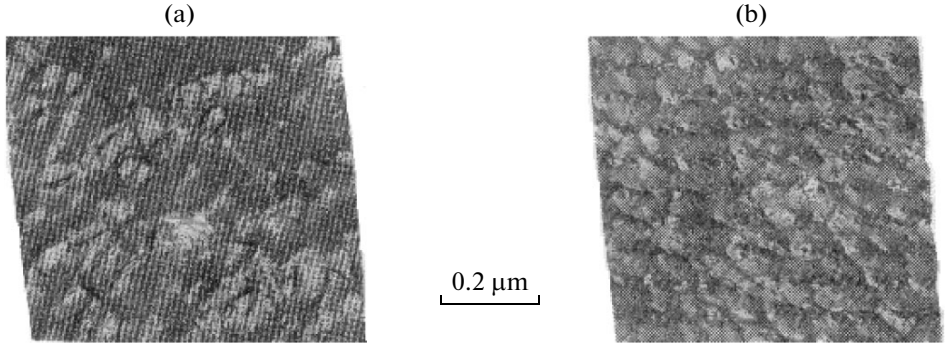


**Fig. 3.** Morphology of the surface of $Co_2O_3$ electrolytic sediments, 2–2.5 μm, obtained from a sulfate solution (with the conditions as in Fig. 1) at $I_a$, mA/cm$^2$ : (a) 7.5; (b) 10.

crystalline grains with a characteristic (for $Co_2O_3$) trend to smoothing the planes, which is possibly related with the haotic sedimentation of the oxide molecules at the growth steps at limited transport of the discharging $Co^{2+}$ ions. This also can be promoted by the tendency of the oxide to form crystalline hydrates $Co_2O_3 \cdot nH_2O$, resulting in the modification of its molecular structure.

The aforementioned interpretation of the various factors effecting the mechanism of the electrocrystallization of cobalt oxide should be supported by the consideration of the dimension of the crystalline nucleus, which is determined, in addition to the indicated energetic correlations, by the conditions of the electrolysis and the kinetics of the electrode process. From the Gibbs–Thomson equation, it can be seen that the greater the nucleus radius (the particle size), the lower the overvoltage of the nucleation is. Hence, it effects both the character of the formation of the developed molecular-crystalline aggregate and its structure. It is obvious that, at its limited size, the nucleation occurs predominantly by instant (cascaded) sedimentation of small 3D crystals, and their growth terminates at the initial stage as a result of the local depletion of the oversaturated phase. In this case, the anodic sediment is characterized by a fine crystalline homogeneous structure. At high radius of the nucleus, that is, at the absence of the factors that block its more or less free development along the substrate surface, the oversaturation is close to the equilibrium saturation and the crystallization process is substantiated by the formation of bidimensional molecular nuclei with their subsequent sedimentation on each other. The structure of the anodic sediments formed at this consists of enlarged crystals with characteristic protruded planes of crystalline packages in the form of growth steps. These cases are schematically illustrated in Fig. 2.

For $Co_2O_3$, the second principal case of nucleation is characteristic, which agrees with the observed morphology of the surface and the structure of the respective anodic sediments (Fig. 3). The surface of the sediments is characterized by the existence of a smoothed relief formed by uniformly and compactly distributed crystalline grains with markedly protruded growth steps. At this, the sediments obtained at the optimal current density (7.5 mA/cm$^2$, the remainder is con-

stant) are distinguished by their coarse structure with rounded geometry of the grains (Fig. 3, a), which stipulated by the aforementioned possible mechanism of their formation. At increased current density (10 mA/ccm$^2$), the appearing grains are developed predominantly in the form of small blocks with visible faceting, which probably should be related with the increased anodic polarization and the respective increase in the difference between $\varphi_{init}$ and $\varphi_{fin}$.

Therefore, the electrolytic phase's formation at anodic sedimentation of $Co_2O_3$ is significantly facilitated in terms of energy by the 3D structure of the oxide molecule, which could serve as base center of nucleation and growth of the molecular crystal. This, probably, can be promoted by the participation of intermediate $CoO^+$ oxide ions in the process, which can act as building material for the nucleated and growing crystals. At this, the $Co^{2+}$ discharge and the formation of the $Co_2O_3$ molecule are in fact the initial action of the molecular electrocrystallization.

## CONCLUSIONS

(1) The possible mechanisms of the anodic formation of oxide compounds, as well as of the respective phase transformations, at electrolysis from a solution of cobalt sulfate were discussed using the example of $Co_2O_3$.

(20 A mechanism of the stepwise formation of $Co_2O_3$ molecules with the participation of adsorbed oxygen and the process of phase formation accounting for the 3D structure of the oxide molecules was proposed.

(3) On the basis of the analysis of the morphology of the surface of the studied sediment, it was noted that its formation occurs by the stepwise growth of the crystals and the formation of separate enlarged grains tending to smooth the planes.

(4) On the basis of the Gibbs–Thompson equation correlating the value of the electrode potential with the radius and the specific free surface energy of the nucleus, the possible energy relations of the anodic nucleation of the metal-oxide compound ($Co_2O_3$) were discussed

## REFERENCES


1. Apostolova, R.D., Nagirnyi, V.M., and Shembel, E.M., Development and Studies of Cathode Material $LiCo_2$ on the Basis of Electrolytic Cobalt Oxides, *Elektrokhimiya*, 1998, vol. 34, no. 7, pp. 778–784.
2. Nagirnyi, V.M., Apostolova, R.D., Baskevich, A.S., et al., Electrolytic Sedimentation of Cobalt Oxide(III) in the Presence of Ions of Nickel(II) and Chromium(III), *J. Appl. Chem.*, 2002, vol. 75, no. 6, pp. 924–928.
3. Nagirnyi, V.M., Apostolova, R.D., and Shembel, E.M., *Sintez i elektrohimicheskie harakteristiki elektroliticheskih metall-oksidnyh soedinenij dlya litievykh akkumulyatornyh system* (Synthesis and Electrochemical Characteristics of Electrolytic Metal Oxide Compounds for Lithium Batteries), Dnepropetrovsk: VUZ UGHTU, 2008, p. 260.
4. Nagirnyi, V.M. and Artamonov, V.G., Anodic Processes at Electrolytic Formation of Oxide Compounds, *Vopr. Khim. Khim. Tekhnol.*, 2009, no. 2, pp. 151–155.
5. *Spravochnik po elektrokhimii* (Handbook of Electrochemistry), Sukhotin, A.M., Ed., Leningrad: Khimiya, 1986.
6. Fetter, K., *Elektrokhimicheskaya kinetika* (Electrochemical Kinetics), Moscow: Khimiya, 1967.
7. Tsu-Yun-Tsao, Major Aspects of Modern Electrochemistry, *Trudy 14-20 soveschaniya Mezhdunardnogo komiteta po elektrokhimii, termodinamike i kinetike)* (Proc. 14-20 Congress of International Committee for Electrochemistry, Thermodynamics, and Kinetics), Moscow: Mir, 1965, pp. 335–363.
8. Frumkin, A.N., Bagotsky, V.S., Iofa, Z.A., and Kabanov, B.N., *Kinetika elektrodnykh protsessov* (Kinetics of Electrode Processes), Moscow: Mosc. Gos. Univ.
9. Scorcheletti, V.V., *Teoreticheskaya elektrokhimiya* (Theoretical Electrochemistry), Leningrad: GosNTI po Khim. Lit., 1959.
10. Danilov, A.I., Polukarov, Yu.M., Modern Concepts of Processes of Formation and Development of Nuclei under Potential Static Conditions, *Usp. Khim.*, 1987, vol. VLI, no. 7, pp. 1082–1103.
11. Nagirnyi, V.M. and Chaikovskaya, V.M., Mechanisms of Formation of Fine Sediments of Metals on Cathode, *Vopr. Khim. Khim. Tekhnol.*, 1974, no. 33, pp. 41–45.

ISSN 1068-3755, Surface Engineering and Applied Electrochemistry, 2010, Vol. 46, No. 3, pp. 248–252. © Allerton Press, Inc., 2010.

ELECTRICAL PROCESSES
IN ENGINEERING AND CHEMISTRY

# Depolarization of the Fluorescence in Donor-Acceptor Pair under Periodic Electric Field[1]

**O. V. Yaltychenko**

*Institute of Applied Physics, Academy of Sciences of Moldova, 5 Academiei str., Kishinev, MD-2028, Republic of Moldova*
*e-mail: oialt@mail.ru*

Received February 9, 2010

**Abstract**—The donor-acceptor pair in the external periodic electric field is under studying. The molecular system is excited by the short impulse of the polarized light, and the electronic excitation initially localized on the donor and interacts only with full symmetrical vibration of the ligand environments, thus the vibrational subsystem forms the package in the form of the coherent state. Donor and acceptor molecules are assumed as identical type of the molecules. The time dependence of the depolarization of the fluorescence is numerically calculated on the basis of the semi-phenomenological model. Numerical estimates are given for cases of the strong and weak electron-vibrational interaction. Transfer of the excitation in the system is defined by the non-linear properties of the system, especially in the case of strong electron-vibrational interaction. The depolarization of the fluorescence is consequence of the such transport and contains the interference addends which conduct to the quantum beats in the time dependence.

**DOI:** 10.3103/S1068375510030105

## INTRODUCTION

Kinetics of the transfer of excitation between donor and acceptor groups in nanostructures and supramolecular complexes and elaboration of the theoretical model for describing of the features of such type of the transfer are actual problems of optoelectronics, molecular, sensor electronics and biophysics. The given theoretical investigation is devoted to elaboration of the two-level semi-phenomenological model featuring the kinetics of the transfer of the excitation between the donor and acceptor in the molecular complex in the external periodic electric field.

The given investigation is theoretical result, however has also practical value. First, the given investigation is showing how in dependence from the relation of the basic parameters of the system it is possible to model and to control processes of the transfer of excitation during biochemical processes with the participation of the biomacromolecules. Secondly, supramolecular complexes and nanostructures with the donor-acceptor groups are the functional elements of the devices of the optoelectronics and the molecular electronics and parametric guidance of the processes of the transfer is extremely important.

Now existing time-resolved experimental techniques which allow to detect superposition of the quantum states in the different biochemical molecular systems. In addition, these states are the functional states in the applications of the bioinformatics, quantum computers, molecular electronics and the molecular engineering [1].

Time evolution of the superposition of the quantum states of the molecular complexes and nanostructures can have experimentally observable physical quantities. Among the observable effects is the depolarization of the fluorescence. Evolution of the superposition of the quantum states which take place in the molecular complexes by means of the observation of the time dependence of the depolarization of fluorescence is theoretically explored in this article.

The system of the non-interacting molecules with donor and acceptor groups is under investigation. For the analysis we shall take the donor and the acceptor groups are identical. The molecular system is excited by the short impulse of polarized light, and the electronic excitation is initially localized on the donor and interacts only with full symmetrical vibration of ligand environments, thus the vibrational subsystem forms the package in the form of the coherent type of the state. The excited state of acceptor group of the pair is resonant for the excited state of the donor because of the complete equivalence of the donor and acceptor groups. Account of the interaction with vibrational degrees of freedom essentially modifies the dynamics of the transport of the excitation from the donor to the acceptor.

Since the donor and acceptor are identical molecules the fluorescence is not affected but depolarization of the fluorescence will be affected, because the "memory" of the initial polarization is lost. For simplicity we assume that both dipole moments on the donor's and acceptor's molecules to be coplanar and mutually perpendicular. Creating the excitation of the donor-acceptor pair which is localized on the donor

[1] The article is published in the original.

molecule by the light polarized in the direction of the dipole moment on that molecule. If the intensities of the parallel fluorescence and perpendicular fluorescence to the direction of the polarization of the incident light are $I_{II}$, $I_{\perp}$ then degree of the depolarization of the fluorescence is

$$f = (I_{II} - I_{\perp})/(I_{II} + I_{\perp}). \quad (1)$$

For the investigation of the excitation transfer within the pair this is convenient observable value. It is clear, that the intensity of the fluorescence in the direction of the unit vector $e_\eta$ is given by [2, 3]

$$I_\eta = \sum_{m,n} \rho_{mn}(\mu_m e_\eta)(\mu_n e_\eta) \quad (2)$$

$\mu_m$ are dipole moments in excited states of the donor and acceptor, $\rho_{mn}$ are components of the density matrix. In the basis of the local states indexes m and n may be 1 or 2.

If the angle between the polarization of the incident light and transition dipole moment of the donor's excited state-1 and acceptor excited state-2 is φ we can write (see Fig. 1)

$$\mu_1 e_{II} = \mu_2 e_{\perp} = \cos\varphi, \quad \mu_1 e_{\perp} = -\mu_2 e_{II} = -\sin\varphi. \quad (3)$$

## SEMI-PHENOMENOLOGICAL MODEL

The excitation transfer process in the donor-acceptor pair under the action of the sinusoidal electric field which interacts only with the dilatational component of the dipole moment of the donor and acceptor groups is proposed.

In this paper we have calculated some factors of the theory of the depolarization of the fluorescence for the excitation transfer process in the donor-acceptor pair under the action of the sinusoidal electric field. It is assumed that for the donor-acceptor pair takes place the resonance of the energy of the lower excited levels. Other excited levels are essentially removed from this pair of the levels so the interaction with them is not considered. The approach of the two-level system is taken unto accounts. It is assumed, that the excitation which is localized on the donor or on the acceptor group interacts only with full-symmetrical vibration of the ligands of this group. Introduction of the new normal coordinates allow exclude one of the new normal coordinates as the full-symmetrical increased on the unit electronic matrix.

Using for the calculations the two-level model Hamiltonian from [4] and assuming that the vibrational subsystem is in the coherent type of the state we realize the plan of the calculation of the time dependence of the average values of the physical quantities grounded on use of the canonical equations of Hamilton and the approximation for the time wave function in the form of the Davydov's type of the soliton [5].

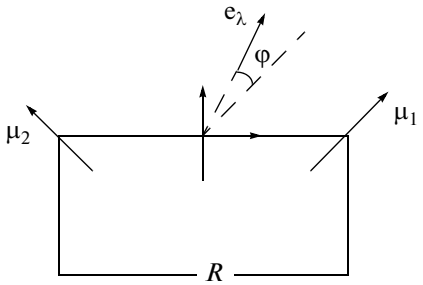


**Fig. 1.** Geometry of the particular planar dipole moment of the donor-acceptor pair. Vectors $\mu_1$, $\mu_2$ are perpendicular and equal in length. The unit vector $e_\lambda$ lies along the polarization vector of exciting light, and the angle φ is measured from the direction of $\mu_1$.

The Hamiltonian of the considered system is:

$$H(t) = \frac{1}{2}(p^2 + \omega_0^2 q^2) + \nu(a_1^+ a_2 + a_1 a_2^+) + gq(a_1^+ a_1 + a_2^+ a_2) + \mu_{II}\varepsilon_0 \cos(\Omega t)(a_1^+ a_1 + a_2^+ a_2) \quad (4)$$

Here $-p$, $q$ are the momentum and coordinate of the vibrational mode $q$ with frequency $\omega_0$; $a_i^+$, $a_i$ – are the operators of the creation and annihilation of the excitation on the donor – 1 and acceptor – 2 groups correspondently; $v$, $g$ are the resonance electronic constant and constant of the electron-vibrational interaction; $-\varepsilon_0$, $\Omega$ are the magnitude and the frequency of the sinusoidal electric field, $\mu_{II}$ is the longitudinal component of the dipole moment of the excited state of the donor group, induced by the short-time polarized light.

In this work the quasi-classical approximation was used. Davydov's type of the time-dependent wave function in Hamilton canonical equation of the motion for the description of the time evolution of the depolarization of the fluorescence was applied

$$\psi(t) = \exp\left(-i(\beta(t)p - \pi(t)q)\sum_{j=1}^{2}\alpha_j a_j^+|0\rangle\right). \quad (5)$$

The system of the linkage differential equations for the amplitudes was obtained:

$$i\frac{d\alpha_1}{dt} = \nu\alpha_2 + g\beta\alpha_1 - \mu_{II}\varepsilon_0\alpha_1\cos(\Omega t) - i\frac{\alpha_1}{\tau_1}$$

$$i\frac{d\alpha_2}{dt} = \nu\alpha_1 + g\beta\alpha_2 - \mu_{II}\varepsilon_0\alpha_2\cos(\Omega t) - i\frac{\alpha_2}{\tau_2} \quad (6)$$

$$\frac{d\pi}{dt} = -\omega_0\beta + g[|\alpha_1|^2 - |\alpha_2|^2]$$

$$\frac{d\beta}{dt} = \pi.$$

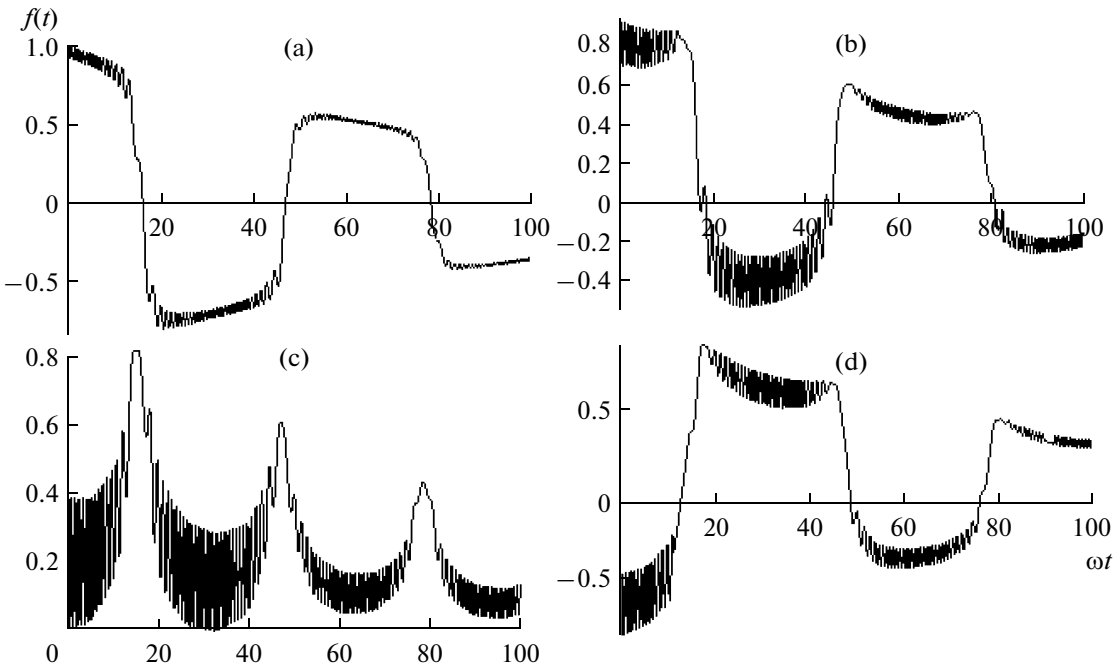


**Fig. 2.** Time dependence of the depolarization of the fluorescence for the next parameters of the system: $\nu = 1$, $g = 0.1$, $\mu_{II}\varepsilon = 5$, $\omega_0 = 1$, $\Omega = 1$, $\tau = 0.005\omega_0$, $\varphi = 0, \pi/4, \pi/2, 3\pi/2$, (a)–(d).

To consider the excitation lifetime on the donor and on the acceptor the relaxation times are phenomenologically entered. The dilatational excitation lifetime is characterizing the relaxation of the diagonal density matrix elements caused by the spontaneous transitions between the levels. The traversal relaxation time for the non-diagonal matrix elements is characterizing the time of the infringement of the phase relations between the states – "time of phase memory". In the formula (6) are phenomenologically entered $\tau_1$, $\tau_2$ as the dilatational relaxation times characterizing the excitation lifetime on the donor and on the acceptor groups accordingly. As the donor and acceptor group are accepted identical, so $\tau_1 = \tau_2$ and the time of the traversal relaxation in such approach will be spotted as

$$\frac{1}{T_\perp} = \frac{2}{\tau}.$$

Here $\alpha_j(t)$, $j = 1, 2$; $\beta(t)$, $\pi(t)$ are the time-dependent amplitudes of the probability of the electron's detection on the excitation state of the donor or on the acceptor excitation state and the average values of the coordinate and momentum of the vibrational mode, correspondently.

Time dependence of the fluorescence of the depolarization through the solutions of the system (6) can be spotted as follows using the reasons presented above

$$f = \left(|\alpha_1(t)|^2 - |\alpha_2(t)|^2\right)\cos(2\varphi) + \left(\alpha_1(t)\alpha_2^*(t) + \alpha_1^*(t)\alpha_2(t)\right)\sin(2\varphi). \quad (7)$$

## RESULTS AND CONCLUSION

The main results of the given consideration, which follow from the numerical solution of (6) are presented on the Figs. 2–4.

On the Figs. 2–4 the time dependence of the depolarization of the fluorescence for the some values of the parameters of the system is presented. For reasoning some values of the parameters of the system which brightly show features of the transfer in the model system in the two extreme cases of the strong and weak electron-vibrational interaction are chosen.

The analysis of the numerical solution (6) presented by the time dependence of the depolarization of the fluorescence of the donor-acceptor pair on Fig. 2–4 allows to make following conclusions. The cases presented on the Fig. 2–3 correspond to the case of the weak electron-vibrational interaction.

Non-linear effects taking place for the case of the strong electron-vibrational interaction in this case may be neglected. Quantum beats of the time dependence of the depolarization of the fluorescence are the

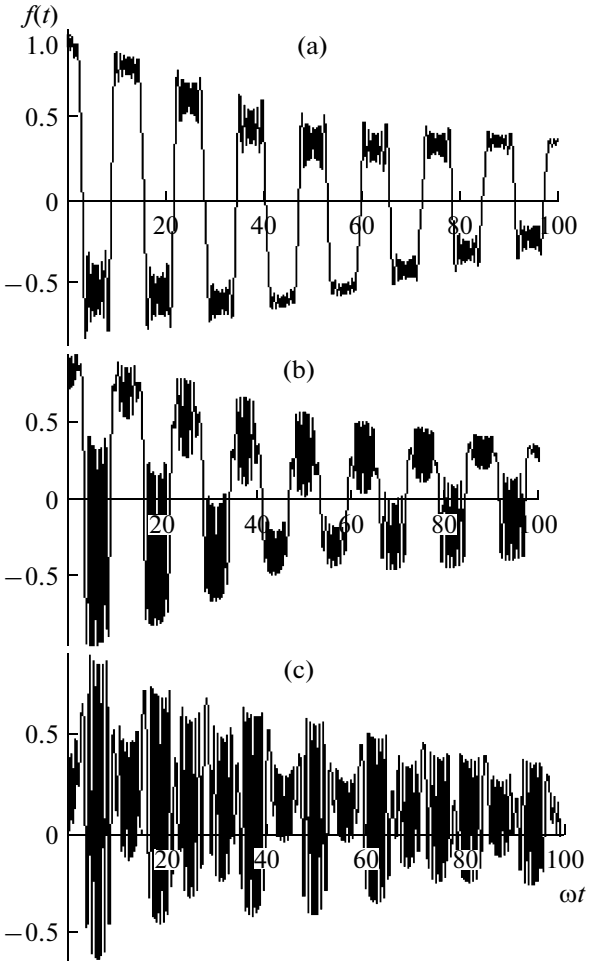


**Fig. 3.** Time dependence of the depolarization of the fluorescence for the next parameters of the system: $\nu = 1$, $g = 0.1$, $\mu_{II}\varepsilon = 5$, $\omega_0 = 1$, $\Omega = 5$, $\tau = 0.005\omega_0$, $\varphi = 0$, $\pi/4$, $\pi/2$, (a)–(c).

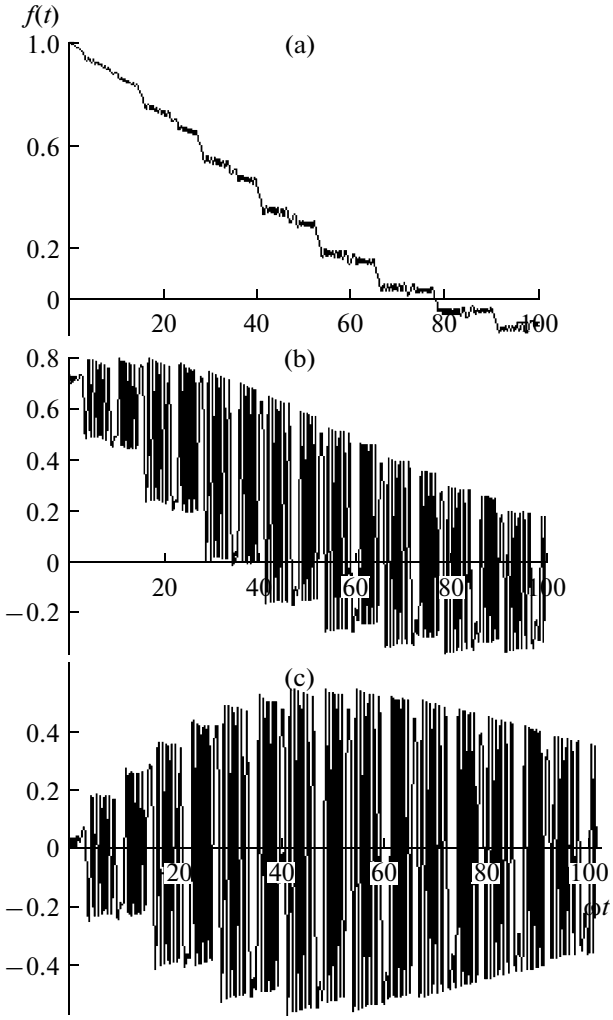


**Fig. 4.** Time dependence of the depolarization of the fluorescence for the next parameters of the system: $\nu = 0.1$, $g = 1$, $\mu_{II}\varepsilon = 5$, $\omega_0 = 1$, $\Omega = 5$, $\tau = 0.005\omega_0$, $\varphi = 0$, $\pi/4$, $\pi/2$, (a)–(c).

consequence of the interference of the excited states of the donor and acceptor of the donor-acceptor pair.

On the Fig. 4 the case of the strong electron-vibrational interaction when it is important to consider non-linear effects is presented.

Let's analyze the case a) Fig. 4, when the corner between the dipole moment of the system and the vector of polarization of radiation $\varphi = 0$. In this case influence of the interference addends may be neglected.

The strong electron-vibrational interaction interferes in the transport of the excitation from the excited state of the donor to the excited state of the acceptor and essentially influences on the character of the fluorescence of the donor-acceptor pair. The time dependence of the depolarization of the fluorescence varies monotonously. Whereas for the cases b) and c) Fig. 4. ($\varphi = \pi/4$, $\pi/2$) the contribution from the interference addends is essentially the monotonous time dependence of the depolarization of the fluorescence is modified by the quantum beats.

Thus, for the donor-acceptor pair interacting with exterior periodic electric field and being in the excited state in the form of superposition of quantum states in the two-level approach were detected the features of the time behavior of the depolarization of fluorescence. This model allows to consider non-linear properties of the system, and also to consider the role of the interference of the quantum states on the dynamics of the transfer of the excitation from the donor to the acceptor in the molecular complex under external electric field.

The cases of the strong and weak electron-vibrational coupling were analyzed. The essential role of the interference of the quantum states is specified in the processes of the energy transfer in this system. This consideration has doubtless interest from the point of view of the studying of the functional devices of the optoelectronics, bioinformatics, molecular and sensor electronics and quantum computers.

## REFERENCES

1. Femtochemistry, *Ultrafast Chemical and Physical Processes in Molecular Systems,* M. Chergui, Ed., Singapore: World Scientific, 1996.
2. Rahman, T.S., Knox, R., and Kenkre, V.M., Theory of depolarization of fluorescence in molecular pairs, *Chem. Phys*, 1979, vol. 44, pp. 197–211.
3. Kenkre, V.M. and Tsironis, G.P., Theory of fluorescence depolarization from nonlinear Schrodinger equation, *Chem. Phys.*, 1988, vol. 128, pp. 219–226.
4. Yaltychenko, O.V. and Kanarovskii, E.Yu., Dynamics of the nonstationary state of an electron in a dimer nano-cluster, *Surface Engineering and Applied Electrochemistry*, 2009, vol. 45, no. 4, pp. 55–61.
5. Yaltychenko, O.V. and Kanarovskii, E.Yu., Electron transfer in the molecular complex of donor-polymer-acceptor, *Analele Universitatii Bucuresti – Chimie*, 2009, vol. 1, pp. 9–13.

ISSN 1068-3755, Surface Engineering and Applied Electrochemistry, 2010, Vol. 46, No. 3, pp. 253–262. © Allerton Press, Inc., 2010.

## ELECTRICAL TREATMENT OF BIOLOGICAL OBJECTS AND FOOD PRODUCTS

# Denitrification of Brackish Water by Electrodialysis: Effect of Process Parameters and Water Characteristics[1]

**Mourad Ben Sik Ali[a], Amine Mnif[b], Bechir Hamrouni[b], and Mahmoud Dhahbi[a]**

[a]*Water and Membranes Technologies laboratory, CERTE, BP. 273, Soliman 8020, Tunisia*

[b]*Chemistry department, Tunis Faculty of Sciences, 2092 Manar II, Tunisia*

*e-mail: mourad.bensikali@gmail.com*

Received February 9, 2010

**Abstract**—The aim of this work is to study the removal of nitrate from brackish polluted water using electrodialysis. The influence of several parameters, such as flow rates, initial feed concentration, co-existing anions and initial pH on process efficiency were studied. This efficiency is evaluated by the removal rate, demineralization rate and power consumption. The denitrification process showed to be independent of pH of feed solution. Although The flow rate as well as the initial salt concentration and also the coexisting anions on the feed solution play a significant role on the denitrification efficiency and mainly on the specific power consumption. The decrease of this parameter induces a decrease on the total energy needed to perform required operation. The denitrification of a contaminated real water sample was investigated so as to improve the efficiency of denitrification process. The nitrate concentration could be reduced from 225 to 25.5 mg $L^{-1}$ (88% removal) which was lower than World Health Organization (WHO) standard (50 mg $L^{-1}$). Moreover the concentrations of different species in the obtained treated water are below the amounts recommended by WHO for drinking water.

**DOI:** 10.3103/S1068375510030117

## 1. INTRODUCTION

Tunisia is characterized by semiarid climate and by limited conventional water resources especially groundwater resources. These underground waters represents an important resource exploited for human consumption, for agricultural and for industrial use [1, 2]. Owing to these activities, the nitrate concentration in surface and groundwater have increased to such an extent that the admitted standards in drinking water have been largely exceeded in many regions [3]. In fact Nitrate pollution is caused by the intensive use of nitrogen fertilizers, crop irrigation with domestic wastewater and use of manure. Therefore, it is concern of diffuse pollution. A maximum limit of 50 mg $L^{-1}$ $NO_3$ in drinking water is permitted [4]. Nitrate contaminated water above these limit is considered as toxic to human health, specifically to children [4–6].

A survey of literature yielded an abundance of information on the technical treatment to remove nitrate from water. Different approaches have been proposed and proven. The typical process can be grouped into chemical, physical and biological denitrification processes [5–17]. Biological and chemical denitrification needs a continuous monitoring, such as addition of a carbon source, pH control, temperature maintenance, and also requires the removal of by-products such as nitrite [5, 7, 8]. Extractive methods like reverse osmosis and ion exchange resins are also largely used to remove nitrates. However, these techniques produce a large amount of effluents, which must be treated later and therefore increase the overall cost of the process [7, 8, 11]. The interest in using of electrodialysis processes to remove excess inorganic contaminants such as boron ($B(OH)_4^-$), fluoride ($F^-$) and nitrate ($NO_3^-$) from drinking water has increased worldwide principally because it is a simple process and does not have many of the defects of chemical processes [18–24]. Some studies were conducted and demonstrated that electrodialysis is a reasonable process for removing these inorganic contaminants from brackish water [14–24].

The electrodialysis is a widely used electro-membrane process especially for desalination of brackish water and sodium chloride recovery from sea water. The removal of ionic components from aqueous solution through ion exchange membranes is carried out under the driving force of an electrical field [25–27].The mandatory condition for an electrodialysis process to be executed is an alternating order of cation and anion membranes and electric field applied across the entire assembly (Fig. 1).

When a direct current is applied between two electrodes, the charged cations will move to the cathode passing through the cation exchange membrane but they will be retained by the anion exchange membrane. Conversely, charged anions will move to the anode through the anion exchange membrane and

[1] The article is published in the original.

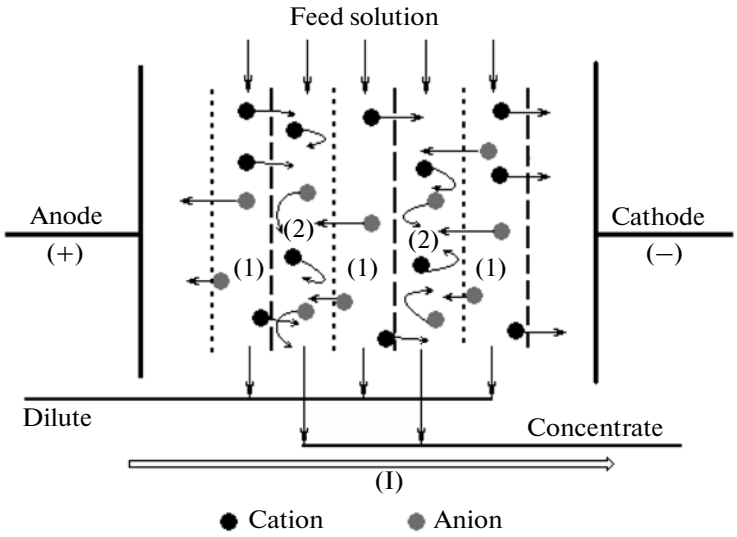


**Fig. 1.** Principle of electrodialysis.

they will be retained by the cation exchange membrane. While the negatively charged anions move to the anode, passing through the anion exchange membrane and retained by the cation exchange membrane. The two types of membranes create alternately two compartments. These compartments will accumulate the ions because the ion exchange membrane between them would prevent ions from moving further. Therefore the solution in the even compartments (1) will be demineralised and solution in the odd compartments (2) will be concentrated. As a result the entire flow incoming to the electrodialysis apparatus can be separated into desalinated and concentrated streams. These flows are called respectively dilute and concentrate.

The aim of this work is to study the removal of nitrate from polluted water using electrodialysis. The influence of several parameters, such as flow rates, initial feed concentration, co-existing anions and initial pH on process efficiency were studied. This efficiency is expressed by the removal rate, demineralization rate and power consumption. At the end, the denitrification of a contaminated groundwater real sample also was investigated so as to improve the efficiency of denitrification process.

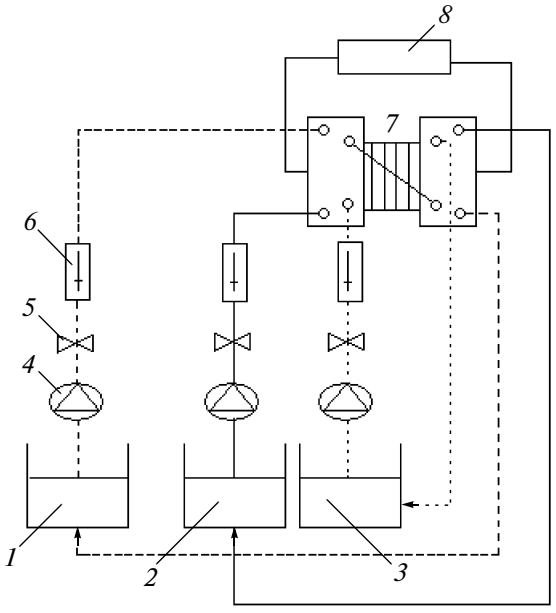


**Fig. 2.** Schematic of the ED system used in this study.

## 2. MATERIALS AND METHODS

### *2.1. Electrodialysis Equipment and Membranes*

The ED setup consists of: a power DC, a brine tank, a feed tank, an electrode rinse tank, three centrifugal pumps ($P$ = 84 W, total head = 4.2 m) equipped each with a flowmeter and three valves to control feed flow rate in the compartments of ED cell. Figure 2 shows a simplified diagram of the ED setup working in batch recirculation mode.

The electrodialysis operation was carried out on a laboratory stack "PCCell ED 64 002" supplied by PCA-Polymerchemie Altmeier GmbH and PCCell GmbH, Heusweiler, Germany. ED cell is packed with ion exchange membranes (cation and anion), spacers and a pair of electrodes (anode and cathode). Both electrodes are made of Pt/Ir-coated Titanium. The membranes and spacers are stacked between the two electrode-end blocks. Plastic separators are placed between the membranes to form the flow paths of the dilute and concentrate streams. These spacers are designed to minimize boundary layer effects and are arranged in the stack so that all the dilute and concen-

**Table 1.** Information on PCA standard cation and anion exchange membranes

| Membrane | Thickness, μm | Ion exchange capacity, meq $g^{-1}$ | Chemical stability (pH) | Permselectivity | Functional groups | Surface potential, Ohm $cm^2$ |
|---|---|---|---|---|---|---|
| PC-SK | 130 | ~1 | 0–11 | >0.93 | $-SO_3^-$ | 0.75–3 |
| PC-SA | 90–130 | ~1.5 | 0–9 | >0.96 | $-NR_4^-$ | 1–1.5 |

trate streams are manifolded separately. In this way a repeating section called a cell pair is formed; it consists of a cation exchange membrane, a dilute flow spacer, an anion-exchange membrane, and a concentrate flow spacer. In this work, experiments were carried out by this stack equipped with three cation exchange membranes (CEM) and two anion exchange membranes (AEM). For each membrane, the active surface area is 0.0064 $m^2$ and the flow channel width between two membranes is 0.5 mm. PCA-SK standard cation exchange membranes and PCA-SA standard anion exchange membranes are used in the stack. Furnished informations by the manufacturer about the membranes are given in Table 1. The ED system is designed to handle 2–5 L laboratory batches.

### *2.2. Reagents*

Analytical grade sodium chloride, sodium nitrate, magnesium chloride, calcium chloride and sodium sulphate salts are used in all experiments to produce solutions with known amount of salts and electrode rinse solution. Distilled water was used throughout.

### *2.3. Real Water Sample*

Brackish water sample with total dissolved salts TDS around 15 g $L^{-1}$ was taken from underground water in the region of Borj-Cédria (Tunis City). Since an electrode overheating can occur in the ED system for the treatment of solution with relatively high salinity (TDS over 5 g $L^{-1}$), this sample was diluted by mixing it with raw water to reduce the total salinity until 5 g $L^{-1}$. And because the measured concentration of nitrate, 25 mg $L^{-1}$, was below the maximum recommended concentration by WHO, small amount of sodium nitrate salt was added to this sample to simulate a contaminated one. The physico-chemistry characteristics of obtained sample are given in Table 2.

### *2.4. Experiment and Analysis Methods*

**2.4.1. Experimental procedure.** During the experiments, the volume of dilute, concentrate and electrode rinse solution was 2 L. As initial concentrate and dilute, the same solution was used. Prior to the experiments, pH was adjusted by the addition of 1 M HCl and/or NaOH. 0.1 M $Na_2SO_4$ was used as electrode rinse solution circulating in electrode compartments, in order to prevent the generation of chlorine or hypochlorite, which could be hazardous for the electrodes. Flow rate of electrode rinse solution was fixed to 80 L $h^{-1}$ for all experiments. Although the flow rate of other solutions (dilute and concentrate) were fixed at the beginning of experiment. Dilute and concentrate were recirculated through the ED cell at a these flow rates until the desired product concentration or total dissolved salts (~0.5 g $L^{-1}$) was achieved in the dilute.

The applied current density across the ED cell was fixed at a value below the limiting current ($I_{lim}$) which is determined by primary tests. Total voltage drop, including voltage drop in the membrane stack as well as on the electrodes, was measured in the experiments.

**Table 2.** Composition, pH and conductivity of brackish water Sample

| Physico-chemistry parameter | |
|---|---|
| Conductivity at 25°C, μS $cm^{-1}$ | 5.008 |
| pH | 7.2 |
| $F^-$, mg $L^{-1}$ | 2.9 |
| $Cl^-$, mg $L^{-1}$ | 2674 |
| $HCO_3^-$, mg $L^{-1}$ | 202 |
| $NO_3^-$, mg $L^{-1}$ | 225 |
| $SO_4^{2-}$, mg $L^{-1}$ | 707 |
| $Na^+$, mg $L^{-1}$ | 1041 |
| $K^+$, mg $L^{-1}$ | 300 |
| $Ca^{2+}$, mg $L^{-1}$ | 235 |
| $Mg^{2+}$, mg $L^{-1}$ | 127.6 |
| TDS, mg $L^{-1}$ | 5424 |

Samples from dilute and concentrate were collected at the beginning and at 5 min intervals for analysis.

After the completion of each experiment, cleaning solutions of 0.1 M HCl, 0.1 M NaOH and ul-trapure water were circulated through the ED cell for 30 min each in order to remove any deposits.

**2.4.2. Analytical methods.** The electrical conductivity (EC) of samples taken from the dilute and concentrate during each experiment was measured using a 712 Conductometer (Metrohm AG, Switzerland). $Ca^{2+}$ and $Mg^{2+}$ amounts were determined by atomic absorption spectroscopy using an analytical AAS Vario 6 spectrometer. $Na^+$ and $K^+$ were analyzed by atomic emission spectroscopy using a Jenway PFP 7 spectrometer. Sulphate and chloride anions were determined by ion chromatography using a Metrohm 761 Compact IC with conductivity detection (Metrohm AG, Switzerland). The anion chromatography measurements with chemical suppression were made with a Metrosep anion dual 2 column (4.6 × 75 mm) with a particle diameter of 6 μm.

654 pH-metre (Metrohm AG, Switzerland) equipped with a glass electrode was used for measuring pH solutions.

$NO_3^-$ concentrations were determined using ion-selective electrodes (ISE) in conjunction with a standard reference electrode connected to a Metrohm 781 Ion Meter (Metrohm AG, Switzerland). The ISEs were regularly calibrated and cleaned using standard methods. Standards and samples were mixed with a total ionic strength adjustment buffer (TISAB) to avoid possible interferences resulting from changes in solution pH and conductivity.

**2.4.3. Data analysis.** The purpose of the experiments was to study the effects of several parameters on ED cell performance. All figures and tables refer to concentration changes in the dilute. The mass balance of the ions present in the feed solution was verified for dilute, concentrate and electrode rinse solution. Thus, data for concentrate and electrode rinse solution will not be presented in this article.

**2.4.3.1. Determination of the demineralization rate.** The conductivity allowed following the demineralization rate [28, 29]. The demineralization rate can be calculated as:

$$DR(\%) = 100\left(1 - \frac{EC_t}{EC_0}\right),$$

where $DR$ is the demineralization rate expressed in percentage, $EC_0$ and $EC_t$ are, respectively, the initial and conductivity of the dilute, expressed in μS $cm^{-1}$.

**2.4.3.2. Determination of the flux and removal of nitrate.** The flux values were evaluated for all experimental conditions in order to compare to transport of nitrate ions from feed to receiver phase. The flux of nitrate ion (J) was determined by using the following equation [20]:

$$J(\text{mol cm}^{-1}\text{s}^{-1}) = \left(\frac{V}{A}\right)\left(\frac{\Delta C}{T}\right),$$

where $V$ is the volume of receiver phase (L), $A$ is the effective membrane area ($cm^2$), $C$ is the transported amount of nitrate at a time (mol $L^{-1}$) and $T$ is the period time (s).

The removal of nitrate was defined as [20]:

$$R(\%) = 100\left(1 - \frac{C_t}{C_0}\right),$$

where $C_t$ is nitrate concentration (mol $L^{-1}$) in dilute compartment, and $C_0$ is the initial concentration of nitrate in the feed phase (mol $L^{-1}$). To compare the removal of nitrate ions, the percent removal was evaluated for all experiments.

**2.4.3.3. Determination of the limiting current ($I_{lim}$).** In electrodialysis, concentration polarization takes place at the membrane surface. The magnitude of the concentration polarization is a function of various parameters including the applied current density, the feed flow velocity parallel to the membrane surface, the cell design, and the membrane properties [30–34]. The transport of charged species to the anode or cathode through a set of ion exchange membranes leads to a concentration decrease of counter-ions in the laminar boundary layer at the membrane surface facing the dilute cell and an increase at the surface facing the concentrate cell. When the ion concentration at the surface of the cation and/or anion exchange membranes in the cells with the depleted solution, the dilute, will become zero, the current density will approach to the maximum value in the process, which is defined as the limiting current density (LCD) [34].

The limiting current density in the electrodialysis process is an important parameter which determines the electrical resistance and the current utilization. It is generally accepted that an electrodialysis process shows higher electrical resistance or lower current utilization when operated at above LCD. It also can give rise to problems such as water dissociation or salt precipitation. It is necessary, therefore, to determine the LCD to prevent problems and operate the electrodialyzer successfully [32].

The limiting current can be determined experimentally by plotting the electrical resistance across the membrane stack (E $I^{-1}$) or the pH value in the dilute cell as a function of the reciprocal electric current ($I^{-1}$). This is called a Cowan-Brown plot after its original developers [33, 34].

Usually, the limiting current depends on membrane and solution properties as well as on the electrodialysis stack construction and various operational parameters such as the flow velocity (flow rate) of the

dilute solution. The set of primary tests was done to determine the limiting current density for the operating conditions to be adopted in this study.

**2.4.3.4. Specific power consumptions.** Specific power consumption (SPC) can be described as the energy needed to treat unit volume of solution. SPC was calculated using the following equation [23]:

$$SPC = \frac{E\int_0^t I(t)dt}{V},$$

where $E$ is the applied potential, $I$ the current, $V$ the dilute stream volume and $t$ is the time.

The SPC values were calculated for each experimental condition and 200 mg $NO_3^-$ $L^{-1}$ removed.

## 3. RESULTS AND DISCUSSIONS

### *3.1. Determination of the Limiting Current ($I_{lim}$)*

In this study the limiting current ($I_{lim}$) was determined by measuring the potential and the cell resistance as a function of the applied current. Figures 3a and 3b shows the curves illustrating the determination of the limiting current from the experimental result obtained with a 0.05 M NaCl solution and a linear feed flow velocity of 0.104 m $s^{-1}$ (15 L $h^{-1}$ flow rate). In the relationship between the dilute pH and the current in Fig. 3a, the limiting current was determined where the slope was changed due to water dissociation on the surface of ion exchange membranes [33, 34]. In addition, the limiting current was determined from the graph showing the cell resistance versus the reciprocal of the current (Fig. 3b).

NaCl Solutions with different concentrations were used to determine these values at different flow rates. The obtained results were summarized in Table 3.

The applied current in all experiment was fixed from the beginning to a value below the limiting current ($I = 0.8I_{lim}$) [35].

### *3.2. Denitrification of Synthetic Solution*

**3.2.1. Effect of pH of the feed solution.** Effect of pH of the feed solution on the removal of nitrate, demineralization rate and specific power consumption are showed in Figs. 4a, 4b and 4c.

The removal of $NO_3^-$ was independent of pH, which is due to the pH independence of $NO_3^-$ speciation [21].

**3.2.2. Effect of feed flow rate.** The operation was carried out using different feed flow rates (5, 15, 30 L $h^{-1}$) and with a nitrate solution of 250 mg $L^{-1}$ and 1.5 g $L^{-1}$ as initial feed concentration.

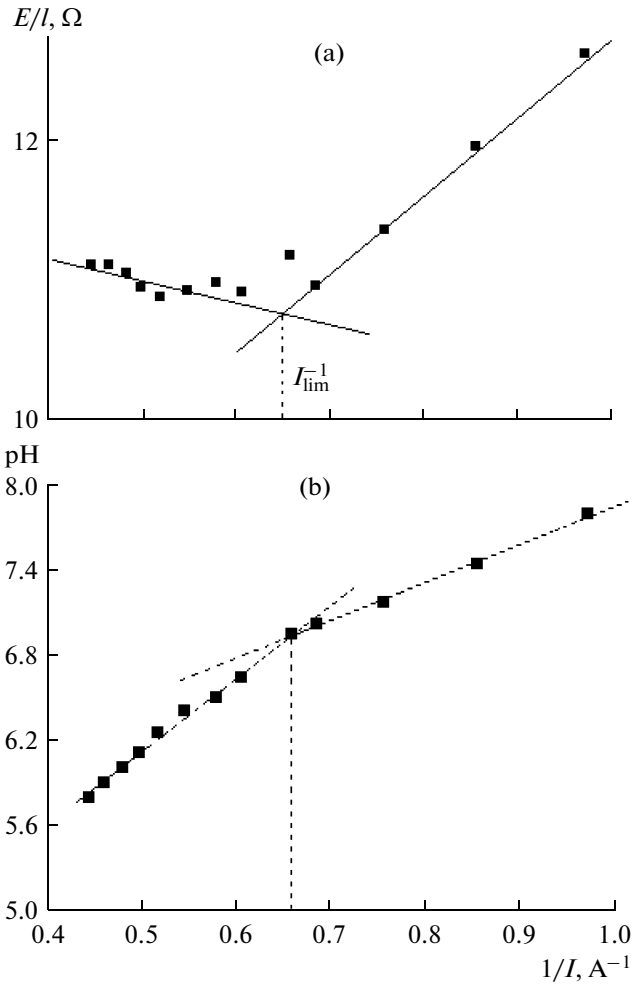


**Fig. 3.** (a) Variation of cell resistance versus the reciprocal of applied current (b) Variation of pH in the dilute compartment versus the reciprocal of applied current.

As seen in Figs. 5a and 5b, flow rate have a significant effect on nitrate removal only in the beginning of the experiment (before 20 min) in the range of flow rates studied. The initial flux of nitrate is higher in the beginning of experiment mainly for low rates. It

**Table 3.** Limiting current values as function of flow rate and feed concentration

| Flow rate, L $h^{-1}$ | Feed solution concentration, g $L^{-1}$ | | | |
|---|---|---|---|---|
| | 0.5 | 1 | 1.5 | 2.5 |
| 5 | 0.2 | 0.4 | 0.82 | 1.16 |
| 15 | 0.34 | 0.62 | 0.98 | 1.52 |
| 25 | 0.46 | 0.86 | 1.15 | 1.96 |
| 30 | 0.52 | 1 | 1.26 | 2.2 |

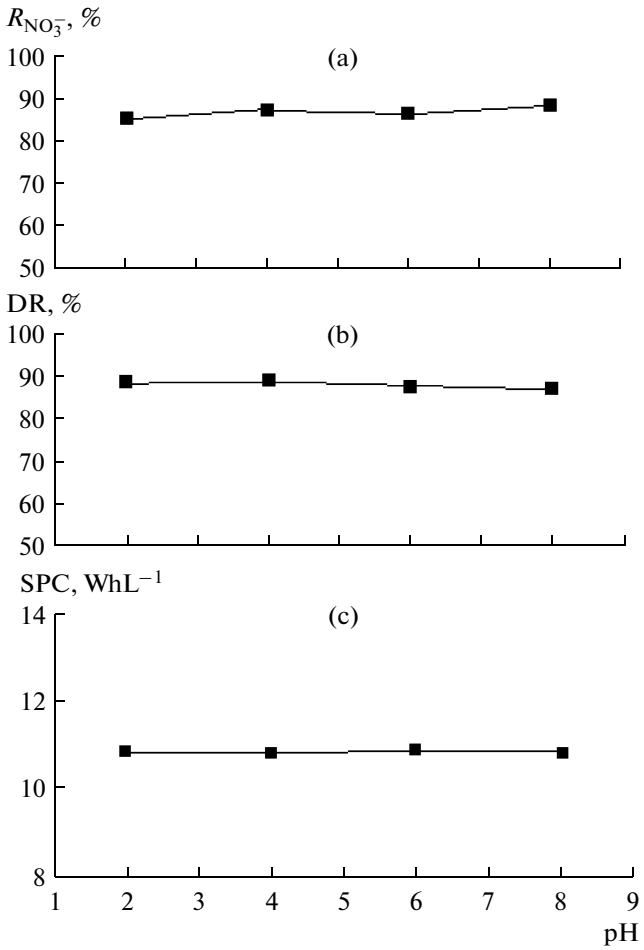


**Fig. 4.** pH of feed solution effect (a) on the removal of nitrate, (b) on the DR and (c) on the SPC ($NO_3^-$ 250 mg $L^{-1}$, applied current 1.72 A, initial feed solution 2.5 g $L^{-1}$ and flow rate 30 L $h^{-1}$).

decreases quickly and become constant for all flow rates.

The nitrate ions transferred from the diluted to concentrated compartments are higher in the beginning of experiment because the amount of nitrate contained in the initial compartments is at higher level and high variations can be calculated. For low flow rate these ions still longer time in the dilute compartments and can be transferred from one to another compartments. After short experiment time the concentration of nitrate in dilute is reduced and the variations during time becomes low and constant. The opposite observations were obtained in the removal rates as function of time [29].

In the other hand, as depicted in Fig. 5c, the specific power consumption depends also on this parameter. The SPC is lower for low flow rate. This can be explained by two propositions. Effectively the SPC depends mainly on two parameters: the applied current and the time of experiment. Firstly the applied current (the limiting current) is depending on the flow rate as shown in Table 3. It is lower for low flow rate. Secondly the experiment time to obtain the same results (removal of 200 mg $L^{-1}$ of $NO_3^-$) is increasing when the flow rates increases.

It was not possible to increase the flow rate above 30 L $h^{-1}$ since the maximum capacity of the pumps in the present system is defined as 30 L $h^{-1}$.

**3.2.3. Effect of initial feed concentration.** The effect of initial feed concentration on the removal of nitrate was investigated using aqueous solutions at various concentrations of NaCl salt (0.5, 1, 1.5 and 2.5 g $L^{-1}$) and fixed nitrate solution of 250 mg $L^{-1}$.

As shown in Figs. 6a and 6b, the initial salt concentration has a significant effect on the nitrate removal. The most important observation is that total process time increased with increasing initial concentration in the feed. Consequently the specific power consumption is closely depending on it as seen in Fig. 6c.

These results can be explained by the increase of number of ions in solutions when the concentration of salts increases. As a result a competitive transfer can

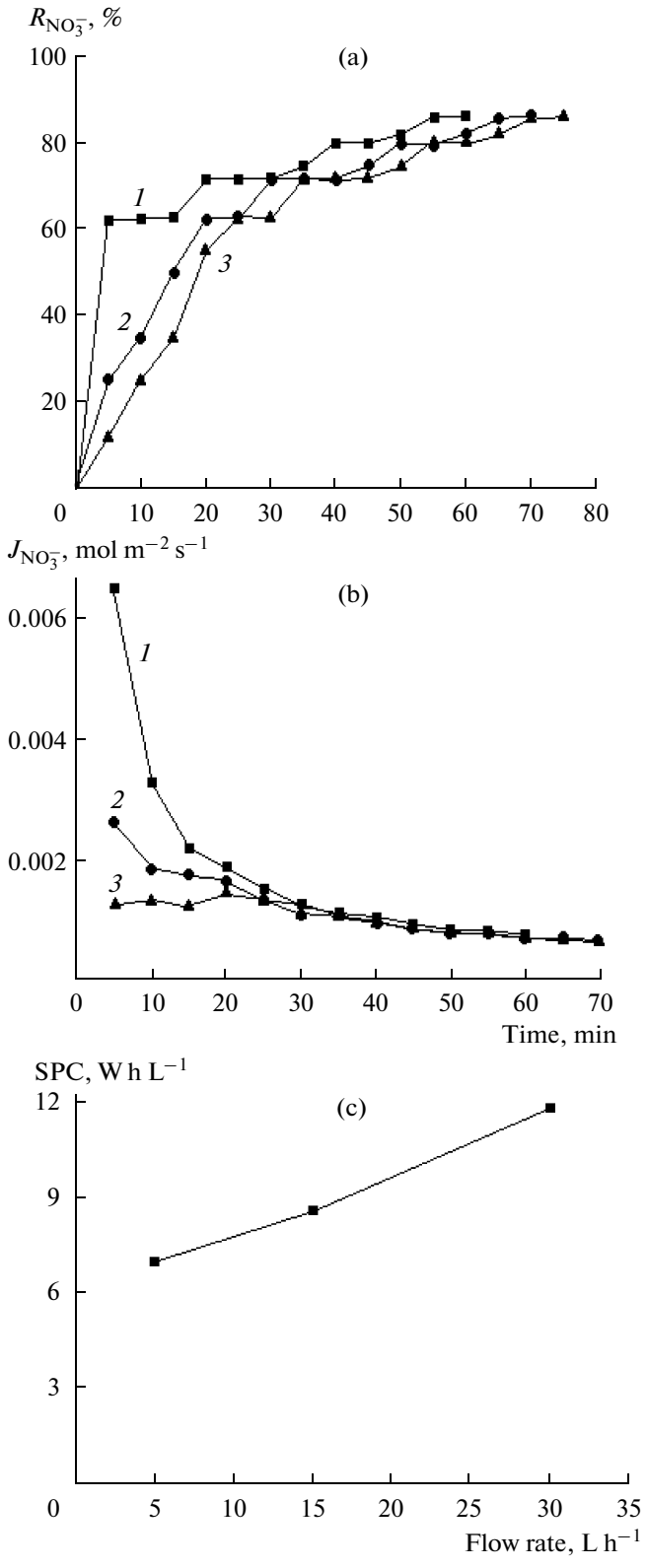


**Fig. 5.** Effect of feed flow rate (a) on the removal of nitrate, (b) on the nitrate flux and (c) on the SPC ($NO_3^-$ 250 mg L$^{-1}$, initial feed solution 1.5 g L$^{-1}$).

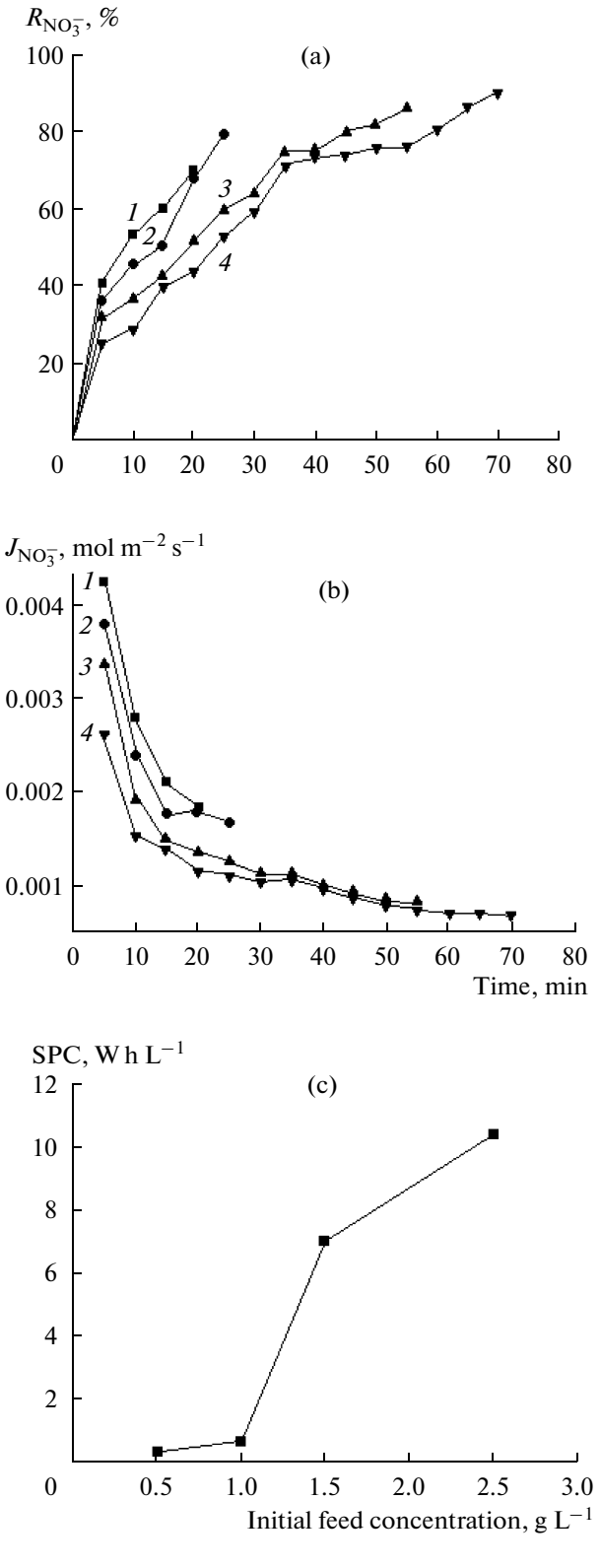


**Fig. 6.** Effect of initial feed concentration (a) on the removal of nitrate, (b) on the nitrate flux and (c) on the SPC ($NO_3^-$ 250 mg L$^{-1}$, flow rate 5 L h$^{-1}$).

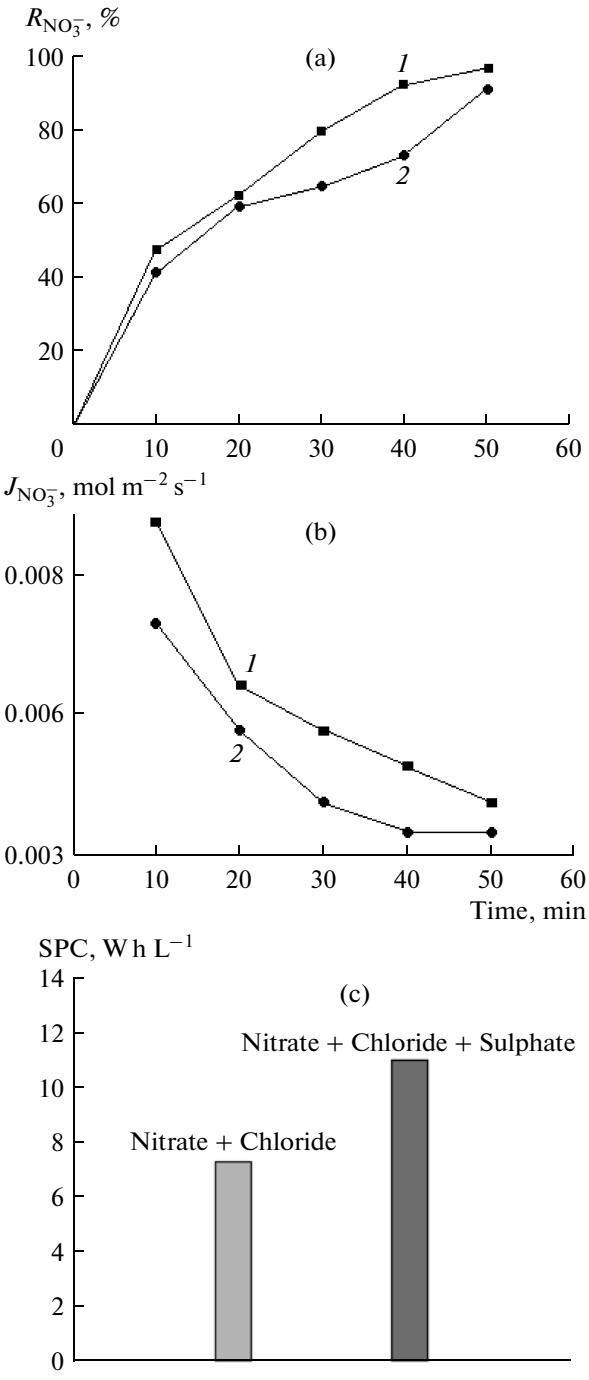


**Fig. 7.** Effect of accompanying ions (a) on the removal of nitrate, (b) on the nitrate flux and (c) on the SPC ($NO_3^-$ 250 mg L$^{-1}$, applied current 1.72 A, initial feed concentration 3 g L$^{-1}$ and flow rate 30 L h$^{-1}$).

appear between nitrate ions and other ions (chloride ions in this case).

It was not possible to increase the concentration of initial feed solution above 3 g L$^{-1}$ since an electrode overheating appeared in the present system as a result of the increase of cell conductivity.

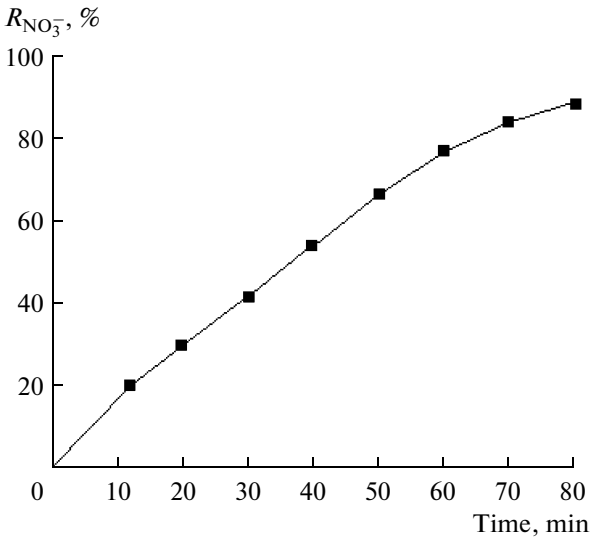


**Fig. 8.** Removal of nitrate from real water sample by electrodialysis (nitrate concentration of real water: 225 mg L$^{-1}$; flow rate: 25 L h$^{-1}$, applied current: 1.92 A).

**3.2.4. Effect of coexisting ions.** In the presence of chloride and sulphate ions, removal of nitrate by electrodialysis was investigated. The experiments were conducted with $NO_3^-$ (250 mg L$^{-1}$ solution) paired only with chloride and mixtures containing both chloride and sulphate ions.

It was obtained that the competition between nitrate and chloride ions was certain (Figs. 6a and 6b). The increase of chloride ions on the feed solution leads to the decrease of the removal rate and flux of nitrate ions. These phenomena are also clearly observed in the presence of sulphate ions. Effectively and as depicted in Figs. 7a and 7b nitrate ions flux and retention rate decreases more in these conditions.

As shown in Fig. 7c, the specific power consumption increases more and more in the presence of the other species. This is due mainly to the augmentation of the total experiment time.

### *3.3. Application of Denitrification of the Real Water Sample*

Finally, the application of electrodialysis was performed on the real brackish water. As seen in Table 4, denitrification of real water was achieved with nitrate concentration (25.5 mg L$^{-1}$) lower than the maximum recommended by WHO (50 mg L$^{-1}$) despite to the presence of chloride and sulphate ions in sample. The concentrations of different species in the obtained treated water are below the amounts recommended by WHO for drinking water.

**Table 4.** Composition of the treated brackish water

| Physico-chemistry parameter | Treated water | Recommendations of WHO [4] |
|---|---|---|
| Conductivity at 25°C, μS $cm^{-1}$ | 0.808 | – |
| pH | 5.1 | 6.5–8.5 |
| $F^-$, mg $L^{-1}$ | 0.22 | 1.5 |
| $Cl^-$, mg $L^{-1}$ | 182 | 250 |
| $HCO_3^-$, mg $L^{-1}$ | 202 | – |
| $NO_3^-$, mg $L^{-1}$ | **25.5** | 50 |
| $SO_4^{2-}$, mg $L^{-1}$ | 24.67 | 400 |
| $Na^+$, mg $L^{-1}$ | 49.92 | 250 |
| $K^+$, mg $L^{-1}$ | 24.23 | – |
| $Ca^{2+}$, mg $L^{-1}$ | 14.03 | – |
| $Mg^{2+}$, mg $L^{-1}$ | 12.72 | – |
| TDS, mg $L^{-1}$ | 350 | 500 |

In other words, nitrate removal from real water sample was 88% at the end of 80 min of electrodialysis (Fig. 8) and with 13.2 W h $L^{-1}$ as specific power consumption.

## CONCLUSIONS

The results from the presented study can be concluded as follows:

—The removal of $NO_3^-$ was independent of pH.

—The feed flow rate has a significant effect on the denitrification efficiency and mainly on the specific power consumption. The decrease of this parameter induces a decrease on the energy needed to perform required operation.

—The initial salt concentration of feed solution has a significant effect on the nitrate removal. An increase of this concentration leads to the increase of total process time and consequently the augmentation of the specific power consumption to obtain required denitrification efficiency.

—The removal of nitrate decreased in the presence of chloride and sulphate ions in the feed phase. In other words, the transport of the nitrate ions is more effective in the absence of co-existent anions.

As a result of the application of electrodialysis on the real water sample, nitrate concentration could be reduced from 225 to 25.5 mg $L^{-1}$ (88% removal), which was lower than WHO standard (50 mg $L^{-1}$). Moreover the concentrations of different species in the obtained treated water are below the amounts recommended by WHO for drinking water.

## REFERENCES


1. Karime, M., Bouguecha, S. and Hamrouni, B., RO Membrane Autopsy of Zarzis Brackish Water Desalination Plant, *Desalination,* 2008, vol. 220, pp. 258–266.
2. Walha, K., Amar R. Ben, Firdaous, L., Quéméneur, F., and Jaouen, P., Brackish Groundwater Treatment by Nano-filtration, Reverse Osmosis and Electrodialysis in Tunisia: Performance and Cost Comparison, *Desalination*, 2007, vol. 207, pp. 95–106.
3. Laajimi, A., Nasr, J.B., and Ferchichi, M., Managing Nitrate Pollution in a Tunisian Irrigated Area: A Multi-Criteria Analysis Approach, in *12th EAAE Congress: People, Food and Environments: Global Trends and European Strategies, 2008*, Belgium, Ghent, http://purl.umn.edu/44186.
4. World Health Organization, Guidelines for Drinking-Water Quality: Incorporating 1st and 2nd Addenda, vol. 1, Recommendations, 2008, pp. 375–492.
5. Della Rocca, C., Belgiorno, V., and Meriç, S., Overview of in-situ Applicable Nitrate Removal Processes, *Desalination*, 2007, vol. 204, pp. 46–62.
6. Shrimali, M. and Singh, K.P., New Methods of Nitrate Removal from Water, *Environ. Pollut.*, 2001, vol. 112, pp. 351–359.
7. Ghafari, S., Hasan, M. and Aroua, M.K., Bio-Electrochemical Removal of Nitrate from Water and Wastewater-A Review, *Bioresour. Technol.*, 2008, vol. 99, pp. 3965–3974.
8. Li, M., Feng, Ch., Zhanga, Z., Lei, X., Chen, R., Yang, Y., and Sugiura, N., Simultaneous Reduction of Nitrate and Oxidation of By-Products Using Electrochemical Method, *J. Hazard. Mater.*, 2009, vol. 171, pp. 724–730.
9. Xia, S., Zhang, Y., and Zhong, F., A Continuous Stirred Hydrogen-Based Polyvinyl Chloride Membrane Biofilm Reactor for the Treatment of Nitrate Contaminated Drinking Water, *Bioresour. Technol.*, 2009, vol. 100, pp. 6223–6228.
10. Zhang, Y., Zhong, F., Xia, S., Wang, X., and Li, J., Autohydrogenotrophic Denitrification of Drinking Water Using a Polyvinyl Chloride Hollow Fiber Membrane Biofilm Reactor, *J. Hazard. Mater.*, 2009, vol. 170, pp. 203–209.
11. Velizarov, S., Crespo, J.G., and Reis, M.A., Removal of Inorganic Anions from Drinking Water Supplies by Membrane Bio/Processes, *Rev. Environ. Sci. Biotechnol.*, 2004, vol. 3, pp. 361–380.
12. Wiśniewski, J., Różańska, A. and Winnicki, T., Removal of Troublesome Anions from Water by Means of Donnan Dialysis, *Desalination*, 2005, vol. 182, pp. 339–346.
13. Park, W., Nam, Y-K., Lee, M-J, and Kim, T-H., Simultaneous Nitrification and Denitrification in a CEM (Cation Exchange Membrane)-Bounded Two Chamber System, *Water Res.*, 2009, vol. 43, pp. 3820–3826.
14. Wisniewski, C., Persin, F., Cherif, T., Sandeaux, R., Grasmick, A., and Gavach, C., Denitrification of Drinking Water by the Association of an Electrodialysis Process and a Membrane Bioreactor: Feasibility and Application, *Desalination*, 2001, vol. 139, pp. 199–205.

15. Annouar, S., Mountadaff, M., Soufiane, A., Elmidaoui, A., Menkouehi Sahli, M.A., and Kahlaoui, M., Denitrifica-tion of Underground Water by Chemical Adsorption and by Electrodialysis, *Desalination*, 2004, vol. 168, p. 185.
16. Menkouchi Sahli, M.A., Annouar, S., Mountadar, M., Soufiane, A., and Elmidaoui, A., Nitrate Removal of Brackish Underground Water by Chemical Adsorption and by Electrodialysis, *Desalination*, 2008, vol. 227, pp. 327–333.
17. El Midaoui, A., Elhannouni, F., Taky, M., Chay, L., Menkouchi Sahli, M.A., Echihabi, L., and Hafsi, M., Optimization of Nitrate Removal Operation from Ground Water by Electrodialysis, *Sep. Purif. Technol.*, 2002, vol. 29, pp. 235–244.
18. Menkouchi Sahli, M.A., Tahaikt, M., Achary, I., Taky, M., Elhanouni, F., Hafsi, M., Elmghari, M., and Elmidaoui, A., Technical Optimization of Nitrate Removal for Groundwater by ED Using a Pilot Plant, *Desalination*, 2006, vol. 189, pp. 200–208.
19. Kesore, K., Janowski, F., and Shaposhnik, V.A., Highly Effective Electrodialysis for Selective Elimination of Nitrates from Drinking Water, *J. Membr. Sci.*, 1997, vol. 127, pp. 17–24.
20. Ergun, E., Tor, A., Cengeloglu, Y., and Kocak, I., Electrodialytic Removal of Fluoride from Water: Effects of Process Parameters and Accompanying Anions, *Sep. Purif. Technol.*, 2008, vol. 64, pp. 147–153.
21. Banasiak, L.J. and Schäfer, A.I., Removal of Boron, Fluoride and Nitrate by Electrodialysis in the Presence of Organic Matter, *J. Membr. Sci.*, 2009, vol. 334, pp. 101–109.
22. Sadrzadeh, M., Razmi, A., and Mohammadi, T., Separation of Different Ions from Wastewater at Various Operating Conditions Using Electrodialysis, *Sep. Purif. Technol.*, 2007, vol. 54, pp. 147–156.
23. Kabay, N., Arar, O., Samatya, S., Yuksel, U., and Yuksel, M., Separation of Fluoride from Aqueous Solution by Electrodialysis: Effect of Process Parameters and Other Ionic Species, *J. Hazard. Mater.*, 2008, vol. 153, pp. 107–113.
24. Ortiz, J.M., Exposito, E., Gallud, F., Garcia-Garcia, V., Montiel, V. and Aldaz, A., Desalination of Underground Brackish Waters Using an Electrodialysis System Powered Directly by Photovoltaic Energy, *Sol. Energy Mater. Sol. Cells*, 2008, vol. 92, pp. 1677–1688.
25. Shaposhnik, V.A., Zubets, N.N., Strygina, I.P., and Mill, B.E., High Demineralization of Drinking Water by Elecrodialysis without Scaling on the Membranes, *Desalination*, 2002, vol. 145, pp. 329–332.
26. Banasiak, L.J., Kruttschnitt, T.W., and Schäfer, A.I., Desalination Using Electrodialysis as a Function of Voltage and Salt Concentration, *Desalination*, 2007, vol. 205, pp. 38–46.
27. Casademont, C., Farias, M.A., Pourcelly, G., and Bazinet, L., Impact of Electrodialytic Parameters on Cation Migration Kinetics and Fouling Nature of Ion-Exchange Membranes during Treatment of solutions with Different Magnesium/Calcium Ratios, *J. Membr. Sci.*, 2008, vol. 325, pp. 570–579.
28. Wang, Q., Ying, T., Jiang, T., Yang, D., and Muzammil Jahangir, M., Demineralization of Soybean Oligosaccharides Extract from Sweet Slurry by Conventional Electrodialysis, *J. Food Eng.*, 2009, vol. 95, pp. 410–415.
29. Lee, H.J., Sarfert, F., and Strathmann, H., Designing of an Electrodialysis Desalination Plant, *Desalination*, 2002, vol. 142, pp. 267–286.
30. Vasil'eva, V.I., Grigorchuk, O.V., and Shaposhnik, V.A., Limiting Current Density in Electromembrane Systems with Weak Electrolytes, *Desalination*, 2006, vol. 192, pp. 401–407.
31. Tanaka, Y., Current Density Distribution, Limiting Current Density and Saturation Current Density in an Ion-Exchange Membrane Electrodialyzer, *J. Membr. Sci.*, 2002, vol. 210, pp. 65–75.
32. Baker, R.W., *Membrane Technology and Applications* (Second Edition), England: John Wiley & Sons, Ltd., 2004.
33. Lee, H.J., Strathmann, H., and Moon, S.H., Determination of the Limiting Current Density in Electrodialysis Desalination as an Empirical Function of Linear Velocity, *Desalination*, 2006, vol. 190, pp. 43–50.
34. Balmann, H.R.-d. and Casademont, E., *Électrodialyse, Techniqués de l'Ingénieur*, 2006, J 2840.

ISSN 1068-3755, Surface Engineering and Applied Electrochemistry, 2010, Vol. 46, No. 3, pp. 263–265. © Allerton Press, Inc., 2010.
Original Russian Text © A.R. Rizun, V.A. Posdeev, Yu.V. Golen', 2010, published in Elektronnaya Obrabotka Materialov, 2010, No. 3, pp. 78–81.

## EQUIPMENT AND INSTALLATIONS

# One-Shot Electrode Systems for High-Voltage Electrochemical Destruction of Natural and Artificial Lumps

**A. R. Rizun, V. A. Posdeev, and Yu. V. Golen'**

*Institute of Pulse Processes and Technologies, National Academy of Sciences of Ukraine*
*pr. Oktyabrskii 43a, Nikolaev, 327018 Ukraine*
*e-mail: dpcd@iipt.com.ua*

Received December 30, 2009

**Abstract**—Thermophysical phenomena are revealed in blast-hole electrochemical explosion processes with the use of one-shot electrode systems, which have an advantage over expensive multiple use electrode systems.

**DOI:** 10.3103/S1068375510030129

## INTRODUCTION

The topicality of the process under consideration is due to the elimination of expensive multiple-use electric-discharge systems from processes of the blast-hole electric-discharge destruction of natural and artificial lumps. It was found in practice that the quantity of the discharges produced by multiple-use electrode systems does not cover their production expenses or their replacement.

There is a proposal for the substitution of one-shot electric-discharge systems for multiple-use electric-discharge systems because the cost of the former is significantly lower at the same quantity of blasting [1].

## CHARACTERISTICS OF THE TECHNOLOGY PROPOSED

A high-voltage electrochemical explosion (HVEE) is a complex of physicochemical phenomena proceeding in the presence of substances or compositions in the area of a discharge channel that are capable of exothermal chemical transformations under the conditions of high temperature and pressure that arise within the discharge channel. The released energy under such transformations is summed with the electric energy that accumulates on the plates of the capacitors. As a result of such summation, the destruction energy increases by several times without an increase in the equipment size, including the number of capacitors [2].

## THERMOPHYSICAL PROCESSES WITHIN BLAST-HOLE AREAS

Figure 1 presents a schematic of the electric discharge in a blast hole with a one-shot discharge system (ODS) in the presence of an exothermal mixture (EM). In the case presented, the electric discharge functions in two ways. It is firstly a source of formation on the primary wave of pressure and, secondly, an electric fuse to ignite the exothermal mixture [3].

The whole process can be separated into two steps. In the first step, the breakdown occurs and the discharge channel is formed, which develops owing to the evolution of the electric energy in the channel. During the second step, the warming-up of the exothermal mixture is observed. The ignition and combustion of the exothermal mixture begin after heating it close to the channel to the ignition temperature. The stable combustion of the mixture is possible under the equality of the heat input to the layers and the output from it. This condition is determined by the solution of a

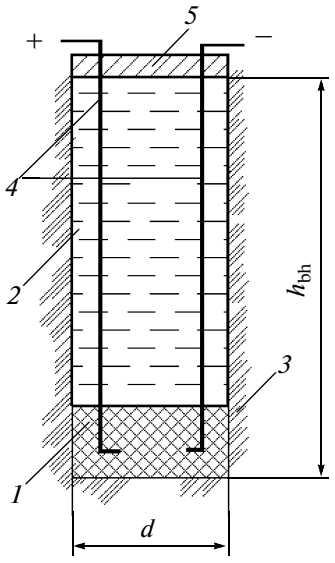


**Fig. 1.** Schematic of the HVEE realization for a one-shot discharge system: (*1*) exothermal composition, (*2*) water, (*3*) soil, (*4*) high-voltage electrodes, (*5*) cover.

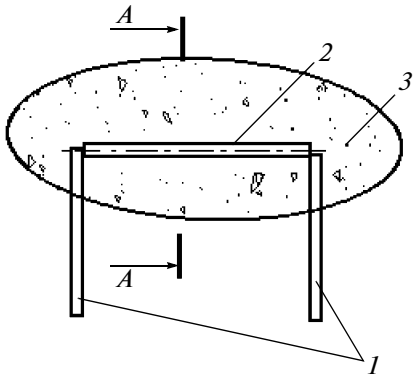


**Fig. 2.** Schematic of the electric discharge within the exothermal medium: (*1*) high-voltage electrodes, (*2*) discharge channel, (*3*) exothermal medium.

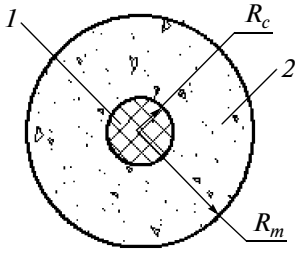


**Fig. 3.** Chart of the *A*–*A* section: (*1*) plasma of the discharge channel with the radius $R_c(t)$, (*2*) exothermal medium; $R_m$ is the general radius.

thermophysical problem. In the common three-dimensional case and with the complex geometry of the volume of the exothermal mixture, the problem up to the present day has not been considered. In the present case, we used a model of the discharge with cylindrical symmetry, where the channel length $l$ significantly exceeded its radius $R$, and the transversal sizes of the mixture's volume were also significantly more than the radius of the discharge channel.

To consider the total thermophysical problem, let us use the method of plane sections [4] (Fig. 2, 3).

Further, let us use the approach presented in [5]. The heat conduction is described by the main set of heat conductivity equations:

$$\rho_1 c_1 \frac{dT_1}{dt} = \frac{d}{dr}\left(\lambda_1 \frac{dT_1}{dr}\right) + \frac{\lambda_1}{r}\frac{dT_1}{dr} + w_1; \quad (1)$$

$$(0 < r < R_k(t))$$

$$\rho_2 c_2 \frac{dT_2}{dt} = \frac{d}{dr}\left(\lambda_2 \frac{dT_2}{dr}\right) + \frac{\lambda_2}{r}\frac{dT_2}{dr} + w_2; \quad (2)$$

$$(R_k < r < R_c)$$

with the initial conditions

$$\left.\begin{aligned} T_1(r) &= T_0 \quad \text{at} \quad t = 0 \\ T_2(r) &= T_0 \quad \text{at} \quad t = 0 \end{aligned}\right\} \quad (3)$$

and the boundary conditions

$$\frac{dT_1}{dr} = 0 \quad \text{at} \quad r = 0, \quad (4)$$

$$\lambda_1 \frac{dT_1}{dr}\bigg|_{r=R_k} = \lambda_2 \frac{dT_2}{dr}\bigg|_{r=R_k}, \quad (5)$$

$$T_1 = T_2 \quad \text{at} \quad r = R_k(t), \quad (6)$$

$$T_2 = T_0 \quad \text{at} \quad r = R_c, \quad (7)$$

where $\rho_i$ ($i = 1, 2$) is the matter density, kg/m$^3$; $c_i$ ($i = 1, 2$) is the heat capacity, J/K; $T_i$ ($i = 1, 2$) is the matter temperature, K; $\lambda_i$ ($i = 1, 2$) is the heat-conductivity coefficient, W/(m K); and $w_i$ ($i = 1, 2$) is the density of the heat sources, W/m$^2$.

In the given expressions, the index 1 is related to the channel, and the index 2, to the surrounding exothermal medium.

The power density within the channel is

$$w_1 = \frac{I^2(t)}{\sigma(T_1)}, \quad (8)$$

where $w_1$ is the power density within the channel, W/m$^2$; $I(t)$ is the current density within the channel, A/m$^2$; and $\sigma(T_1)$ is the conductivity of the channel medium (plasma), S/m.

In turn,

$$I(t) = \frac{\dot{I}(t)}{\pi R_k^2(t)}, \quad (9)$$

where $I(t)$ is the channel current, A.

We assume that the burning of the exothermal medium during the initial step is insignificant, namely, $w_2 \ll w_1$. Therefore, we assume that, before the moment of the mixture's ignition (the beginning of the combustion), $w_2 = 0$. The moment $t_3$ of the mixture's ignition according [5], we determine by the following set of equations:

$$\begin{aligned} q(t_3) &= k\int_R^{R_c} w_2(T_2(r, t_3))2\pi r dr; \\ q(t_3) &= -\lambda_2 \frac{dT_2(R_k, t_3)}{dr}. \end{aligned} \quad (10)$$

Set (10) compares the heat emission from the external source (the discharge channel) in the combustion reaction area with the exothermal heat. The

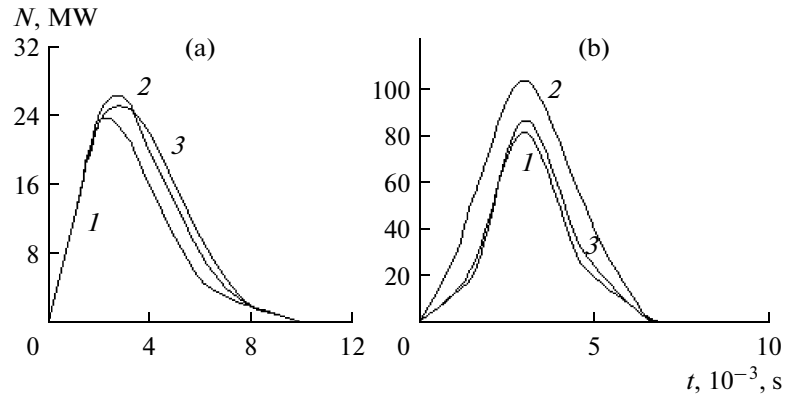


**Fig. 4.** Time dependence of the evolved power computed by (1)–(11). $U_0$, kV; (a) 10, (b) 20; $L = 3 \times 10^{-6}$ H; $C = 3 \times 10^{-6}$ F; the exothermal mixture, kg: (*1*) 0.0003, (*2*) 0.0005, (*3*) 0.0007.

moment of the equality of the heat fluxes gives the time of the mixture's ignition. It is suggested that

$$w_2(T) = \sum_{k=1}^{k} A_k (T_2 - T_0)^{\alpha_k}, \qquad (11)$$

where $A_k$ and $\alpha_k$ are some constants.

To simplify solving problem (1)–(11), let us use the recommendations in [2, 3], where the following approximate equality is assumed:

$$t_s \sim t_0, \qquad (12)$$

where $t_0$ is the duration of the first half-cycle of the oscillations of the discharge current, s.

Figure 4 gives the time dependence of the electrical power's evolution, which is obtained in the computation way. As is evident from the figure, the time of the first half-cycle weakly depends on both the initial voltage on the capacitor plates and the quantity of the exothermal mixture.

Thus, $t_3 = t_0$ is considered the time of the beginning of the stable combustion of the exothermal mixture.

## CONCLUSIONS

The time of the first half-cycle plays a decisive role in achieving the combustion efficiency of the exothermal mixture and the maximum evolution of energy during its combustion [6].

The evolved power in the first half-cycle should be sufficient for the maximum combustion efficiency of the exothermal mixture. In practice, the value of $t_3$ is formed owing to the capacity $C$ at the constant value of the equipment induction.

The use of one-shot systems and exothermal mixtures significantly decreases the primary cost of electric-discharge destruction, decreases the equipment size, and increases the equipment's mobility.

## REFERENCES

1. Rizun, A.R., Golen', Yu.V., Mushtatnyi, G.P., et al., Ukr. Patent 26101 (u200613738), 2006.
2. Vovchenko, A.I. and Posokhov, A.A., *Upravlyaemye elektrovzryvnye protsessy preobrazovaniya energii v kondensirovannykh sredakh* (Controlled Electroblasting Processes of Energy Transformation in Condensed Media), Kiev: Naukova Dumka, 1992, p. 168.
3. Vovchenko, A.I., Kucherenko, V.V., and Shamko, V.V., *Zh. Prikl. Mekh. Tekh. Fiz.*, 1978, no. 5, p. 58.
4. Pozdeev, V.A. and Ishchenko, Zh.N., Approximation of Law for Energy Input on Electrical Discharge and Wire Explosion, in *Electrorazryadnye protsessy: teoriya, eksperiment, praktika: Sb. Nauchn. Tr.* (Electrical-Discharge Processes: Theory, Experiment, and Practice: Collection of Proc.), Kiev: Naukova Dumka, 1984, p. 58.
5. Kupershtokh, A.L. and Luk'yanchenov, L.A., Determining Effective Kinetics of Heat Generation on Ignition of Heterogeneous Condensed Matters in *Mekhanika bystroprotekayushchikh protsessov: Sb. Nauchn. Tr. SO AN SSSR. Inst. gidrodinamiki. Moskva* (Mechanics of Fast Processes: Collection of Proc. of Siberian Branch of Academy of Sciences of the USSR. Inst. of Hydrodynamics. Moscow, 1983, vol. 62, p. 68.
6. Rizun, A.R., Golen', Yu.V., Denisyuk, T.D., et al., *Nauka Inovatsii*, 2007, no. 3, p. 50.

ISSN 1068-3755, Surface Engineering and Applied Electrochemistry, 2010, Vol. 46, No. 3, pp. 266–270. © Allerton Press, Inc., 2010.

EQUIPMENT AND INSTALLATIONS

# Modeling of Laser Cladding with Diode Laser Robotized System[1]

**Jianhua Yao[a], V. S. Kovalenko[b], Qunli Zhang[a], Anyakin Mykola[b], Xiaodong Hu[a], and Weifu Wang[a]**

[a] *Research Center of Laser Processing Technology and Engineering, Zhejiang University of Technology, Hangzhou, P.R. China*
*e-mail: laser@zjut.edu.cn*

[b] *Laser Technology Research Institute, National Technical University of Ukraine "KPI", Pobeda avenue 37, Kyiv, 03056, Ukraine*
*e-mail: kovinvst@ntu-kpi.kiev.ua*

Received December 30, 2009

**Abstract**—The choice of proper working conditions is a problem for any processing. But for laser processing this procedure is much more serious. The final results of the processing are usually influenced by over 100 factors. So the best way to choose more cheaply and fast the working conditions is to use the processing simulation. Different tactics of this procedure is discussed and the statistical modeling is accepted. The actual model for laser cladding is developed based on the experimental results of steel cladding with diode laser robotized system. This model can be used to find the optimal working conditions for laser processing in practical use.

**DOI:** 10.3103/S1068375510030130

## 1. INTRODUCTION

In laser processing to choose the working conditions may appear not very easy task. Unlike at any other conventional processing the final results at laser processing may be influenced by more than 100 different factors: (1) laser beam parameters (its wavelength, mode, level of focusing/defocusing, power/energy distribution in the focusing spot, pulse duration and frequency for pulsed irradiation, etc.); (2) material properties (elements content, surface optical properties, thermo-physical properties, component dimensions, etc.); (3) conditions of laser irradiation (speed of irradiation, overlapping coefficients, the amount and type of irradiated spots distribution on the surface of the component, angle of surface irradiation, etc.); (4) additional conditions (beam scanning, use of additional energy—hybrid processing, application of surface coatings, etc.).

As a final goal of processing the large variety of factors may be considered as well: dimensions, surface roughness, micro hardness, size of HAZ (Heat Affected Zone), distribution of chemical elements, wear resistance, strength, etc.

Considering the complexity of laser processing, the best way to its study may be the use of processing simulation which gives the possibility to reduce the time, labor and cost of research and to predict the final result of processing. For the moment there had been developed the variety of different tactics of different process modeling [1–6].

The most efficient models are considered as follows:

—physical simulation (model);

—numerical simulation;

—statistical simulation.

**Physical simulation (model)** is based on application of fundamental physical laws. Because such laws may not be known for some unusual conditions of laser interaction with matter, the results of such simulation may be valid only for limited known conditions. This makes it impossible to use such tactics for practical purposes.

**Numerical simulation** is based as well on fundamental physical laws but model may be vadequate only when all dependencies are known (which is unrealistic) in real conditions. So such simulation is very difficult to use for practical purposes.

As opposite to previous tactics, the **statistical simulation** is based on gained real experimental data. Thus it is very simple for realization. Its main advantages are minimum experiments to create the model and possibility for wide practical use with given ahead statistical mistake. As disadvantages the following may be named: simulation is valid only within the limited experimental space and it doesn't disclose the physical mechanism of the processing.

## 2. DEVELOPMENT OF THE MODEL BASED ON STATISTICAL SIMULATION

At statistical simulation the studied process is considered as a "black box" which is influenced by the number of independent variables (working conditions) and affects the final results (dependent variables) of processing (Fig. 1).

[1] The article is published in the original.

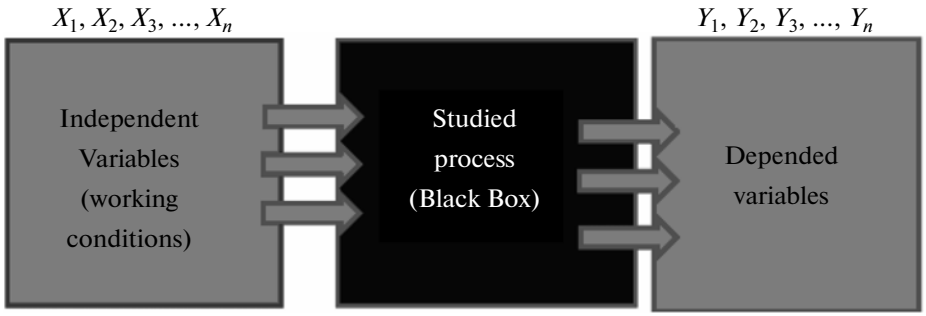


**Fig. 1.** Scheme of the relations between studied process and different variables.

In general it may be described mathematically as following regression equation:

$$y = b_0 + \sum_{i=1}^{i=k} b_i x_i + \sum_{i \neq j=1}^{i \neq j=k} b_{ij} x_i x_j + \sum_{ii=1}^{ii=k} b_{ii} x_{ii}^2$$

where: $k$—number of technological factors; $b_0$, $b_i$, $b_{ij}$, $b_{ii}$—regression equation coefficients; $i, j$—indexes.

As independent variables (working conditions) the following factors are considered:

—properties of laser beam;

—properties of material to be processed;

—additional conditions.

As final result of the processing the different dependent parameters may be considered:

—component Properties (wear resistance, strength), $Y_1$, $Y_2$, ..., $Y_N$;

—surface roughness ($Y_i$), Dimensions of HAZ ($Y_j$), Size of tempered zone ($Y_1$) Chemical elements distribution ($Y_m$) and etc.

For modeling realization depending on different consideration (amount of experiments, their duration and cost, expected accuracy, etc.), different techniques (plans of experiments) may be proposed. Among them we will name only few:

(1) composite plan—**26**–**42** experiments;

(2) plan of experiments (Hartly)—**30** experiments;

(3) super full plan of experiments (Rechtchafner), (Hartly)—**21** experiments;

(4) symmetrical Composite plan—**45**–**58** experiments;

(5) plan of experiments (Box)—**44**–**76** experiments.

Considering constrains of time, labor and cost the following plan had been chosen:

—nonsymmetrical almost full Hartley plan of experiments;

—total amount of experimental points—N = 17;

—total amount of experiments—N*nu = 17*3 = 51;

—repetition of experiment in one point—nu = 3.

Levels of variation and intervals of changes for technological parameters (dependent variables) are given in table.

## 3. EXPERIMENTAL EQUIPMENT AND PROCEDURES

The experimental part of the work had been done by using the equipment shown at Fig. 2. It includes the following devices:

Levels of variation of the factors

| Levels of variation and intervals of change technological factors | Code Scale | Power (P) | Distance between focusing point of powder stream and sample (FP) | Operation Speed (V) | Feeding Rate (FR) |
|---|---|---|---|---|---|
| Unit | | W | mm | mm/min | g/min |
| Main (Ground) level | 0 | 1700 | 0 | 650 | 10 |
| Interval of variation | 1 | 200 | 6 | 350 | 5 |
| High level | 1 | 1900 | 6 | 1000 | 15 |
| Low level | −1 | 1500 | −6 | 300 | 5 |

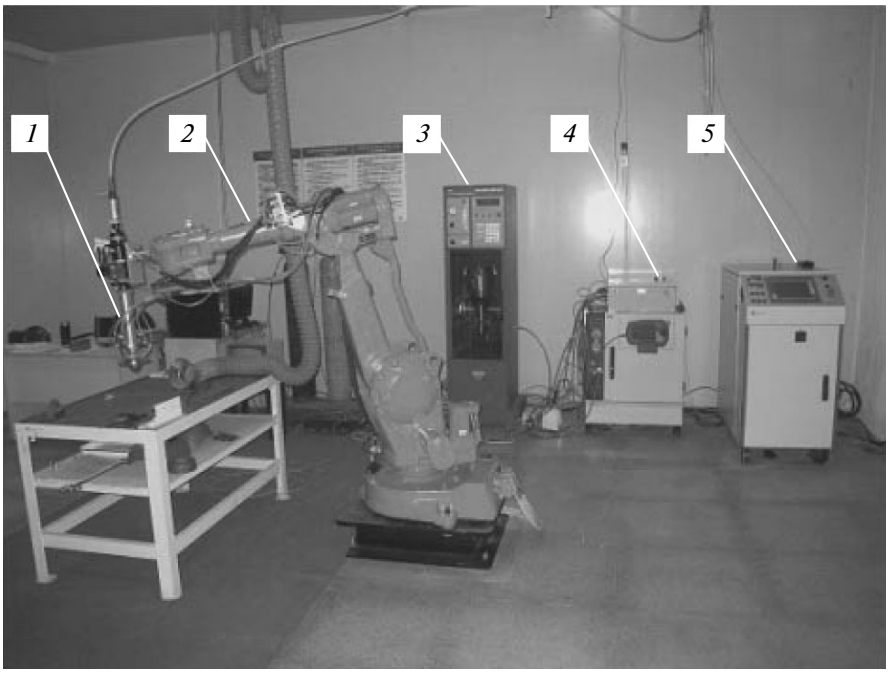


**Fig. 2.** The general view of industrial robotized system based on diode laser: *1*—Laser beam focusing system coaxial with powder nozzle; *2*—Robot; *3*—Feeder; *4*—Robot controller; *5*—Fiber Coupled Diode Laser.

(1) Robot: IRB 2400 ABB (Switzerland) is a 6-axis industrial robot, designed specifically for manufacturing industries that use flexible robot-based automation. The robot has an open structure that is specially adapted for flexible use, and can communicate extensively with external systems. Its main parameters: the load limit is 16 kg, positioning accuracy is 0.70 mm, and arm working radius is 1.4 m.

(2) Laser: LDF400-2000 Fiber-Coupled Diode Lasers. Its main parameters: the wavelength is 900–980 nm, output power is 2000 W, and transverse mode is multi-mode.

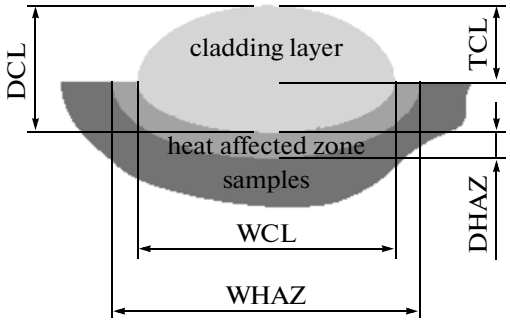


**Fig. 3.** Scheme of the cross section structure.

(3) Powder feeder with closed-loop feed rate monitoring and control system: Rotameter and mass flow carrier gas metering models available. The powder feeding rate is from 2 g/min to 50 g/min.

Samples for experimental research had been prepared from the stainless steel 2Cr13 (C—0.21%, Cr—13%, Si—1.16%, Ni—0.77%, Fe—the rest). Samples had been irradiated at focused beam diameter ∅4 mm according to the plan of experiments.

Sample dimension is 40 × 100 × 11 ($mm^3$), and 2Cr13 powder with particle size of 50–75 μm was used. The wire electrical discharge machine had been used to cut sample crosssection. After sectioning samples had been subjected to standard metallographic procedures for futher studies. Micro-hardness and dimension measurements had been done using digital microhardness meter HDX-100 (China). Typical crosssection structure of treated layers is demostrated at Fig. 3, where TCL—the thickness of cladding layer, DCL—depth of cladding layer, WCL—width of cladding layer, HCL—hardness of cladding layer, DHAZ—depth of heat affected zone, WHAZ—width of heat affected zone, HHAZ—its hardness.

## 4. DISCUSSION OF THE RESULTS

As a result of calculations the coefficients for regression equation had been found. To describe the dimensions parameters of the processed layers and micro hardness changes these coefficients are presented as a range diagrams (Fig. 4a and 4b). Analyzing

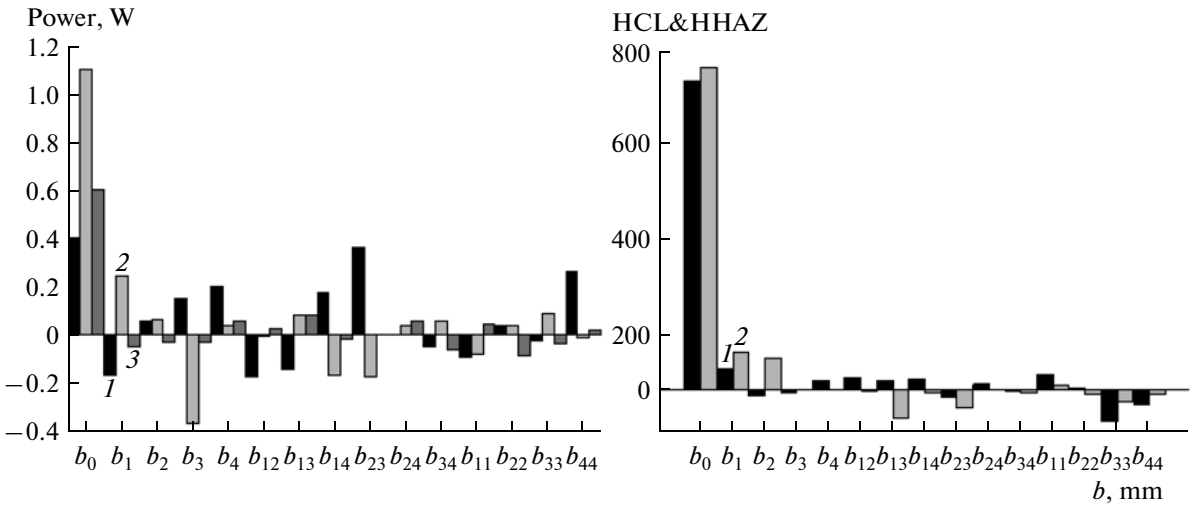


**Fig. 4.** (a) Regression coefficients for thickness of cladding layer (TCL), depth of cladding layer (DCL) and depth of the heat affected zone (DHAZ). *1*—TCL; *2*—DCL; *3*—DHAZ; *x1*—power; *x2*—distance between focusing point of laser and sample; *x3*—operation speed; *x4*—feeding rate. (b) Regression coefficients for hardness of cladding layer (HCL) and Hardness of the heat affected zone (HHAZ). *1*—HCL; *2*—HHAZ.

these results one may see that the main factors which are influencing the cladding quality are the following: laser radiation power (and hence the power density), distance between the focusing point of focused laser beam and sample, operational speed of cladding and the powder feeding rate.

Based on the same algorithm the dependences of other cladding process results (dimensions of the processed area, surface roughness, micro hardness, size of HAZ (Heat Affected Zone), distribution of chemical elements, wear resistance, strength, etc.) from various working conditions may be determined.

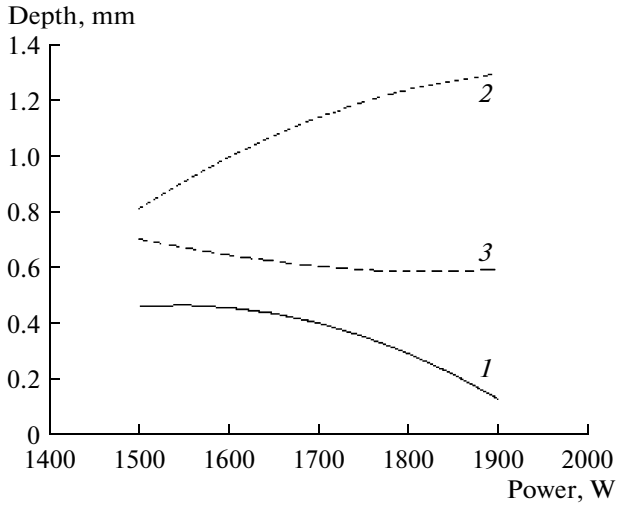


**Fig. 5.** Thickness and depth of cladding layer, depth of HAZ VS Power. *1*—TCL vs. Power; *2*—DCL vs. Power; *3*—DHAZ vs. Power.

## 5. CONCLUSIONS

(1) To describe the laser cladding processing the statistical model based on results of experimental research had been developed.

(2) Considering constrains of time, labor and cost, the nonsymmetrical almost full Hartley plan had been chosen for modeling realization.

(3) The dimensions and hardness of the cladding layers are mainly influenced by the following factors—power and movement speed of the heating source, the mass feeding rate of the injected powder, the position of component in relation to the powder stream, etc.

(4) The developed model is valid within the limits of the given multifactors space.

(5) Model may be used for practical choosing of optimal working conditions for laser cladding at industrial level.

## 6. ACKNOWLEDGMENTS

This research had been done in the framework of China-Ukraine scientific collaboration agreement. The authors would like to appreciate the financial support from the International Cooperation Project of the Ministry of Science and Technology of the People's Republic of China (JG-JD-2008001).

## REFERENCES

1. Adler, Yu.P., Markova, E.V., and Granovski, Yu.V., *Experiment Planning at Search for Optimal Conditions*, Moscow: Nauka, 1976.
2. Nalimov, V.V., *Theory of Experiment*, Moscow: Nauka, 1971.
3. Novik, F.C. and Arsov, Ya.B., *Optimization of Processes of Metal Technology with Methods of Experiments Planning*, Moscow: Nauka, 1980.
4. Kovalenko, V., Anyakin, M., and Uno, Y., Modeling and Optimization of Laser Semiconductors Cutting, *Proc. International Congress of Lasers & Electro-Optics "ICALEO'2000"*, Dearborn, USA, 2000, vol. 90, pp. D82–D92.
5. Ng, G.K.L. and Li, L., Optimisation of Laser Percussion Drilling for Improved Reliability, *Proc. International Congress of Lasers & Electro-Optics'2002 "ICALEO'2002"*, Scottsdale, USA, 2002.
6. Kovalenko, V., Uno Yoshiyuki, Anyakin, M., and Okamoto Yasuhiro, Laser Cutting of Semiconductor Elements, *International Journal of Electrical Machining*, 2002, no. 7, pp. 9–14.

ISSN 1068-3755, Surface Engineering and Applied Electrochemistry, 2010, Vol. 46, No. 3, pp. 271–275. © Allerton Press, Inc., 2010.
Original Russian Text © S.A. Baranov, 2010, published in Elektronnaya Obrabotka Materialov, 2010, No. 3, pp. 87–93.

OPERATING EXPERIENCE

# A Three-Layer Model of an Amorphous Microwire

**S. A. Baranov**[a, b]

[a] *Institute of Applied Physics, Academy of Sciences of Moldova, ul. Academiei 5, Chisinau, MD–2028 Republic of Moldova*
[b] *Shevchenko Pridnestrov'e State University, ul. 25 Oktyabrya 128, Tiraspol, Republic of Moldova*
*e-mail: baranov@phys.asm.md*

Received March 12, 2010

**Abstract**—A theory of a three-layer model for an amorphous microwire is studied. The obtained theoretical results are confirmed by an experiment. For a more precise comparison of the theory with the experiment, a series of experimental measurements is needed, which are also discussed in the paper.

**DOI:** 10.3103/S1068375510030142

## INTRODUCTION

Any rapidly hardened objects (a band, powders, films, or an amorphous microwire) obtained directly from a liquid phase are known to undergo a state of tension. A microwire's tension can be subdivided into the following:

(1) Hardened-remnant tensions, which occur due to the nonuniformity of the object cooling down.

(2) The tensions resulting from various coefficients of thermal expansion (CTE) of metal, glass, and a transition layer.

The first type tensions are undoubtedly significant in a microwire, especially with the glass insulation removed off the fiber core. However, both the experimental studies and the theoretical estimations show [1–6] that, in a regular cast microwire, they are more than an order of magnitude less than the tensions of the second type that occur due to common glass insulation. The interest in the second type tensions is correlated with a number of special physical aspects, e.g., with the effect of natural ferromagnetic resonance [1, 2]. Thererfore, only the tensions involved by the CTE difference are to be discussed.

In a microwire casting based on Ulitovskii's method, the tensions increasing in the glass-to-metal seal upon the composite's cooling down are observed. We shall call them elastic tensions for short. Usually, the study of such microwire tensions is restricted to the glass insulation state's examination, because, as a rule, the higher the tensions are, the more brittle the glass insulation may become. A great number of papers have dealt with such studies (see the reviews in [3–6]).

Below, the tensions arising in a metal fiber core are to be considered and a microwire model that consists of three layers is to be discussed.

A three-layer model has a profound justification. The existence of an intermediate layer (IL) between the glass and metal are discussed in [3–6]. The elastic tensions in the glass due to the CTE difference, conditionally denoted as $\alpha_i$, may decrease upon the introduction of a given layer having specified physical properties.

Below, let us present a microwire in the form of the coaxial cylindrical surfaces having the radii of $R_i$ ($i$ = 1, 2, 3) correspondingly for the fiber core, glass, and the IL sealed after cooling down from $T^*$ ($T^* \approx 500$–700°C) once all of the plastic relaxations have been accomplished. Consider in the cylindrical coordinates the bias field of the elastic deformations as functions of $U_r$ and $U_z$ (along the axes $r$ and $z$). From the problem's symmetry and in a linear approximation, the data of the bias field are introduced for the fiber core of the metal:

$$U_r = a_1 r, \tag{1}$$

$$U_z = b_1 z. \tag{2}$$

For the glass layers ($k = 2$) and the IL (wire–glass) ($k = 3$),

$$U_r = a_k r = \frac{c_k}{r}, \tag{3}$$

$$U_z = b_k z. \tag{4}$$

The term $\frac{c_1}{r}$ for the metal fiber core is eliminated for the following reasons. At $r \longrightarrow 0$, it leads to infinite elastic displacements. In the given approximation, the relative deformations of the fiber core are independent of $r$.

Hook' law takes the following form for the wire:

$$\sigma_{r(\varphi)} = \lambda_1(a_1 + \nu_1 b_1), \tag{5}$$

$$\sigma_z = 2\lambda_1\nu_1(a_1 + \nu_1 b_1) + E_1 b_1. \tag{6}$$

For the shells ($k = 2, 3$),

$$\sigma_r = \lambda_k(a_k + \nu_k b_k) - \lambda_k \frac{c_k}{r^2}(1 - 2\nu_k), \quad (7)$$

$$\sigma_\varphi = \lambda_k(a_k + \nu_k b_k) + \lambda_k \frac{c_k}{r^2}(1 - 2\nu_k), \quad (8)$$

$$\varphi_z = 2\lambda_k \nu_k (a_k + \nu_k b_k) + E_k b_k, \quad (9)$$

where

$$\lambda_i = \frac{E_i}{(1 + \nu_i)(1 - 2\nu_i)}, \quad (10)$$

and $E_i$ are Young's modulus, and $v_i$ are the Poisson coefficients. The boundary conditions for the tension are written from the equilibrium conditions of the forces affecting the three subsystems (the fiber core, the IL, and the glass).

$$(\sigma_r)_{r = R_1 = 0}, \quad (11)$$

$$|\sigma_r|_{r = R_{i-0}} = |\sigma_r|_{r = R_{i+0}}, \quad (12)$$

where $R_i$ is the boundary between the systems of the fiber core–IL and the IL–glass.

$$f_i|\sigma_z|_{r = R_{i-0}} = f_k|\sigma_z|_{r = R_{i+0}}, \quad (13)$$

where $i$, $k$ are the cross section areas of the systems of the fiber core, the IL, and the glass. The conditions are written for the fiber core–IL and the IL–glass pairs. If an external voltage is applied to the microwire, the final condition should be added: $\sigma$ (the external voltage) instead of a zero.

The conditions for the relative displacements are as follows:

$$(b_i)_{r = R_{i-0}} - (b_k)_{r = R_{i+0}} = \varepsilon_{ik}, \quad (14)$$

$$(a_i)_{r = R_{i-0}} - (a_k)_{r - R_{i+0}} = \varepsilon_{ik}, \quad (15)$$

The $\varepsilon_{ik}$ parameter determines the difference between the thermal deformations of the materials:

$$\varepsilon_{ik} = \int_{T_r}^{T^*} (\alpha_i - \alpha_k) dt. \quad (16)$$

A linear dependency of $\varepsilon_{ik}$ on the temperature is often used for the estimation:

$$\varepsilon_{ik} \approx (\alpha_i - \alpha_k)(T^* - T_r). \quad (17)$$

The problem solution in a general form is possible only numerically. The following approximated analytical solution for the axial extension of the fiber core will suit us hereafter:

$$b_1 = b_1^0 + b_1', \quad (18)$$

$$b_1^0 = \varepsilon_{12} \frac{kx}{kx + 1}, \quad (19)$$

$$b_1' \cong \varepsilon_{13} k_1 x_1, \quad (20)$$

where

$$k = \frac{E_2}{E_1}; \quad x = \frac{f_2}{f_1}; \quad k_1 = \frac{E_3}{E_1}; \quad x_1 = \frac{f_3}{f_1}.$$

For obtaining the solution all of $v_i = 1/3$. Since the IL properties are little known, there are good reasons to consider that $x_1 \ll 1$; $\varepsilon_{13} < \varepsilon_{12}$. Herewith, $b_1' < b_1^0$, which confirms the accepted approximation for obtaining the solution. It is shown experimentally that $b_1'$ makes up no more than 20% of $b_1^0$; therefore,

$$b_1 \approx \varepsilon_{12} \frac{kx}{kx + 1}. \quad (21)$$

Let us then write the result for the tensions in the fiber core, which we shall further study:

$$\sigma_r = \sigma_\varphi \equiv P,$$
$$P = \varepsilon E_1 \frac{kx}{(k/3 + 1)x + 4/3}, \quad (22)$$

$$\sigma_z = P \frac{(k + 1)x + 2}{kx + 1}. \quad (23)$$

Let us estimate the tensions that appear in the fiber core commonly for the parameters of

$$\varepsilon = \varepsilon_{12} \sim (5–6) \times 10^{-3},$$
$$k \sim 0.3–0.5, \quad (24)$$
$$E_1 \sim (1.5–1.9) \times 10^{11} \ \text{H/m}^2.$$

If $x \gg 1$, then the fiber core tensions have the order of

$$\sigma_z \sim 3\sigma_{r(\varphi)} \sim \varepsilon E_1 \sim 10^9 \ \text{H/m}^2. \quad (25)$$

If $x \sim 1$,

$$\sigma_z \sim 2\sigma_{r(\varphi)} \le 10^8 \ \text{H/m}^2. \quad (26)$$

The given tensions prevail over the other forms of tensions that appear in the process of the microwire's amorphous casting, which is confirmed both by the experimental examinations and the theoretical calculations [1–5].

## COEFFICIENT OF THERMAL EXPANSION

An important parameter for which the microwire's composite properties are manifested is the coefficient of thermal expansion. For the above model,

$$\alpha_{eff} = \alpha_1 + \alpha_2, \quad (27)$$

where

$$\alpha_1 = \frac{\alpha_m + kx\alpha_g}{1 + kx}, \quad (28)$$

where $\alpha_m \sim 10^{-5}$ K$^{-1}$, and $\alpha_g \sim 0.5 \times 10^{-5}$ K$^{-1}$.

It is known from the experiments that the coefficient of the thermal expansion with sufficiently high accuracy

is described by formulas (27) and (28). The $\alpha_2$ addition is small and it can be ignored; then, from the comparison with the experiment, one may assume that

$$\alpha_2 < \alpha_1. \quad (29)$$

Let us perform the typical estimations. Conventionally, if $k \approx 0.5$, one gets

$$\alpha_{,eff} < \alpha_m,\ \alpha_{eff} \approx 0.7 \times 10^{-5}\ \mathrm{K}^{-1};$$

that is, the coefficient of the thermal expansion of the microwire becomes 1.4 times less than that of the microwire fiber core with the glass shell removed.

The above effect is confirmed experimentally [3–5].

## YOUNG'S EFFECTIVE MODULUS

Let us present Young's effective modulus as follows:

$$E_{eff} = E^0 + E', \quad (30)$$

where

$$E^0 = E_1 \frac{kx+1}{x+1}, \quad (31)$$

$$E' \sim k_1 x_1. \quad (32)$$

Young' modulus for a thin microwire is known to greatly exceed the one for the similar amorphous materials. The surface oxide layer (the metal fiber core is covered with) is assumed to be a significant factor and involve Young's modulus increasing.

Young's modulus for the metal oxides is found to exceed the one for the metals (say, by an order). Therefore, if for the microwire having a 1μm diameter of the fiber core $E^0$ and $E'$ are considered to be of one order, one may estimate the parameter of $x_1 \sim 0.1$.

Upon a decrease of the microwire fiber's core diameter with Young's modulus increasing, the ultimate tension of the hyperfine microwire also increases. In our opinion, those two phenomena are of the same nature. This effect was earlier called the dimensional effect of the microwire's strength increase. Note that thin microwires with the dimensional effect have a higher specific electrical resistance.

Consider next that Young's modulus in the amorphous materials depends on the magnetostriction of the magnetic and domain structure. This effect, known as the delta $E$ effect, seems to somewhat decrease Young' modulus.

## TENSOR SENSITIVITY

A significant value that makes it possible to measure the pressure or tension using a simple electric method is known as the microwire's tensor sensitivity. Let us determine the coefficient of the tensor sensitivity of a wire to deformation and express it through the electric resistance varying. The electric resistance of metals well obeys the following formula:

$$R = \rho \frac{L}{S}, \quad (33)$$

where $L$ is the length of the wire, $S$ denotes the cross section areas, and ρ designates the specific electric resistance of the material.

The electric resistance modification is

$$\frac{dR}{R} = \left(\frac{dR}{R}\right)_T + \left(\frac{dR}{R}\right)_\varepsilon. \quad (34)$$

The first term is absent at a constant temperature

$$\frac{dR}{R} = \left(\frac{dL}{L}\right) - \left(\frac{dS}{S}\right) + \left(\frac{d\rho}{\rho}\right). \quad (35)$$

Since the specimen's cross section modifies with the expansion (or compression) of the material in one direction according to Poisson's $v$ coefficient, then

$$\frac{dS}{S} = -2v\left(\frac{dL}{L}\right). \quad (36)$$

Hence,

$$n = \frac{dR/R}{dL/L} = (1+2v) + \frac{d\rho/\rho}{dL/L}, \quad (37)$$

where $n$ is known as the coefficient of the tensor sensitivity of the material. As a rule, $\nu = 1/3$ for metals; therefore. $n = (1 + 2\nu) \approx 1.7$. Considering the second term, it increases, but it is limited by a value of 2. However, in the composite, the $\tilde{\nu}$ value may differ from 1/3. Poisson's coefficient is known to be determined through the values of $k^*$ (the modulus of the compression) and μ (the modulus of the shear) ($k^*$, $\mu > 0$):

$$v = \frac{1}{2}\frac{3k^* - 2\mu}{3k^* + \mu}. \quad (38)$$

Since $k^*$ and μ are always positive, ν may vary for the different substances only within the limits of

$$-1 \le \nu \le 1/2 \quad (39)$$

(the given limits are obtained at $k^* = 0$ and at $\mu = 0$).

Virtually, Poisson's coefficient changes only in the limits of

$$0 \le \nu \le 1/2. \quad (40)$$

However, all the above refers to a solid-state body that appears to be an isolated thermodynamic system. For the isolated system, i.e., a microwire, which comprises a fiber core and a shell (IL), equality (40) is accomplished.

Using system of equations (7)–(15), let us carry out Poisson's coefficient's calculation for the wire in the a-wire-and-a-shell model (the shell serves as the

**Table 1.** Dependency of the specific resistance on the manganese content (U weight %) for the iron based alloy

| U weight % | 1 | 2 | 3 |
|---|---|---|---|
| ρ, μOhm cm ($t \approx 20$°C) | 180 | 190 | 200 |
| Error (%) | 20 | 20 | 15 |

**Table 2.** TCR dependency of the manganese content (U weight %) for the iron based alloy

| U weight % | 1 | 2 | 3 |
|---|---|---|---|
| $\alpha \times 10^{-5}$ (1/degree) (20°C–250°C) | 10 | 8 | 5 |
| Error (%) | 15 | 10 | 10 |

electric isolator). After the appropriate calculations, assuming $\nu = 1/3$, one can obtain

$$\nu_{eff} = \frac{x(4/3k + 1) + 4/3}{x(k + 3) + 4}, \quad (41)$$

where $x$ is the ratio of the cross section areas of the external shell to the metal fiber core, and $k$ denotes the ratio of Young's modules of the external shell to the fiber core.

Let us examine the obtained formula (41): if $x \longrightarrow 0$, then $\nu_{eff} \longrightarrow 1/3$; i.e., the limiting transition for the case of the insulation's absence is fulfilled.

The most interesting case is when

$$kx \gg 1;$$

then, $\nu_{eff} \longrightarrow 4/3$, which is relevant for

$$n \longrightarrow 3.67. \quad (42)$$

This is the limiting value for the tensor sensitive wire covered with a shell. For the regular amorphous microwire, if the glass is regarded as a shell (i.e., without considering the IL ($k \le 0.3$)) but $x \gg 1$, the following limiting case is accomplished:

$$\nu_{eff} = \frac{4/3k + 1}{k + 3} \sim \frac{1.4}{3.3} \sim 0.4, \quad (43)$$

thus leading to no substantial change of the coefficient of the tensor sensitivity. Indeed, it is experimentally known that the tensor sensitivity of a microwire actually remains unchanged upon the glass insulation etching off.

## RESULTS AND DISCUSSION

For the theory's immediate verifying, the following model system was created. Using the method for the lead vacuum retraction from the melt into a capillary of Pyrex brand glass, a lead microwire in a glass shell was manufactured. In the case of the lead microwire with a Pyrex glass shell, $k \sim 5$, which was a successful example for verifying formula (41). The wire with $x \approx 2$ was the most advantageous one for the measurements. From the table data for the lead without the glass shell, $\nu \sim 0.7$. The measurement of $n$ in the case with the glass shell's presence leads to the theoretical calculation of Poisson's efficient coefficient:

$$\nu_{eff} \sim 0.9.$$

For the microwire with the amorphous fiber core,

$$n \sim 2–2.9$$

and actually it is independent of the glass insulation's presence. For the amorphous materials in the form of a band from the same alloys, $n$ does not usually exceed 2. To explain these results, let us take the model of the fiber core with a shell. The surface layer (SL), for which $k_1x_1 \sim 1$, is assumed to be the shell. Note that, in the limiting case, when $k_1x_1 \gg 1$ and $\nu \longrightarrow 4/3$, $n \sim 3.67$. The given theory thus may account for the phenomenon of the enhanced value of $n$ of the tensor sensitivity for the microwire. Experimentally, the SL etching was also carried out, which mostly led to the fiber core's destruction. For the specimens when we managed to measure $n$, it decreased to 2.

One may assume that the thermal processing may affect the characteristics of the transitional layer.

The tensor sensitivity actually remains unchanged upon the annealing up to 350°C. The annealing at 350°C for half an hour modifies the tensor sensitivity of the FeBSiCMn wire from 3 to 2.5. Further annealing of this alloy involves the brittleness of it. Note that, at the thermal processing with a temperature of above 300°C, the change of the microwire'sspecific resistance also occurs.

The microwire with the amorphous structure of the fiber core can have enhanced tensor sensitivity; therefore, the microwires based on Fe–MN–C–Si and having the above properties were examined.

The most stable among the compositions under study were those containing increased quantities of B and Si. The values of the tensor sensitivity coefficient for these alloys are 2.7–2.6, correspondingly, with the values of the temperature coefficient of the resistance (TCR) being $(8.5–12.6) \times 10^{-5}$ K$^{-1}$. Among the above alloys, the iron-based with the following additives is the best: 1 C wt %, 5 Si wt %, and 4 Mn wt %, which also manifests the best mechanical strength (an ultimate tension of 3500–4000 MPa) among the alloys under consideration.

The amorphous microwires discussed have a fairly high electric resistance (200 μOhm cm). The indicated properties make it possible to use the microwire with the amorphous structure fiber core for the production of tensometric sensors.

## CONCLUSIONS

(1) The resistances are calculated for the three-layer model of a cast amorphous microwire.

(2) The coefficient of thermal expansion and Young's effective modulus along with the tensor sensitivity for the offered model are found.

(3) The obtained theoretical results are confirmed by the experiment. For the more precise comparison of the theory with the experiment, a series of experimental measurements seem necessary, which are also discussed in the paper.

## REFERENCES

1. Baranov, S.A., Radioabsorption Properties of Amorphous Microwires, *Moldavian J. Phys. Sci.*, 2009, vol. 8, nos. 3–4, pp. 335–339.
2. Baranov, S.A., Magnetic Properties of Micro- and Nanowire in the Superhigh – Frequency Range, *Surf. Eng. Appl. Electrochem.*, 2009, vo. 45, no. 6, pp. 441–445.
3. Baranov, S.A., Stoianov, S.S., Experimental Measurement of a Tensing in a Microwire, *Surf. Eng. Appl. Electrochem.*, 2008, vol. 44. no. 2, pp. 98–105.
4. Baranov, S.A., Residual Stress in Amorphous Microwire, *Surf. Eng. Appl. Electrochem.*, 2006, vol. 42, no. 6, pp. 44–46.
5. Baranov S.A., Residual Stress Investigation in Cast Glass-Covered Amorphous Magnetic Microwire by Ferromagnetic Resonance Method, *Moldavian J. Phys. Sci.*, 2002, vol.1, no. 4, pp. 73–76.
6. Baranov S.A., Estimation of Distribution of Residual Stresses in Core Amorphous Microwires, *Met. Sci. Heat Treat.*, 2001, vol. 43, nos. 3–4, pp. 167–168.

ISSN 1068-3755, Surface Engineering and Applied Electrochemistry, 2010, Vol. 46, No. 3, pp. 276–280. © Allerton Press, Inc., 2010.
Original Russian Text © M.K. Bakhadyrkhanov, G.Kh. Mavlonov, S.B. Isamov, K.S. Ayupov, Kh.M. Iliev, O.E. Sattarov, S.A. Tachilin, 2010, published in Elektronnaya Obrabotka Materialov, 2010, No. 3, pp. 94–99.

OPERATING EXPERIENCE

# Photoconductivity of Silicon with Multicharged Clusters of Manganese Atoms $[Mn]_4$

**M. K. Bakhadyrkhanov, G. Kh. Mavlonov, S. B. Isamov, K. S. Ayupov, Kh. M. Iliev, O. E. Sattarov, and S. A. Tachilin**

*Tashkent State Technical University, ul. Universitetskaya 2, Tashkent, 100095 Uzbekistan*

*e-mail: mavlonov_g@mail.ru*

Received January 18, 2010

**Abstract**—The features of the photoelectric properties of silicon with multicharged nanoclusters of manganese atoms are studied. The patterns of change in the multiplicity of the charge state of the nanoclusters as a function of the Fermi level position are determined. It is shown that the samples with the maximum multiplicity of the charge of the nanoclusters exhibit a number of new physical effects, i.e., anomalously high extrinsic photoconductivity within a range of 3–5 μm, giant residual conductivity, and photoconductivity stimulated by an electrical field. In samples with a minimal charge state of the nanoclusters, the effect of anomalously deep infrared quenching of the photoconductivity is observed, the quenching multiplicities of which achieve 6 or 7 orders. The laws for controlling the photoelectric properties of silicon by changing the charge state of the nanoclusters are determined.

**DOI:** 10.3103/S1068375510030154

The behavior of the manganese atoms in the silicon lattice depends heavily on the conditions of the doping and postdiffusion annealing [1–3]. The results of studies [4] show that the standard high-temperature diffusion of manganese in silicon not only makes it possible to obtain samples with a stable state of manganese atoms in the lattice but also leads to a significant erosion of the surface and the formation of various SiMn-type silicides in the near-surface region of the material. The disadvantages of high-temperature diffusion significantly impede the use of some interesting phenomena observed in Si⟨B, Mn⟩ in electronics [5–6]. Therefore, we have developed a new method of doping, i.e., low-temperature diffusion. The principle of this method is that the diffusion is carried out starting from room temperature with its gradual increasing up to the desired final value at a set rate. The number of stages, the time of the exposure at each stage, and the final temperature of the diffusion are governed by the parameters of the original material and the requirements for the parameters of the resulting samples.

The original material was *p*-type single-crystal silicon with the resistivity $\rho \sim 5\ \Omega$ cm. By controlling the conditions of the doping, we obtained compensated *p*-Si⟨B, Mn⟩ and overcompensated *n*-Si⟨B, Mn⟩ samples with the resistivity $\rho \sim 10^3$–$10^5\ \Omega$ cm. In these samples obtained using the new method of doping, we did not find erosion and the formation of various alloys of SiMn either on the surface or in the near-surface region. Unlike the samples with the same resistivity that were obtained by the high-temperature diffusion, they exhibit stable and reproducible electric parameters, and the process of decomposition does not take place in them for a long time in the temperature range $T = 300$–$420$ K. They also exhibit extremely high photosensitivity. To study the state of the manganese atoms in the lattice of silicon doped using the new method, we investigated the EPR spectra of these samples at $T = 77$ K using a Broker installation. The results of the investigation showed that these samples comprise more pronounced hyperfine spectra consisting of 21 lines, which were observed in [2, 3, 7]. The authors of these works attributed these spectra to the formation of nanoclusters of manganese atoms $[Mn]_4$. It should be noted that the hyperfine spectra associated with $[Mn]_4$ are more clearly seen in compensated *p*-Si⟨B, Mn⟩ with the resistivity $\rho \sim (6$–$7) \times 10^3\ \Omega$ cm; the Fermi level in them corresponds to $E_F = E_V + 0.38$ eV. The shift of the Fermi level to the midgap (i.e, the increase in the resistivity of the material) leads to smearing and decreasing of the amplitude of the spectrum in the *p*-Si⟨B, Mn⟩ samples with $\rho > 6 \times 10^4\ \Omega$ cm; hyperfine spectra are not observed in overcompensated samples either. In the *n*-type samples doped with manganese, irrespective of their resistivity, the EPR spectra related to $[Mn]_4^0$ were not observed. However, it should be noted that, according to the calculations based on the results of the Hall effect, in both the compensated and overcompensated samples under study, as well as in the *n*-silicon doped with manganese, the concentration of electroactive atoms is nearly the same and differs by no more than 1%. Therefore, we can assume that the negatively charged atoms of boron

stimulate the self-organization of nanoclusters whose structure can be represented in the form $[(Mn)_4^{+n}B^-]^{+(n-1)}$; that is, the boron atom is at the center of the nanocluster, and four positively charged atoms of manganese are in the equivalent nearest-neighbor interstitial positions [3]; that is, the nanoclusters of manganese atoms may be in a multicharged state. This assumption can be confirmed by the fact that, in the compensated $p$-Si⟨B, Mn⟩ samples, in which the spectra related to $[Mn]_4$ clusters are clearly detected, the manganese atoms are in a charged state ($Mn^+$ and $Mn^{++}$). As is known [8], manganese atoms in silicon form two donor levels with the activation energy $E_1 = E_c - 0.3$ eV and $E_2 = E_c - 0.5$ eV; therefore, we can assume that the nanoclusters are in a multicharged state. Hence, depending on the Fermi level position in the samples under study, the concentration of atoms with the $N^0_{Mn}$, $N^+_{Mn}$, and $N^{++}_{Mn}$ state changes significantly. As the Fermi level shifts from the lower position in the band gap to the upper position, the number of atoms in the $N^{++}_{Mn}$ state decreases and, accordingly, the concentration of $N^+_{Mn}$ and $N^0_{Mn}$ increases; in the overcompensated samples, $N^0_{Mn} > N^+_{Mn}$ and, accordingly, the multiplicity of the charge state of the nanoclusters varies from $[(Mn)_4^{+8}B^-]^{+7}$ to $[(Mn)_4^{+4}B^-]^{+3}$. Thus, changing the Fermi level position in the samples from $E_F = E_V + 0.38$ eV to $E_F = E_C - 0.45$ eV, we can change the multiplicity of the nanoclusters in the range $n = +(7-3)$; hence, we can assume that the nanoclusters are in a multicharged state.

It is of great interest to study the physical properties of silicon samples with such multicharged states. The results of studying the magnetic properties of the samples have shown [9] that these materials exhibit an anomalously high negative magnetoresistance at $T =$ 300 K. It is of interest to study the photoelectric properties of these samples because, for one thing, as far as we know from the literature, the effect of multicharged centers $N^{\pm n}$ (where $n > 3$) on the photoelectric properties is hardly studied at all and, for another thing, these materials make it possible to develop fundamentally new sensitive photodetectors, efficient photocells, and elements of optical memory.

The photoelectric properties of the samples were studied using an IKS-21 spectrometer equipped with a cryostat that allows studying the photoconductivity (PC) in a wide range of temperatures ($T = 77-350$ K), the electric field, and the intensity of the background light. The PC in all the samples was studied under identical conditions. To study only the extrinsic PC, we used a double filter of a polished silicon wafer, which was installed in front of the cryostat window behind the IKS-21 globar.

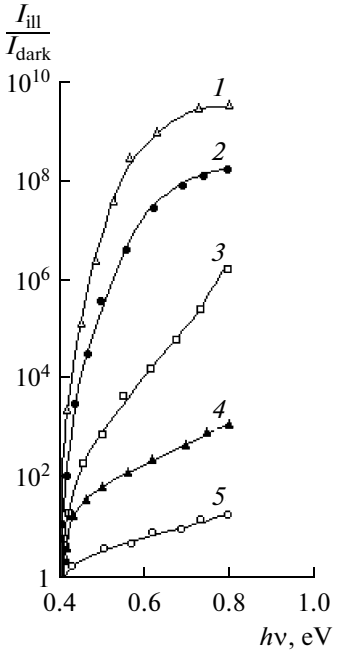


**Fig. 1.** Spectral dependence of the PC of the Si⟨B, Mn⟩ samples with nanoclusters of manganese atoms with different Fermi level positions: (*1*) $E_F = E_V + 0.38$ eV, (*2*) $E_F = E_V + 0.42$ eV, (*3*) $E_F = E_V + 0.48$ eV, (*4*) $E_F = E_V + 0.385$ eV, and (*5*) $E_F = E_C - 0.45$ eV.

Figure 1 shows the spectral dependence of the PC of the $p$-Si⟨B, Mn⟩ samples with nanoclusters of manganese atoms with different Fermi level positions. As can be seen in the figure, in the samples with nanoclusters with a maximum multiplicity of the charge, the photoresponse begins at $h\nu = 0.4$ eV; as the photon energy increases, the photocurrent increases continuously and step-wise (curve *1*). In the interval of $h\nu =$ 0.4–0.8 eV, the PC increases by 9 orders; a further increase in the photon energy $h\nu > 0.8$ eV does not lead to its appreciable increase; that is, at 0.8 eV, the photocurrent saturation region begins. Thus, these samples exhibit a giant extrinsic PC in the wavelength range of $\lambda = 1.5-3$ μm. As the Fermi level shifts to the conduction band, whilst the continuous and stepwise increase in the PC is preserved in the spectrum region under discussion, its value decreases appreciably (curves *2*, *3*). In the overcompensated $n$-Si⟨B, Mn⟩ samples with the Fermi level position $E_F = E_C - 0.45$ eV, the PC decreases significantly in the entire spectrum region, and, at $h\nu > 0.8$ eV, the PC saturation is not observed (curve *5*). In order to elucidate the nature of the observed giant extrinsic PC, we studied the PC of samples of silicon doped with manganese under identical conditions using high-temperature diffusion. The results showed that the PC in the spectrum region

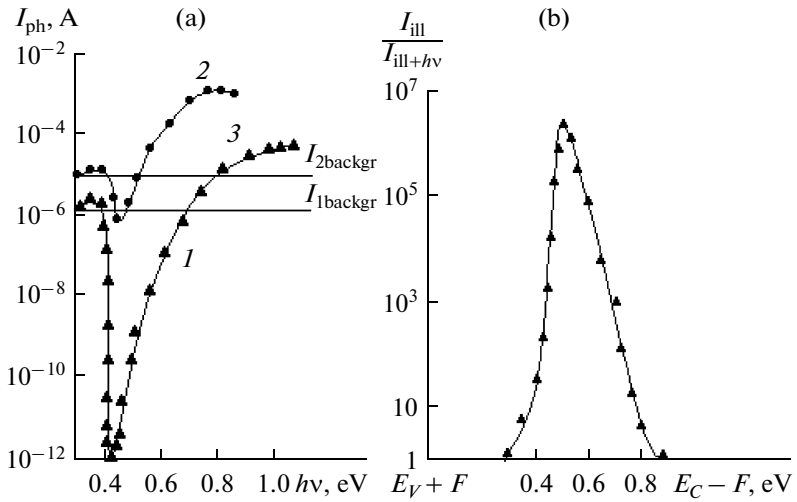


**Fig. 2**. (a) Spectral dependence of the PC in the presence of a background integral light in the $p$-Si⟨B, Mn⟩ samples: (*1*) $\rho = 3 \times (10^4–10^5)$ Ω cm and (*2*) $\rho = (6–7) \times 10^3$ Ω cm. (b) Changes in the multiplicity of the IRQ as a function of the Fermi level position.

under study is lower by 5 or 6 orders (curve *4*) than in the samples with the same electric parameters and the same concentration of electroactive manganese atoms obtained using the new technique (curve *1*). These data indicate that the observed giant extrinsic PC is attributed to the presence of multicharged nanoclusters of manganese atoms. Thus, it is found that, by changing the position of the Fermi level in samples with nanoclusters in the range of $\Delta E_F = [(E_C - 0.45) - (E_V + 0.38)] = 0.29$ eV, we can control the extrinsic PC within 6 to 8 orders. To obtain the maximum extrinsic PC, the samples must have the Fermi level $E_F = (E_V + (0.38–0.42))$ eV, i.e., $\rho = 6 \times 10^3 - 2 \times 10^4$ Ω cm. It is found that the shift of the Fermi level to the valence band $E_F = E_V + 0.38$ eV also leads to an appreciable decrease in the PC; apparently, this is due to the increase in the concentration of holes that are not compensated for by manganese atoms in the valence band.

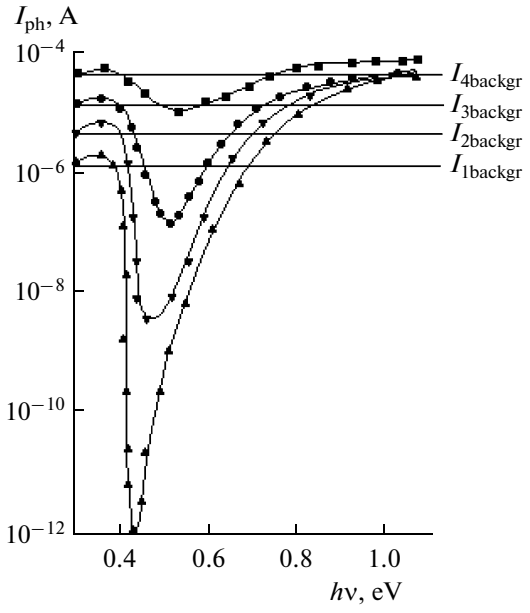


**Fig. 3.** IRQ of the PC as a function of the intensity of the background light in the $p$-Si⟨B, Mn⟩ samples with $\rho = 8 \times 10^4$ Ω cm. $I_1 < I_2 < I_3 < I_4$.

Figure 2a shows the spectral dependence of the PC in the samples under study in the presence of integral background light. As we can see, in the $p$-Si⟨B, Mn⟩ samples with the resistivity $\rho = 3 \times 10^4–10^5$ Ω cm $E_F = (E_V + (0.45–0.52))$ eV, a gigantically deep infrared quenching (IRQ) of the PC is observed (Fig. 2a, curve *1*) with the quenching multiplicity $K\left(\frac{I_L}{I_{L+h\nu}}\right)$ achieving 6 or 7 orders. To the best of our knowledge, such a deep IRQ of the PC has not been found yet in any known photosensitive semiconductor material. In the compensated samples with a giant extrinsic PC, an extremely weak IRQ is observed (Fig. 2a, curve *2*). The change in the multiplicity of the IRQ as a function of the Fermi level position is depicted in Fig. 2b.

It is revealed that, in the samples with the maximum IRQ, a PC occurs at a fairly high intensity of the background light. As the intensity of the background light increases, the quenching depth decreases (Fig. 3). The feature of the IRQ of the PC in these samples is that this effect takes place when the power of the IR light is lower that the power of the background light by a factor of 2–10.

The study of the CVC of the samples in the presence of extrinsic light showed that, in the places of the occurrence of a giant extrinsic PC, the CVC significantly depends on the energy of the incident photons and consists of two regions. In the range of low energy

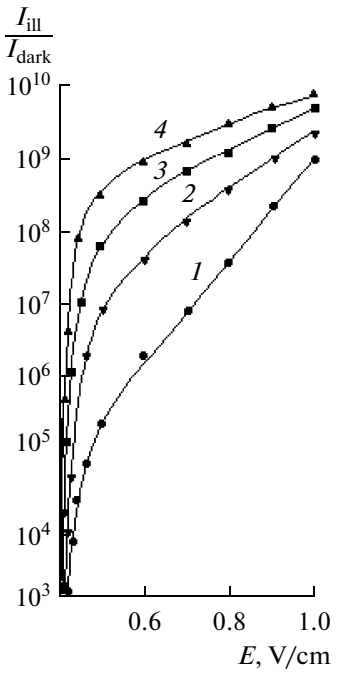


**Fig. 4.** CVC of the samples with $\rho = (6–7) \times 10^3$ Ω cm ($p$-type) at $hv$, eV: (*1*) 0.5, (*2*) 0.546, (*3*) 0.62, and (*4*) 0.68.

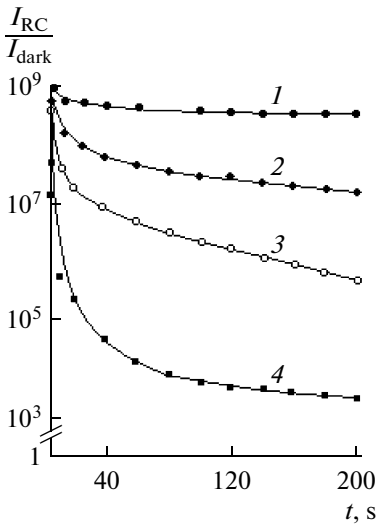


**Fig. 5.** Kinetics of relaxation of the RC: (*1*) $\rho = 7 \times 10^3$ Ω cm, $p$-type; (*2*) $\rho = 1.2 \times 10^4$ Ω cm, $p$-type; (*3*) $\rho = 2 \times 10^4$ Ω cm, $p$-type; and (*4*) $\rho = 10^5$ Ω cm, $n$-type.

fields $E = 0–E_1$, the PC increases by the superlinear law $I \sim E^n$; however, as the photon energy increases, the value of $E_1$ decreases and the value of $n$ grows. At higher electric fields $E > E_1$, the superlinearity of the CVC is preserved and the value of $n$ decreases (Fig. 4). These data show that the electric field significantly stimulates the photosensitivity of the samples.

An interesting effect was observed in the study of the PC relaxation after the light had been switched off (Fig. 5). As we can see, in the samples with the maximum extrinsic PC $p$-Si⟨B, Mn⟩ with $\rho \sim (6–7) \times 10^3$ Ω cm, after switching off the light, the value of the PC hardly changes significantly, it is preserved for a fairly long time; that is, the relaxation of the PC is extremely slow, and a giant residual conduction (RC) is observed (curve *1*). At the same time, in the samples with the Fermi level position closer to the midgap, after switching off the light, the PC experiences a sharp drop by a few orders followed by the relaxation of the RC (curves *2*, *3*). The closer the Fermi level to the midgap is, the faster the relaxation of the RC occurs. In the overcompensated $n$-Si⟨B, Mn⟩ samples, the value of the PC decreases sharply after the light has been switched off, and the value of the RC is considerably lower than in the other samples (curve *4*). The value of the RC heavily depends on the energy of the incident light; that is, a spectral dependence takes place. Thus, it is clearly found that, by changing the position of the Fermi level in the $p$-Si⟨B, Mn⟩ samples, we can control the kinetics and the value of the RC over a wide range. As is known from [10], this RC and its kinetics of relaxation differ significantly from the RC found in other semiconductor materials [11].

It is impossible to explain the experimental results only by the isolated $Mn^0$, $Mn^+$, and $Mn^{++}$ states of the manganese atoms in the silicon lattice. Thus, as was shown in the compensated $p$-Si⟨B, Mn⟩ obtained by standard high-temperature diffusion, where the manganese atoms are mainly in the $Mn^+$ and $Mn^{++}$ states, although the above effects are observed, their values and nature differ significantly from the parameters of the samples obtained using the new technique. Based on the observed effects and the results of the EPR, we assume that the proposed new method of doping stimulates the self-organization of multicharged nanoclusters whose multiplicity of charge can be controlled by changing the Fermi level position in such materials. These nanoclusters exhibit not only unique photoelectric properties but also a high magnetic moment. We believe that a new scientific direction appears, i.e., the development and study of quantum dots with a multiple charge and a magnetic moment. We can assume that a deeper and more comprehensive study of the properties of these materials will allow revealing the features of semiconductor materials with nanoclusters that are not known yet. Based on the experimental data, we can assume that multicharged nanoclusters of manganese atoms $[(Mn)_4^{+n}B^-]^{+(n-1)}$ form a band of energy levels that lie within the range $\Delta E = [(E_V + 0.4)–(E_C– 0.45)] = 0.32$ eV in the band gap of silicon. They contain a few discrete levels with significantly different cross sections of capture of charge carriers. At present, more detailed studies are being carried out in this domain.

## CONCLUSIONS

The features of the PC of silicon with multicharged nanoclusters of manganese atoms are studied. Thus, it is found that these samples exhibit an anomalously high extrinsic PC in the wavelength region $\lambda = 1.5–3$ μm. In addition, it is observed that these samples exhibit a giant residual photoconductivity.

## REFERENCES


1. Ludwig, G.W., Woodbury, H.H., and Carlson, R.O., Spin Resonance of Deep Level Impurities in Germanium and Silicon, *J. Phys. Chem. Solids*, 1959, vol. 8, p. 490.
2. Kreissl, J. and Gehlhoff, W., Electron Paramagnetic Resonance of the $M_4^0$ Cluster in Silicon, *Phys. Status Solidi B*, 1988, vol. 145, p. 609.
3. Fistul', V.I., Kazakova, V.M., Bobrikov, Yu.A., Ryabtsev, A.V., Abdurakhmanov, K.P., Zainobiddinov, S., Kamilov, T.S., and Utamuradova, Sh.B., On the State of Impurity Atoms of Manganese in Silicon, *Fiz. Tekh. Poluprovodn.*, 1982, vol. 16, no. 5, p. 939.
4. Bakhadyrkhanov, M.K., Boltaks, B.I., and Kulikov, G.S., Diffusion, Electrotransport, and Solubility of Manganese Impurity in Silicon, *Fiz. Tverd. Tela*, 1972, vol. 14, pp. 1671–1676.
5. Bakhadyrkhanov, M.K., Kamilov, T.S., et al., Photoelectric Properties of p-Type Silicon Doped with Manganese, *Fiz. Tekh. Poluprovodn.*, 1975, vol. 9, no. 1, pp. 76–80.
6. Ayupov, K.S., On IRQ PC in Mn-Doped Silicon, *Elektron. Obrab. Mater.*, 2005, no. 4, pp. 84–88 [*Surf. Eng. Appl. Electrochem.* (Engl. Transl.), no. 4, p. 91].
7. Askarov, Sh.I., Bakhadirkhanov, M.K., Masterov, V.F., and Shtel'mah, V.F., Study of the Interaction between Impurities of Sulfur and Manganese in Silicon by the EPR Method, *Fiz. Tekh. Poluprovodn.,* 1982, vol. 16, no. 7, pp. 1308–1310.
8. Abdurakhmonov, K.P., Lebedev, A.A., Kreissl, J., and Utamuraova, Sh.B., Deep Levels in Silicon Related to Manganese, *Fiz. Tekh. Poluprovodn.*, 1985, vol. 19, no. 2, pp. 213–216.
9. Ayupov, K.S., Bakhadyrkhanov, M.K., Mavlonov, G.Kh, Zkirillaev, N.F., Isamov, S.B., and Koveshnikov, S.V., Study of the Dependence of Negative Magnetoresistance in Silicon Nanoclusters on the Concentration of Manganese Atoms, *6th Int. Conf. Kremnii-2009*, Novosibirsk, 2009.
10. Sheinkman, M.K. and Shik, A.Ya., Long-Term Relaxations and Residual Conductivity in Semiconductors, *Fiz. Tekh. Poluprovodn.*, 1976, vol. 10, no. 2, pp. 209–233.
11. Astrova, E.V., Voronkov, V.B., Lebedev, A.A., et al., Phenomena of Long-Term Relaxation of Residual Conductivity in Photodetectors Based on Si⟨Zn⟩, *Izv. Vyssh. Uchebn. Zaved., Mater. Elektron. Tekh.*, 1999, no. 1, pp. 16–20.

ISSN 1068-3755, Surface Engineering and Applied Electrochemistry, 2010, Vol. 46, No. 3, pp. 281–284. © Allerton Press, Inc., 2010.
Original Russian Text © A.M. Magerramov, M.A. Ramazanov, A.Kh. Mustafaeva, 2010, published in Elektronnaya Obrabotka Materialov, 2010, No. 3, pp. 100–104.

OPERATING EXPERIENCE

# Photoluminescence in Nanocomposites Based on PVDF + ZnS

**A. M. Magerramov, M. A. Ramazanov, and A. Kh. Mustafaeva**

*Baku State University, ul. Khalilova 23, Baku, AZ-1148 Azerbaijan*

*e-mail: nanomaterials@bsu.az, mamed_r50@mail.ru*

Received January 22, 2010

**Abstract**—The photoluminescence properties of nanocomposite materials based on polyvinylidene fluoride (PVDF) with a filler of ZnS are studied in the wavelength region of $\lambda = 300–1000$ nm. PVDF powder with a particle size of 0.5–1.0 μm is used as the matrix. It is shown that an increase in the concentration of the initial solutions leads to an increase in the size of the ZnS nanoparticles in the PVDF; that is, in the process of the cluster formation, the coalescence of the ZnS particles into a nucleation center takes place. It is also found that the composites exhibit a shift of their luminescence bands to shorter wavelengths at a decrease in the concentration of nanoparticles in the matrix and, consequently, in the size. This can be explained by both the reabsorption of the luminescence in the optically dense scattering sample and a change in its spectral composition.

**DOI:** 10.3103/S1068375510030166

The preparation of metal nanoparticles is one of the important problems of modern nanochemistry. The interest in this problem is caused, first of all, by the necessity to obtain small-sized systems for various domains of science and technology. It is well known that the properties of nanodimensional particles differ from the properties of macroparticles. By preparing composite materials that comprise nanoparticles and by controlling the sizes and the form of the nanostructures, it is possible to enrich these composites with entirely new functional characteristics (optical, magnetic, and mechanical) that differ from the properties of conventional materials. Recently, many studies concerned with various aspects of obtaining polymer composite materials with luminescence properties have been carried out. Semiconductor materials in the form of clusters distributed in an organic polymer matrix have been the subjects of intense interest of researchers working in the domain of physics and chemistry of low-dimensional systems for some time [1, 2]. To obtain nanodimensional semiconductor materials, some processing methods are used, such as sol-gel processing [3], the Langmuir–Blodgett method [4], molecular beam epitaxy [5], and the method of multicycle processing [6]. One of the main obstacles to the possible use of structures with semiconductor nanoclusters in optoelectronics is the low efficiency of the luminescence of nanoclusters due to the high density of the surface states. The density of the surface states depends on both the technique of preparation and the subsequent processing of the nanoclusters and the matrix with the introduced nanoparticles. By studying the structure of composites and revealing the relation between the pattern of the supramolecular formation and the properties of the polymers, we can directionally control the structure of the resulting material in order to obtain a desired set of properties. The study of the structure of these materials makes it possible to predict their properties. According to the changes in the properties, we can estimate the structure of the nanocomposites. In this work, we study the photoluminescence of ZnS nanoparticles in a polymer matrix of polyvinylidene fluoride (PVDF).

## EXPERIMENTAL

The photoluminescence properties of a nanocomposite based on PVDF with a filler of ZnS were studied in the wavelength region of $\lambda = 300–1000$ nm. The matrix was a PVDF powder with a particle size of 0.5–1.0 μm.

To enhance the activity with respect to the metal ions, the PVDF powder was exposed to γ-radiation with various doses. After that, the PVDF + ZnS nanocomposite was prepared of this powder. At first, a certain amount of the PVDF powder was mixed with 50 ml of the $ZnSO_4$ solution with a concentration of 0.1 M. The resulting mixture was placed into a mechanical stirrer for 30 min. Subsequently, the powder was filtered and dried for a day. Next, the dry powder was mixed with 50 ml of the $Na_2S$ solution with a concentration of 0.1 M. After that, it was again placed into the mechanical stirrer for 30 min. The filtration and the drying were repeated in the same way.

Other samples of powder were obtained using solutions of $ZnSO_4$ and $Na_2S$ with a concentration of 0.5 and 1 M, respectively. The hot-pressing technique was used at the melting point of PVDF to prepare samples of the PVDF + ZnS nanocomposite from these powders.

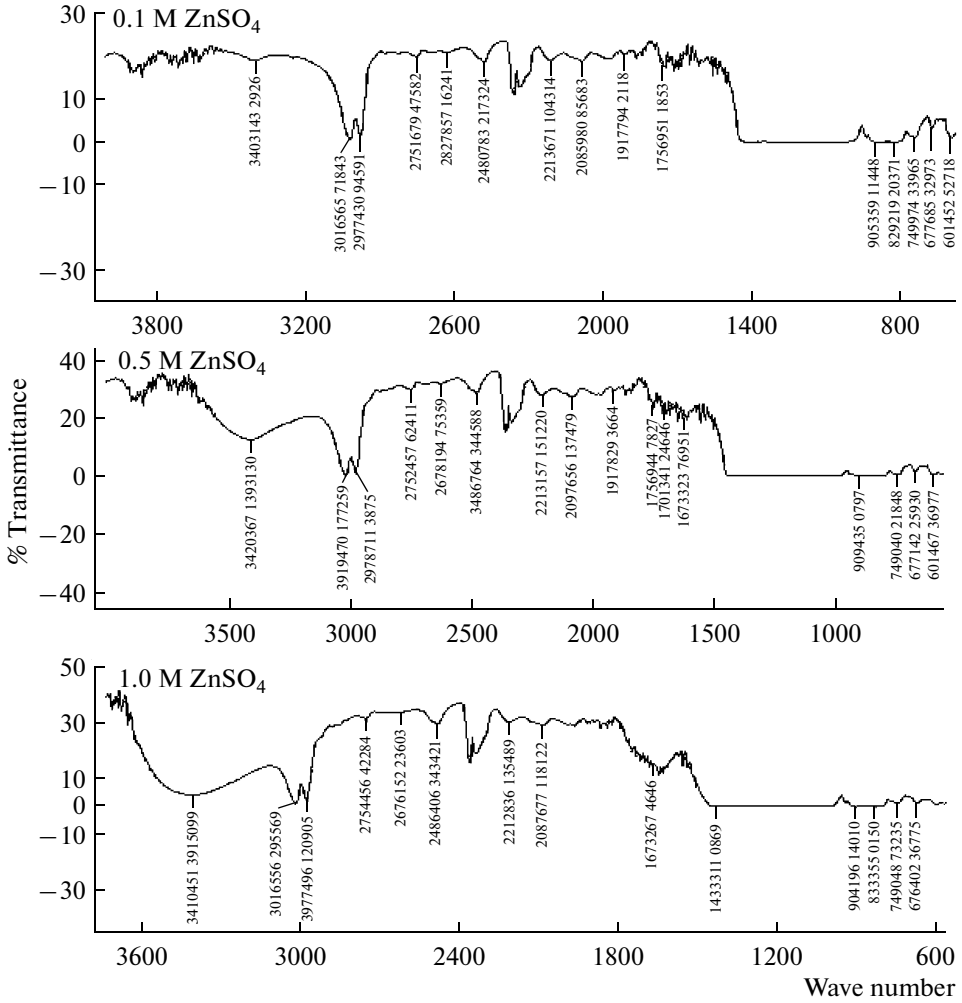


**Fig. 1.** IR spectra of samples of the PVDF + ZnS nanocomposite obtained from the 0.1 M, 0.5 M, and 1 M solutions of $ZnO_4$.

Using atomic force microscopy (AFM), we studied the microreliefs of the PVDF + ZnS nanocomposites and the distribution of ZnS in the polymer matrix of the PVDF.

Infrared spectroscopy was applied to estimate the development of the oxidation–destructive processes in the PVDF polymer.

The absorption spectra were studied using a Perkin-Elmer SF Spectroscopy instrument in the wavelength region of 200–800 nm.

## RESULTS AND DISCUSSION

Figure 1 depicts the IR spectra of the samples of the PVDF + ZnS nanocomposites obtained from the 0.1 M, 0.5 M and 1 M solutions of $ZnSO_4$. As we can see, an increase in the concentration leads to a change in the IR spectrum, particularly, in the wavelength regions of 3410, 3019, 2978, and 905–441 $cm^{-1}$.

The change in the wavelength regions of 3410 and 3019 $cm^{-1}$ is attributed to the formation of hydroxyl groups in the polymer. In addition, as the concentration increases, a strong change in the intensity of the band at 2978 $cm^{-1}$ is observed; it may be indicative of the activation of CH valence vibrations in the PVDF spectrum.

We can also see that there is a change in the wavelength regions of 904, 833, 749, 676, and 601 $cm^{-1}$, which is related to the bands of helical conformation of the chain. The change in the wavelength region of 441 $cm^{-1}$ is due to the zigzag planar chain.

Figure 2 depicts the AFM image of the surface of the PVDF + ZnS nanocomposites that were obtained using PVDF powders in the initial state and the $ZnSO_4$ solution with a concentration of 0.1 M.

The AFM studies of the nanocomposites showed that the sizes of the ZnS nanoparticles in the polymer matrix are 25–40 nm, that the surface roughness varies from 20 to 45 nm, and that the ZnS nanoparticles are distributed in the polymer matrix uniformly. The effect of the concentration of the initial solutions on the size of the nanoparticles in the PVDF was studied. Accord-

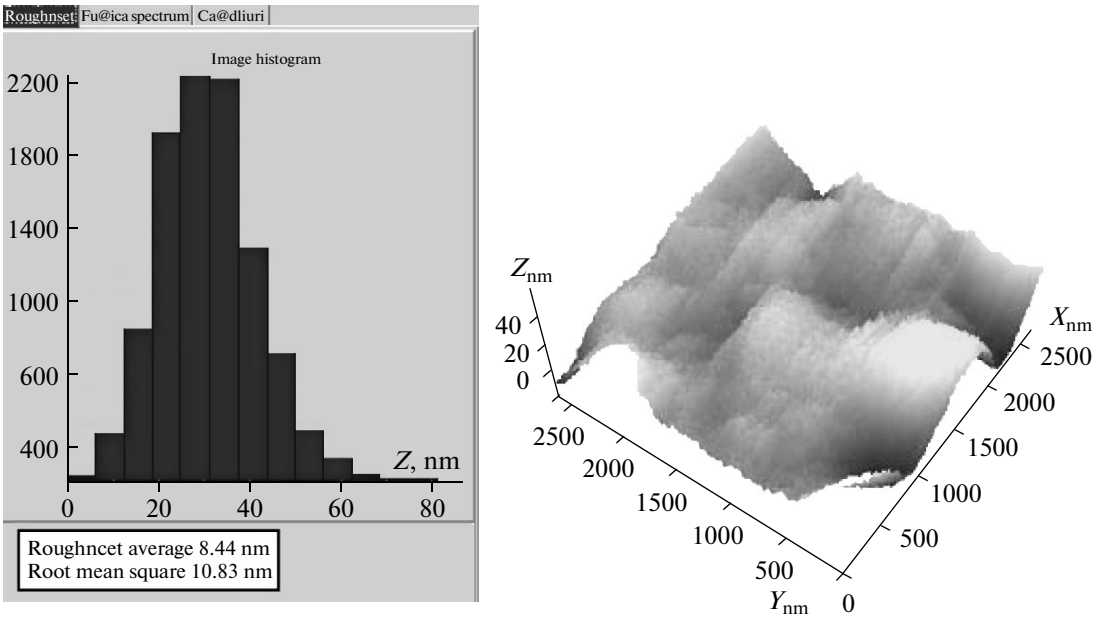


**Fig. 2.** AFM image of the PVDF + ZnS nanocomposite and a histogram of the surface roughness and sizes of the ZnS nanoparticles.

ing to the experimental results, an increase in the concentration of the initial solutions leads to an increase in the size of the ZnS nanoparticles in PVDF; that is, in the process of the cluster formation, the coalescence of the ZnS nanoparticles into a crystallization nucleus takes place.

It was found that an increase in the concentration of the solutions leads to an increase in the sizes of the ZnS nanoparticles in the PVDF; that is, for the 0.1-M solution, the resultant nanoparticles have a size of 25–40 nm and, in the case of the 0.5-M and 1-M solutions, the nanocluster sizes are 50–55 and 70–90 nm, respectively. This is due to the fact that, as the concentration of the solutions increases, the greater part of the $Zn^{2+}$ and $S^{2-}$ ions are consumed for the coagulation of the original particles rather than for the formation of new nucleation centers. The photoluminescence properties of the PVDF + ZnS nanocomposites depending on the concentration of the initial solutions were studied using a Cary Eclipse instrument.

It is seen from Fig. 3 that an increase in the concentration of the initial solutions leads to a change in the luminescence spectra of the PVDF + ZnS nanocomposites. It is shown that, as the concentration increases, the maximum amplitude at a wavelength of 635 nm increases and then decreases, although the change in the maximum for a length of 635 nm is stronger than for a length of 810 nm. It was also found for the nanocomposites containing nanoparticles of ZnS that a decrease in the size and the concentration of the nanoparticles in the matrix leads to a shift of the luminescence bands to shorter wavelengths. This can be explained by both the reabsorption of the lumines-

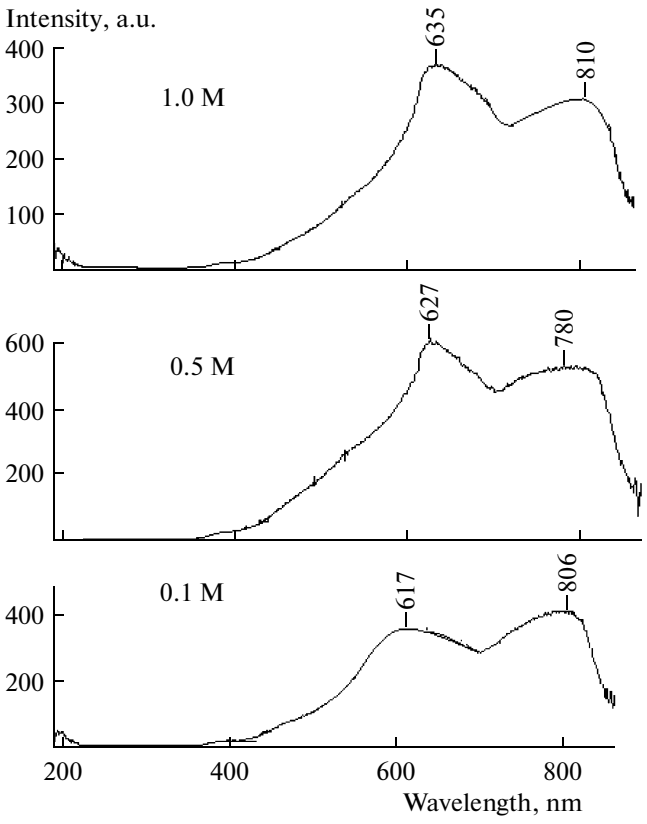


**Fig. 3.** Photoluminescence spectra of the PVDF + ZnS nanocomposites as a function of the concentration of the initial solutions.

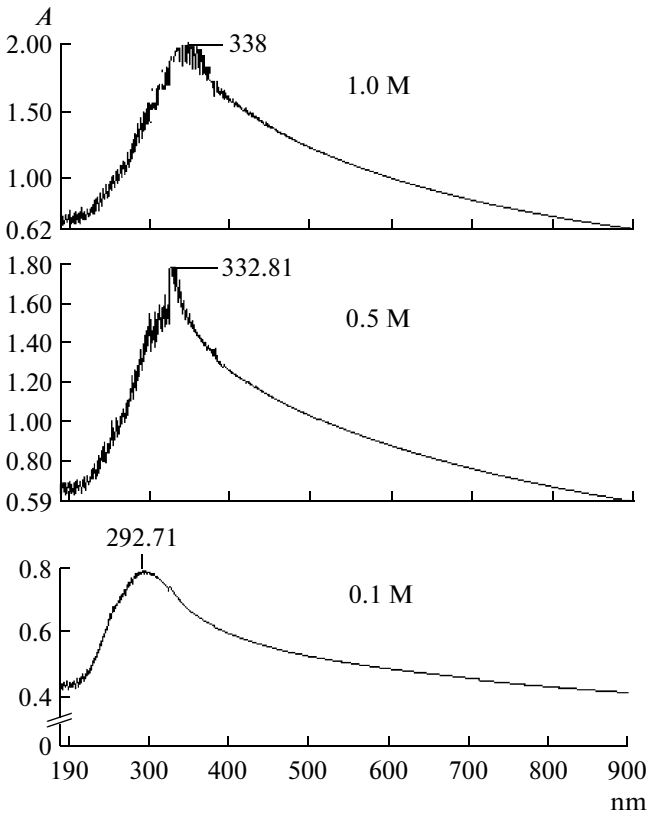


**Fig. 4.** Absorption spectra of the samples of the PVDF + ZnS nanocomposite as a function of the concentration of the initial solutions.

cence in the optically dense scattering samples and a change in its spectral composition. A certain contribution comes from the process of the concentration quenching of the luminescence, which intensifies with the increasing particle size [7].

Figure 4 shows the absorption spectra of samples of the PVDF + ZnS nanocomposites as a function of the concentration of the initial solutions.

We can see from the figure that a shift in the absorption spectrum takes place; that is, in the case of a 0.1-M solution, the maximum amplitude is formed at a wavelength of 292 nm, while, in the case of the 0.5-M and 1-M solutions, it does at wavelengths of 332 and 338 nm. It is also found that the amplitude in the absorption spectrum increases with the increasing concentration.

## CONCLUSIONS

Thus, it is shown that, while the concentration of the initial solutions increases, the sizes of the ZnS nanoparticles in the PVDF grow; that is, in the process of the cluster formation, the coalescence of ZnS nanoparticles into a nucleation center takes place. It is also found that, for the nanocomposites containing nanoparticles of ZnS, a shift of the luminescence bands to shorter wavelengths is observed at a decrease in the concentration of the nanoparticles in the matrix and, consequently, in the size. This can be explained by both the reabsorption of the luminescence in an optically dense scattering sample and a change in its spectral composition.

## REFERENCES

1. Tello, M., Carcia, R., Martin-Gado, J.A., Martines, N.F., and Aballe, L., Bottom-Up Fabrication of Carbon-Rich Silicon Carbide Nanowires by Manipulation of Nanometer-Sized Ethanol Menisci, *Adv. Mater.*, 2005, vol. 17, pp. 1480–1483.
2. Fricke, M., Lorke, A., Kotthaus, J.P., Medeiros-Ribeiro, G., and Petroff, P.M., Shell Structure and Electron-Electron Interaction in Self-Assembled InAs Quantum Dots, *Europhys. Lett.*, 1996, vol. 36, no. 3, p. 197.
3. Magerramov, A.M., Ramazanov, M.A., and Gadjieva, F.V., Role of Phase Interactions in Formation of Photoluminescent and Dielectric Properties of Polymeric Nanocomposites PP + CdS, *J. Optoelectron. Adv. Mater. – Rapid Commun.*, 2009, vol. 3, no. 12, pp. 1348–1353.
4. Bagaev, E.A., Zhuravlev, K.S., Sveshnikova, L.P., Badmaeva, I.A., and Repinskii, S.M., Photoluminescence from Cadmium Sulfide Nanoclusters Formed in the Matrix of a Langmuir–Blodgett Film, *Fiz. Tekh. Poluprovodn.*, 2003, vol. 37, no. 11, p. 1358 [*Semiconductors* (Engl. Transl.), vol. 37, no. 11, p. 1321].
5. Magerramov, A.M., Ramazanov, M.A., and Gadjieva, F.V., Properties and Structure Formation of Cadmium Sulfide Nanocomposites with Polypropylene, *J. Optoelectron. Adv. Mater. – Rapid Commun.*, 2008, vol. 2, no. 11, pp. 743–746.
6. Ramazanov, M.A., Photoluminescence in Nanocomposites Based on Polyvinylidene Fluoride and a Filler of CdS, *Prilk. Fiz.*, 2007, no. 6, pp. 8–11.
7. Sokolov, V.A. and Gorban', A.N., *Lyuminestsentsiya i adsorbtsiya* (Luminescence and Adsorption), Vol'kenshtein, F.F., Ed., Moscow: Nauka, 1988, pp. 17–23.

ISSN 1068-3755, Surface Engineering and Applied Electrochemistry, 2010, Vol. 46, No. 3, pp. 285–290. © Allerton Press, Inc., 2010.
Original Russian Text © B.I. Stavitskii, 2010, published in Elektronnaya Obrabotka Materialov, 2010, No. 3, pp. 105–109.

INFORMATION

# Glimpses of the History of Electrospark Machining of Materials[1] (Dedicated to the Centenary of B.R. Lazarenko)

**B. I. Stavitskii**

*Candidate of Engineering, Senior Researcher, Lenin Prize Laureate,*
*Chief Designer of Electrospark Equipment for the Electronics Industry.*
*Fryazino, Russia*

**DOI:** 10.3103/S1068375510030178

In connection with the forthcoming centenary celebration of B. R. Lazarenko, we shall continue the trip down memory lane concerning the state-of-the-art of the electrospark machining of metals abroad in the first decade after the discovery made by him scientist. Thus, analyzing the results of the First International Symposium on the Electrospark Machining of Metals, which was held on September 12–20, 1960, in Prague and estimating the state-of-the-art of engineering developments, B.R. Lazarenko pointed out that the Soviet Union was certainly ahead in the domain of original designs for electrospark installations, the parameters of which were superior to the foreign level.

The Symposium was initiated by the Scientific and Technical Society of the Czechoslovak Socialist Republic. Leading specialists in the domain of the electrospark machining of metals from 11 countries of the world (Austria, England, Hungary, the German Democratic Republic, the People's Republic of China, Poland, the Soviet Union, France, the Federal Republic of Germany, the Czechoslovak Republic, and Switzerland) came together for the first time; thereby, they not only witnessed the general recognition of the electrospark machining of metals but also summarized the achievements and outlined the ways of further development of this highly innovative process. The Symposium began with an opening speech of the Chairman of the Slovak Branch of the Czech Technical Society of the Czechoslovak Republic J. Stanek and with the election of B.R. Lazarenko the president of the symposium.

Figure 47 depicts B.R. Lazarenko at the symposium on the electrospark machining of metals. The person to his right in the photograph is V.Yu. Veroman—one of the experts in the domain of ultrasonic, electrical, and electrochemical methods of treatment of metals and nonmetallic materials in Leningrad, who was engaged in the development and study of the processes of high-frequency electrospark machining of metals.

This photograph was given to Boris Romanovich by Jindrich Stanek in Chisinau when he was visiting the Institute of Applied Physics of the Moldavian Academy of Sciences on August 5, 1967; the photograph has the following presentation inscription:

"To my dear teacher Academician Lazarenko
as a memento and as an expression
of my gratitude for those times when
I was learning to perceive the wonderful
spark phenomenon.

Jindrich Stanek
Chisinau, August 5, 1967"

Figure 48 shows B.R. Lazarenko and Jindrich Stanek at the First International symposium on the electrospark machining of metals in Prague in 1960.

The director of the Research Institute for Mechanization and Automation (VUMA) J. Stanek demonstrated a unique BQD-4 electrospark installation to the participants of the Symposium; the installation was designed for the simultaneous machining of 30 grooves of a forming roll with a diameter of 350 mm and a length up to 1700 mm (Fig. 49a). The capacity of the installation is 5 kVA. It works automatically, and a forming roll is completely finished after 8 h. The installation has a three-loop circuit, and conventional industrial water is used as the interelectrode medium. A number of measures are designed into the installation that make it electrically safe in service.

The representative of the Hermann Schlimme Plant, the engineer G. Rossa (Berlin, GDR), reported to the participants of the Symposium on a similar installation for electrospark machining of grooves of a forming roll (Fig. 49b). The Engineering Director of the Industrial Electronics Society (AGIE) V. Ullman brought to the attention of the participants of the symposium a new model of the SIP-AGIE electrospark installation for high-precision works (Fig. 49c).

The installation is based on the successful combination of the achievements in electronics and the production technology of optical measuring devices. Based on the tables of the SIP optical coordinate measuring machines, which were well-proven by long-

[1] This is a continuation, see the beginning in *Surf. Eng. Appl. Electrochem.*, nos. 1–2, 2010.

B.P. and N.I. Lazarenko at the company AGIE.

**Fig. 47.** B.R. Lazarenko at the International Symposium on the Electrospark Machining of Metals.

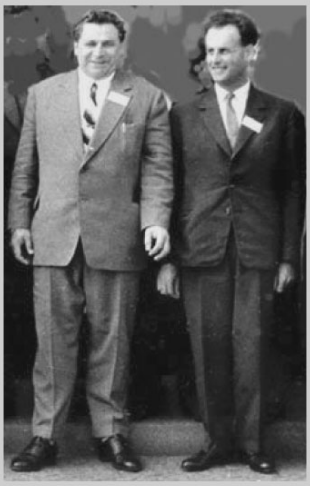

Prague, September 1960

**Fig. 48.** B.R. Lazarenko and Jindrich Stanek at the First International Symposium.

term practice, the experts in electronics designed a SIP-AGIE automatic installation with the following engineering data:

| | |
|---|---|
| Maximum area of the workpiece, mm | 400 × 250 |
| Guaranteed running accuracy, μm | 2 |
| Automatically controlled travel of the spindle at a distance, mm | 150 |
| Installation capacity, kVA | 1.7 |
| Maximum yield, $mm^3$/min | 300 |
| Surface finish by a solid alloy | class 10 |

The same company demonstrated two more electrospark installations: VL-6 and BKU-12. The first of them, i.e., VL-6, is universal and is intended for some electrospark works. The BKU-12 installation is designed for machining large workpieces, mainly for the production of forging dies.

The Swiss company Charmilles showed an Eleroda D-15 electrospark installation for heavy works. Its capacity is 30 kVA, the maximum area of the workpiece is up to 1080 × 470 mm, and the maximum yield is up to 4000 $mm^3$/min.

**The First International Symposium on the Electrospark Machining of Metals was organized by the Scientific and Technical Society of the Czechoslovak Republic and proceeded from September 12 to September 20, 1960.**

B.R. Lazarenko wrote in his publication concerned with this symposium:[2]

"*In the history of the electrospark method of machining of metals, there are several characteristic periods: the search for the discoverers of the electrospark method, the involvement of new researchers into this domain of science; the penetration of this method into various branches of industry; and, finally, the general recognition of this process as a new field of electrophysics of great theoretical and practical significance. In this regard, 1960 was a particularly remarkable year, when the lead-*

[2] Lazarenko, B.R., First International Symposium on the Electrospark Machining of Metals, in *Tsentral'naya nauchno-issledovatel'skaya laboratoriya elektricheskoi obrabotki materialov AN SSSR. Problemy elektricheskoi obrabotki materialov* (Central Scientific Research Laboratory for Electrospark Machining of Metals Acad. Sci. USSR. Problems of Electrospark Machining of Materials), Moscow: Akad. Nauk SSSR, 1962, pp. 169–180.

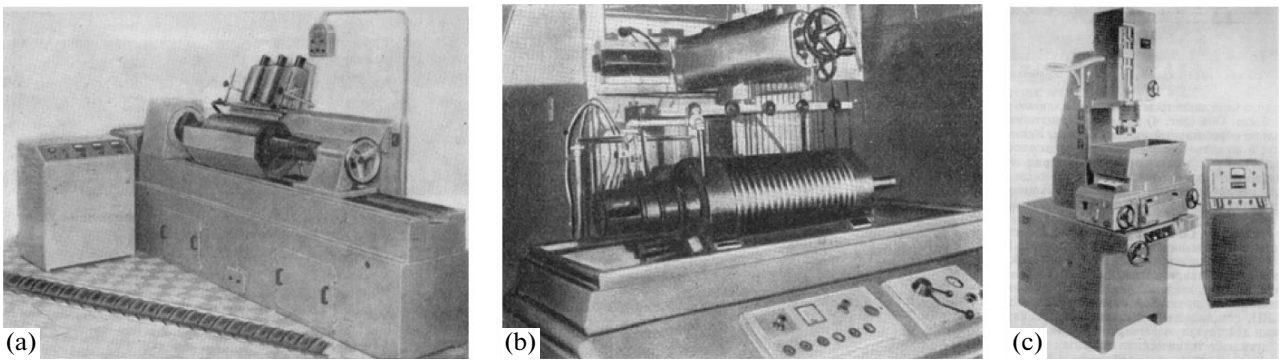

**Fig. 49.** (a) The BQD-4 (Czechoslovak Republic) installation for electrospark machining of grooves of a forming roll, (b) the Hermann Schlimme (GDR) installation for electrospark machining of grooves of a forming roll, and (c) the SIP-AGIE (Switzerland) electrospark installation for high-precision works.

**Fig. 50.** Participants in the First International Symposium on the Electrospark Machining of Metals in Prague (1960).

*ing specialists in the domain of electrospark machining of metals from 11 countries of the world (Austria, England, Hungary, the GDR, the People's Republic of China, Poland, the Soviet Union, France, the FRG, the Czechoslovak Republic, and Switzerland) came together for the first time; thereby, they not only witnessed the general recognition of the electrospark machining of metals but also summarized the achievements and outlined ways of further development of this highly innovative process.*"

Figure 50 depicts a group photograph of the participants in the symposium.

Among them, in the first row (from the left to right) are Hu Dzhuan-Jin (People's Republic of China), Kh.V. Obrig (FRG), K. Albinski (Poland), V. Ullman (Switzerland), B.R. Lazarenko (Soviet Union), J. Stanek (Czechoslovak Republic), D. Fefer (England), and K. Smith (England). G. Rossa (GDR) and (to his left) A. Roth (Hungary) stand behind K. Albinski.

For the first three days, the symposium was held in Prague and was concerned with presentations and discussions. The symposium began with the opening speech of the Chairman of the Slovak Branch of the Czech Technical Society of the Czechoslovak Republic J. Stanek and with the election of B.R. Lazarenko the president of the symposium.

The following reports were represented at the symposium:

(1) "The State-of-the-Art of Electrospark Machining of Metals and the Main Tasks of This Science" (Soviet Union, B.R. Lazarenko).

**Fig. 51.** (a) After the ceremony of awarding commemorative medals of Prague University by its dean L. Ganka (in the center) to F. Griffiths (to the left) and Prof. B.R. Lazarenko (to the right) for their transcendental merit in the field of engineering. (b) The Fair in Brno (from the left to right): licensed engineer Roth (Budapest), licensed engineer Albinski (Krakow), W. Berger (Switzerland), and Prof. Lazarenko.

(2) "The Physics of Spark High-Current Discharge and Electroerosion" (Czechoslovak Republic, V. Ermokh).

(3) "The Use of Spark Erosion in Research Laboratories" (Czechoslovak Republic, I. Khudoba).

(4) "A New Type of Electric Current Pulse Generator Applied for Electrospark Machining of Metals" (France, M. Bruma).

(5) "Some Patterns of Electrospark Machining of Metals" (Czechoslovak Republic, I. Preis and E. Zelenai).

(6) "Electrospark Machining of Materials" (FRG, Kh.V. Obrig).

(7) "Control of Electrospark Processes" (Czechoslovak Republic, V. Senetskii).

(8) "On the Problems of the Technique of Electrospark Machining of Metals" (Czechoslovak Republic, J. Stanek).

(9) "Some Problems of the Precision of Electrospark Machining of Metals" (Hungary, A. Roth).

(10) "The Production of a Processing Electrode as a Crucial Factor of Electrospark Tools and Dies" (GDR, W. Gruner).

(11) "The Electrospark Machining of Metals and its Economic Value in Various Branches of Industry" (GDR, G. Rossa).

(12) "The Technology of Electrospark Making of Small-Size Holes" (Czechoslovak Republic, I. Janowitz).

(13) "Some Technological Problems of Electrospark Machining of Dies and Molds" (Poland, K. Albinski).

(14) "The Technique of Production of Forging Dies by the Electrospark Method" (Czechoslovak Republic, Zhuhai).

(15) "Cost-Effective Production of Dies and Molds" (Switzerland, V. Ullman).

Each of the reports was discussed. At the end of this part of the symposium, Dean of the Czech Technical University Prof. Doctor Eng. L. Ganka awarded commemorative medals of the University to the representative of the Soviet Union, B.R. Lazarenko, and to the representative of the British aviation company F. Griffiths for their achievements in the field of the development of engineering sciences.

The second part of the symposium was concerned with the studying of the work of the most advanced designs of electrospark installations. For this purpose, on September 16, all the participants left for Shumperk to visit the integrated plant for hard alloys that comprises a workshop fully equipped with electrospark installations designed in the VUMA and after that to visit the Second International Fair in Brno, where some countries demonstrated their achievements in the domain of electrospark machining, among them there were electrospark installations and processes developed in the Czechoslovak Republic, Poland, the People's Republic of China, England, and Switzerland.

**The most part of the works that were reported at the symposium were concerned with the basic physics of the process of electrospark machining of metals,** yet they were not original in terms of explaining the process and the known tenets of the theory (including those that were established in the works of the inventors of the method, i.e., B.R. and N.I. Lazarenko).

The study carried out at the Institute of Technical Physics of the Academy of Sciences of the Czechoslovak Republic (V. Ermokh) was the most interesting in this regard. V. Ermokh correctly stated that the period of spontaneous development and implementation (engineering of new designs of installations and technology) would be based on the data obtained by phys-

icists. He also pointed out some shortcomings in the physical studies published by many authors and drew the attention of the participants of the symposium to the need for more rigorous and universal methods of physical experiments.

*The work of the symposium showed that the greatest advances in the study of the physics of the process of electrospark machining of metals belong to the physicists of the Soviet Union.*

The representative of the French National Center for Scientific Research—Prof. M.S. Bruma—aptly generalized the main physical and technical requirements that must be imposed on generators feeding the spark gap. For this purpose, he considered two questions:

(i) What is the most reasonable value of the voltage to be applied for electrospark machining?

(ii) How does the amount of ejected material depend on the duration and power of a single pulse as well as on the pulse repetition frequency?

It is obvious that the higher the voltage is, the lower the machining precision is. Other things being equal, an increase in the voltage leads to a deterioration of the surface quality and to a significant increase in the wear ratio of the processing electrode.

An increase in the power and the repetition rate of the discharges increases the erosion of the anode, and an increase in the pulse duration decreases it. Therefore, to increase the efficiency of electrospark machining, it is necessary to simultaneously control the repetition frequency and the duration of the pulses, the voltage, and the instantaneous current; however, it should be done so that the wear of the processing electrode does not increase with the deterioration of the surface finish commensurately.

M.S. Bruma solved this problem by designing an electric bridge circuit (Fig. 52a), one of its diagonals forms a processing electrode–workpiece circuit, and the other is connected with its terminal points to the generator, which generates a voltage significantly lower than 100 V at a few amperes and a variable frequency of 3–12 kHz. The change of the alternating low-voltage current into high-power polar pulses of high frequency is performed using silicon diodes.

The operation of this generator is based on the dynamic equilibrium of the bridge: in the course of the discharges, the total reactivity is zero and the power source supplies the maximum current; upon contacting of the electrodes (Fig. 52b), the bridge's balance is disturbed, which leads to the appearance of reactance that automatically limits the strength of the current supplied by the power source. The design of the whole circuit in the form of concentric cylinders is noteworthy (Fig. 52c).

The Engineering Director of Sparkatron (England)—the engineer D. Fefer—reported very good results for unipolar low-voltage pulses. The company constructed a 400-Hz rotating generator and developed a silicon-rectifier circuit that feeds electrodes with electric pulses with a duration of $9 \times 10^{-4}$ s at a voltage of 22 V and an average (controlled) current up to 150 A.

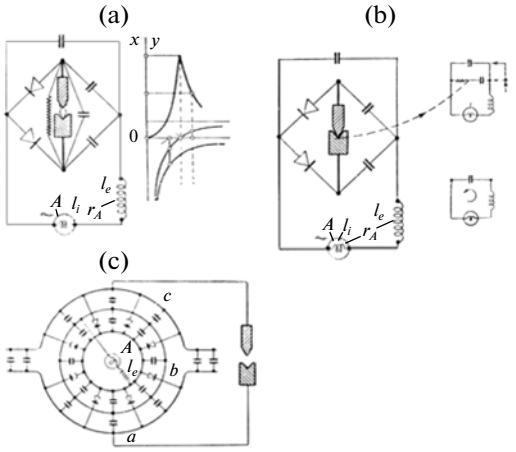


**Fig. 52.** Electric-pulse generator developed in the National Center for Scientific Research (France): (a) the system's condition in normal service, (b) the same in the event of a fault, and (c) the layout of the circuit components.

The circuit operating in a Uzimyu electrospark installation of the French company Qualitex deserves attention. This multitube pulse-transformer electronic circuit provides a unipolar pulse repetition frequency of more than 300000 per second.

**In the opinion of B.R. Lazarenko, all the participants in the symposium mentioned that the electrospark machining of metals has become a constituent of mechanical-engineering technology, the manufacture of some products was unthinkable without it (this was said in 1960, i.e., 50 years ago!).**

Moreover, it has became clear that the possibilities of the electrospark method of metal machining are so multifold that a further and extremely sharp reduction in the volume of metal cutting will take place in the nearest future. In this aspect, the report made by the Director of VUMA—J. Stanek—was very illustrative. The analysis given by him showed that 13 industrially advanced countries produce about 80 types of electrospark installations with a capacity of 0.2–40 VA. In addition, special-purpose electrospark installations have a capacity of a few hundred kVA. The average capacity of the produced installations is 5 kVA.

Using the example of the industry of the Czechoslovak Republic, J. Stanek showed the dynamics of the development and application of the electrospark machining of metals. Until quite recently, no electrospark installations were in the Czechoslovak Republic; however, by 1960, hundreds of units worked in its industry; moreover, the Czechoslovak Republic began to export its products to a number of countries. In the

past, universal electrospark installations intended mainly for works in tool workshops were developed and manufactured, whereas, at present, the trend is for the preparation of high-performance single-purpose electrospark installations. One of them was discussed above (see Fig. 49a).

All the participants in the symposium mentioned the extremely high technical-and-economic efficiency of the electrospark machining of metals, owning to which the production of this equipment is increasing sharply in all countries.

In conclusion, B.R. Lazarenko remarked that results of the work of the symposium made it possible to assess the state-of-the-art of this process of machining, to determine the most probable trends of its further development, and to come into personal contact with many specialists in the domain of electrospark machining of metals.

When finishing his paper on the First International Symposium on the Electrospark Machining of Metals, B.R. Lazarenko wrote the following (see the footnote above):

"*When summarizing the state-of-the-art of engineering developments, it should be noted that our country undoubtedly heads the domain of original designs of electrospark installations, the parameters of which are superior to the foreign ones. For example, we can mention the ELEKTROM-15 electrospark installation designed in the TsNIL-ELEKTROM of the Academy of Sciences of the Soviet Union and a whole host of electrospark installations designed in the State Union Research Institute of the State Committee of the Council of Ministers of the Soviet Union on Electronic Engineering.*"

To be continued.